Novel Machine Learning-Driven Platforms for In-Situ Prediction of Vertical and Top Surface Roughness in Laser Powder-Bed Fusion

by

Sahar Toorandaz Kenari

A thesis

presented to the University of Waterloo

in fulfillment of the

thesis requirement for the degree of

Doctor of Philosophy

in

Mechanical and Mechatronics Engineering

Waterloo, Ontario, Canada, 2025

© Sahar Toorandaz Kenari 2025

Examining Committee Membership

The following served on the Examining Committee for this thesis. The decision of the Examining Committee is by majority vote.

External Examiner:	Swee Leong Sing, Ph.D. Assistant Professor Department of Mechanical Engineering National University of Singapore
Supervisor:	Ehsan Toyserkani, Ph.D. Professor Department of Mechanical and Mechatronics Engineering University of Waterloo
Internal Member:	William Melek, Ph.D. Professor Department of Mechanical and Mechatronics Engineering University of Waterloo
Internal Member:	Mustafa Yavuz, Ph.D. Professor Department of Mechanical and Mechatronics Engineering University of Waterloo
Internal-External Member:	Adil Al-Mayah, Ph.D. Professor Department of Civil and Environmental Engineering University of Waterloo

Author's Declaration

This thesis consists of material all of which I authored or co-authored: see Statement of Contribution included in the thesis. This is a true copy of the thesis, including any required final revisions, as accepted by my examiners.

I understand that my thesis may be made electronically available to the public.

Statement of Contribution

The following chapters, 1, 2, and 5, were authored exclusively by Sahar Toorandaz Kenari under the supervision of Prof. Ehsan Toyserkani and were not intended for publication. Portions of this thesis include two manuscripts prepared for publication:

Chapter 3:

The conceptualization of the study was carried out by Sahar Toorandaz Kenari and Prof. Ehsan Toyserkani, with methodology developed by Sahar Toorandaz Kenari and Prof. Ehsan Toyserkani. Software development was handled by Sahar Toorandaz Kenari and Dr. Farima Liravi, while validation was performed by Sahar Toorandaz Kenari and Dr. Katayoon Taherkhani. Formal analysis and investigation were conducted by Sahar Toorandaz Kenari. Data curation was managed by Sahar Toorandaz Kenari, Dr. Katayoon Taherkhani, and Dr. Farima Liravi. The original draft was written by Sahar Toorandaz Kenari, with review and editing contributions from Dr. Katayoon Taherkhani, Dr. Farima Liravi, and Prof. Ehsan Toyserkani. Visualization was done by Sahar Toorandaz Kenari, with supervision and project administration by Prof. Ehsan Toyserkani. Resource and funding were secured by Prof. Ehsan Toyserkani. All authors reviewed and approved the final manuscript.

Citation for Chapter 3:

Sahar Toorandaz, Katayoon Taherkhani, Farima Liravi, Ehsan Toyserkani. A novel machine learning-based approach for in-situ surface roughness prediction in laser powder-bed fusion. Additive Manufacturing, 2024.

Chapter 4:

The study was conceptualized by Sahar Toorandaz Kenari and Prof. Ehsan Toyserkani, with the methodology also developed by the same team. Software development was carried out by Sahar Toorandaz Kenari, Dr. Farima Liravi and Dr. Osazee Ero, while Sahar Toorandaz Kenari handled the validation. Formal analysis and investigation were performed by Sahar Toorandaz Kenari. Data curation was jointly managed by Sahar Toorandaz Kenari and Dr. Farima Liravi. Sahar Toorandaz

Kenari authored the original draft, with Dr. Farima Liravi and Prof. Ehsan Toyserkani contributing to its review and editing. Visualization was prepared by Sahar Toorandaz Kenari, while Prof. Ehsan Toyserkani oversaw supervision and project administration. Resources and funding were provided by Prof. Ehsan Toyserkani. All authors reviewed and approved the final version of the manuscript.

Citation for Chapter 4:

Submitted - Sahar Toorandaz, Farima Liravi, Osazee Ero, Ehsan Toyserkani. *A Pioneer Machine Learning-Driven Platform for In-Situ Vertical Side Surface Roughness Prediction in Laser Powder Bed Fusion. Journal of Manufacturing Systems, 2025*.

Abstract

Controlling and optimizing surface roughness remains a significant challenge in Laser Powder Bed Fusion (LPBF), as roughness profoundly influences fatigue life, mechanical performance, and post-processing (e.g., machining) costs. While in-situ monitoring has emerged as a key approach for real-time defect detection, predicting surface roughness, particularly for both top and vertical surfaces of parts being printed, remains underexplored. Existing studies predominantly rely on camera-based methods, which usually suffer from the limitations such as lack of viewability of vertical surfaces covered by loose powder particles in LPBF, sensitivity to ambient light, resolution constraints, and the need for additional optical equipment. This research pioneers a novel photodiode-based in-situ monitoring framework integrated with machine learning (ML) algorithms to predict surface roughness in real-time for both top and vertical surfaces of LPBF-printed parts.

For top surface roughness prediction, the methodology involves capturing light intensity signals from the melt pool using an on-axial photodiode, incorporating additional process parameters, and training multiple ML models to predict surface roughness at a fine spatial resolution (690 μm × 510 μm), including edges and corners. The framework is rigorously evaluated across a wide range of roughness values, demonstrating its robustness in adapting to process parameter variations.

For vertical surface roughness prediction, this study introduces the first-ever in-situ framework using photodiode signals to overcome challenges posed by loose powder coverage, which obstructs conventional sensing techniques. Key time-domain and frequency-domain features are extracted from photodiode signals captured near vertical surfaces and combined with essential process parameters to train ML models. Among the five ML models evaluated, Random Forest (RF) and eXtreme Gradient Boosting (XGB) demonstrated the highest accuracy and lowest error rates. Incorporating in-situ data significantly improved RF's performance, increasing R^2 from 0.35 (using process parameters alone) to 0.78, confirming the effectiveness of this approach.

This research introduces an innovative pathway for real-time surface roughness prediction in LPBF, enabling enhanced quality assurance, process optimization, and defect mitigation. The integration of photodiode signals with advanced ML algorithms enables precise, on-the-fly assessment of both top and vertical surfaces, enhancing the ability to detect and address irregularities as they occur. By addressing the limitations of traditional camera-based methods, this photodiode-ML framework provides a fast, adaptive, and scalable solution for real-time surface

monitoring, paving the way for more advanced quality control strategies, and promising greater reliability and consistency in the production of high-performance components.

Acknowledgements

The completion of this research would not have been possible without the invaluable support and contributions of many individuals, to whom I am deeply grateful.

I would like to express my sincere gratitude to my esteemed supervisor, Professor Ehsan Toyserkani, for his unwavering support, exceptional guidance, and thoughtful advice throughout this journey. His constant encouragement and mentorship have been pivotal in shaping my academic and scientific growth at the University of Waterloo.

I would like to extend my heartfelt appreciation to my thesis examining committee members: Dr. Swee Leong Sing from National University of Singapore, along with Prof. William Melek, Prof. Mustafa Yavuz, and Prof. Adil Al-Mayah from the University of Waterloo. I am grateful for their time, effort, and thoughtful review of my thesis, as well as their valuable feedback and insightful suggestions, which have greatly contributed to the improvement of this work.

I would also like to express my sincere gratitude for the financial support provided by the Natural Sciences and Engineering Research Council of Canada (NSERC) and the Department of Mechanical and Mechatronics Engineering at the University of Waterloo. Their contributions have been instrumental in making this research possible.

I would like to extend my heartfelt thanks to my current and former colleagues at the Multi-scale Additive Manufacturing (MSAM) Laboratory at the University of Waterloo, including Dr. Farima Liravi, Dr. Katayoon Taherkhani, Dr. Nadia Azizi, Dr. Shima Akbarian and Dr. Osazee Ero, for their invaluable assistance and advice.

I am also deeply grateful to the technical staff at the University of Waterloo, including Francis Dibia, Jerry Ratthapakdee, and Grace Kurosad, for their exceptional support and help with the experimental tests.

Lastly, I offer my heartfelt gratitude to my parents and siblings for their unwavering love, constant support, and endless encouragement throughout this journey.

Dedication

To my beloved Family

Contents

Examining Committee Membership ii

Author's Declaration iii

Abstract vi

Acknowledgements viii

Dedication ix

List of Figures xiii

List of Tables xviii

Chapter 1. Introduction 1

1.1. Motivation and Challenges 1

1.2. Objectives 2

1.3. Thesis Outline 6

Chapter 2. Literature Review and Background 7

2.1. Abstract 7

2.2. Additive Manufacturing (AM) and Laser Powder Bed Fusion (LPBF) 7

2.3. Defects and Process Challenges in LPBF 7

2.4. Quality Assurance in LPBF 9

2.4.1. In-situ Sensors 10

2.4.2. Overview of Machine Learning 11

2.5. Surface Roughness Prediction in LPBF 12

2.5.1. Ex-Situ Surface Roughness Prediction 13

2.5.2. In-Situ Surface Roughness Prediction 18

2.6. Summary 22

Chapter 3. A Novel Machine Learning Based Approach for In-situ Surface Roughness Prediction in Laser Powder-Bed Fusion....24
3.1. Abstract....24
3.2. Methodology and Data Preprocessing....24
3.2.1. Design of Experiment....24
3.2.2. Data Collection....26
3.2.3. Correlation between the Collected Data....28
3.2.4. Feature Engineering....30
3.2.5. Dataset Splitting....36
3.2.6. Strategies for Handling Imbalanced Data....37
3.2.7. Implementation of Machine Learning Algorithms....37
3.3. Results and discussion....40
3.3.1. Tuning Models Hyperparameters....40
3.3.2. SOM Cluster Size Evaluation....42
3.3.3. Feature Combination Analysis....45
3.3.4. Models Performance Assessment....47
3.3.5. Training Set Size Exploration....52
3.3.6. Random Forest Feature Importance....53
3.4. Summery....55
Chapter 4. A Pioneer Machine Learning-Driven Platform for In-Situ Vertical Side Surface Roughness Prediction in Laser Powder Bed Fusion....57
4.1. Abstract....57
4.2. Methods and Data Preparation....58
4.2.1. Experimental Design Strategy....58
4.2.2. Data Acquisition and Measurements....60
4.2.3. Feature Engineering Techniques....65

4.2.4. Development of the Machine Learning Model 66
4.3. Results and Discussion 74
4.3.1. Distribution of Surface Roughness (*Sa*) Measurement 74
4.3.2. Cross-Validation Analysis 75
4.3.3. Models' Performance Evaluation on Unseen Test Data 79
4.3.4. Feature Importance Assessment 85
4.4. Summary 87
Chapter 5. Conclusion and Future Work 89
5.1. Conclusions of In-Situ Top Surface Roughness Prediction 89
5.2. Conclusions of In-Situ Vertical Side Surface Roughness Prediction 90
5.3. Future work 91
Letter of Copyright Permission 93
References 101

List of Figures

Figure 1-1. Graphical illustration of the first objective of the present study. The photodiode signal at each point is captured and integrated with additional features. This combined data serves as input for a machine learning model, which predicts the Sa value categorized into four classes. This methodology enables Sa class predictions for every small area (690 µm × 510 µm) of the top surface, including edges and corners across each layer. In this illustration, while the layer is incomplete, the model predicts the Sa class for the printed area, with the remaining regions awaiting data to complete the prediction map for that layer [5]. 4
Figure 1-2. Graphical illustration of the second objective of the present study. By selecting any vertical side and any specific region of interest along that side, light intensity signals are collected from areas near the edges of the chosen region. Through signal processing, key features are extracted and integrated with essential process parameters to predict the surface roughness of the vertical side within the specified region of interest.....5
Figure 2-1. Schematic of LPBF equipped with on-axis and off-axis photodiodes [33].....11
Figure 2-2. Results of ANN modeling for each cross-validation. Figure reproduced from [46]…14
Figure 2-3. Comparison between predicted and measured surface roughness Ra. Figure reproduced from [49]. 15
Figure 2-4. Roughness distribution on different sides of one produced cube. Figure reproduced from [54]. 17
Figure 2-5. Impact of scan strategy on surface roughness: a) Simple bidirectional scan strategy with no rotation between layers, used for Cube 1. b) Stripe scan strategy with 67° rotation between layers, used for Cube 2. c) 2D height map for layer 22 of Cube 1. d) 2D height map for layer 22 of Cube 2. Figure reproduced from [56].....19
Figure 2-6. Height distribution of Layers 1 through 4, before and after correction using Inline Coherent Imaging (ICI), Figure reproduced from [57]. 20
Figure 3-1. Process parameters, sorted by descending VED values, aligned with part locations (replicates A and B).....25
Figure 3-2. Visual representation of data collection process. Step one: Capturing light intensity data during printing with an in-situ monitoring photodiode sensor. Step two: Measuring the entire top surface height of parts using a laser scanning confocal microscope (LSCM). 26

Figure 3-3. Light intensity distribution of the last three layers and height distribution of the top layer for some parts. 29
Figure 3-4. An example of the segmentation of light intensity and height distribution of Part 10/A (dimension of each cell is 690 µm × 510 µm). Each cell has a distinct distribution of light intensity or height.....31
Figure 3-5. Feature extraction from each cell. I) Clustered Light Intensity: Clustering light intensity data in a single cell using SOM and calculating the centroid of each cluster. These values are different for each cell, even within one part. II) Process Parameters: Considering some specific process parameters. These values are the same for all cells within one part but vary from part to part. III) Spatter Region Index: Factoring in part location on the build plate and potential spatter presence by utilizing i and j indices. These values are the same for all cells within one part but vary from part to part. IV) Edge Proximity Index (epi): Considering the distance between a cell and the edges of a part through quadrant partitioning at the cell of interest and counting the density of cells in each quadrant. These values are different for each cell, even within one part. 34
Figure 3-6. a) Quantifying surface roughness (Sa) by analyzing the height distribution of each cell and classifying the results into distinct classes. b) Boxplot diagram displaying Sa values for all cells, highlighting statistical parameters and aligning with the selected range of Sa classes. 36
Figure 3-7. An illustration depicting the application of a ML algorithm, showing input features and output, along with the process of combining the first group of features for the last three layers. Note that the other feature groups remain constant across all layers.....39
Figure 3-8: Results of 10-fold cross-validation. a) Average F1-score with standard deviation error bars across 10 iterations. b) F1-score comparison per class for each model using 6 SOM clusters. 44
Figure 3-9: Result of unseen test dataset for different number of SOM cluster using RF model. a) F1-score comparison per class and macro F1-score. b) Recall comparison per class and macro recall. 45
Figure 3-10: Comparison of the models' performance using different combinations of input features on unseen test set. a) All four groups employed. b) Exclusion of the process parameter group. c) Exclusion of the spatter region index group. d) Exclusion of the edge proximity index (epi) group. 46

Figure 3-11: Confusion matrix generated by a) RF, b) GB, c) XGB, d) SVM, e) NN, and f) LSTM on unseen test set. 49
Figure 3-12: Receiver operating characteristic (ROC) curve generated by a) RF, b) GB, c) XGB, d) SVM, e) NN, and f) LSTM on unseen test set. 51
Figure 3-13: Effect of the train set size on the models' performance on unseen test set. a) Weighted F1-score. b) Macro F1-score. 53
Figure 3-14: Comparative assessment of random forest feature importance across different input feature combinations, distinguished by color to represent four distinct input feature groups. a) All four groups employed. b) Exclusion of the process parameter group. c) Exclusion of the spatter region index group. d) Exclusion of the edge proximity index (epi) group. (Note: C1-C6 denote clustered light intensity) 55
Figure 4-1. Layout of part locations on the build plate for replicates A and B. As an example, part 2 (replicates A and B) is highlighted. 59
Figure 4-2. Schematic of light intensity data collection during Melt Pool Monitoring (MPM), showing datapoints recorded across the x-y plane and the concept of the Edge Margin Zone (EMZ) for the Front Side 61
Figure 4-3. Illustration of the Edge Margin Zone (EMZ) concept with three values (120, 280, and 400 μm) marked with (*). Color coding (red for Front, blue for Left, cyan for Back, and green for Right) represents the data collected from each side, highlighting the top 5 mm of the part. 62
Figure 4-4. Flattening process to convert 2D layered data into a continuous 1D signal, shown for the Front Side as a representative example and sequentially ordered from the bottom to the top of the area of interest. 63
Figure 4-5. Illustration of the feature extraction process (input) and surface roughness measurement (output) for the top 5 mm of the part. Input: Time-domain and frequency-domain features extracted from the 1D signal of each vertical side. Output: Representative Sa values averaged from five discrete points per side, serving as ML model outputs. 64
Figure 4-6. Conventional vs. proposed methods for surface roughness prediction: process parameters only vs. process parameters with in-situ features, including time-domain and frequency-domain features extracted from light intensity signals (MPM) 69
Figure 4-7. Flowchart of the model training and hyperparameter optimization process. 72

Figure 4-8. Surface roughness (Sa) distributions for the four vertical sides (Front, Left, Back, Right) of two build plates: (a) Build Plate 1, (b) Build Plate 2. The Right Side shows a narrower, more uniform distribution, while the Front, Left, and Back Sides exhibit broader distributions, with the Back Side shifted toward higher roughness values. Differences between build plates highlight the influence of external factors. 74
Figure 4-9. Evaluation of average R^2 and standard deviation of R^2 across different cluster numbers (N) and edge margin zones (EMZ) using 5-fold cross-validation for (a) XGB and (b) RF models. Optimal performance is achieved at EMZ = 120 μm and N = 3, indicating the most accurate and stable predictions for surface roughness. 77
Figure 4-10. Violin plots of R^2 (a) and RMSE (b) for five models using 5-fold cross-validation with EMZ = 120 μm and N = 3. XGB and RF achieve the highest accuracy and lowest error with minimal variability, outperforming the other models. 78
Figure 4-11. Predicted vs. true Sa values (a, c, e, g, k) and residual plots (b, d, f, h, m) for XGB, RF, SVR, GPR, and FNN models on the unseen test set. RF achieves the highest consistency with the fewest residuals near the ±10% threshold, highlighting its superior predictive accuracy. 80
Figure 4-12. Side-wise evaluation of the best models (XGB and RF) using Mean Absolute Percentage Error (MAPE) and Mean Absolute Error (MAE) on the unseen test set. RF demonstrates better performance across all sides, with the Back Side and Right Side showing the lowest errors due to their distinct and uniform Sa distributions. 82
Figure 4-13. Performance comparison of models on the unseen test set with different combinations of input features (PP, frequency-domain, and time-domain) using R^2, MAE, RMSE, and MAPE. Combining all feature groups results in the highest R^2 and lowest error metrics, demonstrating the effectiveness of integrating in-situ features with process parameters. 84
Figure 4-14. Sensitivity analysis of training set size on model performance on the unseen test set, showing improvements in R^2 and RMSE as the training size increases for all models. GPR and RF achieve the best accuracy and lowest errors. 85
Figure 4-15. Feature importance analysis for XGB and RF models. XGB relies heavily on process parameters (67.6%), while RF emphasizes time-domain features (67.2%). Although XGB shows a strong reliance on process parameters, using only process parameters results in an R^2 of 0.35, highlighting the importance of integrating in-situ features to improve performance, increasing R^2 to 0.76. (Note: C1-C3 represent the centroids of three clusters of light intensity using SOM). 87

List of Tables

Table 2-1. Different types of defects in LPBF. 8
Table 3-1: Selected hyperparameters and their defined range 42
Table 3-2: Comparative performance on unseen test set and training times of models 52
Table 4-1. Process parameters and corresponding VED values, calculated using $VED = PV.h.t$ (layer thickness t = 0.04 mm) 58
Table 4-2. Hyperparameters explored for each ML model, their definitions, ranges, and final selected values used in this study. 73

Chapter 1. Introduction

1.1. Motivation and Challenges

Laser Powder Bed Fusion (LPBF), a key additive manufacturing (AM) process, is widely adopted in industries such as aerospace, healthcare, defense, and automotive due to its ability to produce complex geometries with tailored material properties while reducing costs and lead times. However, one of the persistent challenges in LPBF is surface roughness, which critically influences fatigue resistance, tensile strength, corrosion behavior, and overall part durability. To mitigate these issues, costly post-processing methods are often necessary [1], [2]. Interestingly, in some applications such as heat exchangers and biomedical implants, controlled surface roughness can be advantageous, improving cooling performance and osteointegration.

Surface roughness in LPBF consists of two critical aspects: top surface roughness and vertical surface roughness. While significant research has focused on top surface roughness, vertical surface roughness remains largely unexamined despite its critical role in heat transfer efficiency, tensile behavior, and dross formation. This lack of attention is primarily due to the inherent difficulty of monitoring vertical features in real-time, as conventional optical methods struggle with visibility constraints imposed by powder layers.

To ensure part quality, two primary quality assurance approaches are employed in LPBF: ex-situ inspection (post-process measurement) and in-situ monitoring (real-time defect detection). In-situ monitoring is particularly advantageous as it provides real-time feedback, allowing for immediate process parameter adjustments such as laser power and scan speed, to mitigate defects as they arise. This approach enhances production efficiency, reduces post-processing costs, and is increasingly becoming integral to industry certification workflows [3], [4].

Existing in-situ monitoring methods predominantly rely on cameras, which have been extensively used for defect detection, melt pool analysis, and geometric accuracy assessment. However, camera-based systems are limited by trade-offs between field of view and resolution, sensitivity to ambient light, and the requirement for controlled lighting conditions. Additionally, camera images are often large in size and require significant data reduction to extract relevant features. Moreover, cameras are incapable of capturing vertical surface roughness, as powder layers obscure vertical features, making direct visual assessment impractical.

This research directly addresses these critical gaps by introducing a novel photodiode-based in-situ monitoring system for both top and vertical surface roughness assessment, marking a significant advancement over existing methods. While photodiodes have been previously used in LPBF for melt pool monitoring, their potential for surface roughness detection has remained largely unexplored. Compared to cameras, photodiodes offer higher sampling frequencies, robustness in dusty environments, and the ability to detect light intensity variations that correlate with surface roughness formation. Their adaptability for reflective materials like titanium and copper makes them particularly suitable for LPBF applications, when optical monitoring faces limitations.

By addressing these gaps, this research not only advances in-situ monitoring capabilities in LPBF but also sets a foundation for improved process control, quality assurance, and application-specific roughness optimization. The ability to accurately monitor and control both top and vertical surface roughness in real-time has profound implications for the AM industry, enabling enhanced part functionality while reducing reliance on costly post-processing techniques.

1.2. Objectives

The primary objective of this study is to develop an in-situ prediction platform for both top and vertical surface roughness using photodiode signals during LPBF. This study pioneers two key innovations in in-situ monitoring:

1. Photodiode-based in-situ monitoring of top surface roughness – While prior studies have exclusively used cameras for this purpose, this research introduces a photodiode-driven approach, leveraging its ability to capture real-time surface signatures with higher efficiency and adaptability. Unlike previous methods that measured roughness in selected areas, this study predicts surface roughness at a fine resolution (690 μm × 510 μm) across the entire top surface, capturing critical variations including edges and corners, for a more comprehensive and accurate roughness assessment.
2. First-ever in-situ monitoring of vertical surface roughness – Unlike top surface roughness, vertical roughness has received minimal attention, and no existing studies, whether camera-based or otherwise, have successfully implemented a real-time monitoring technique. This

work establishes a photodiode-based method capable of detecting side light intensity variations, enabling vertical roughness estimation for the first time.

Figure 1-1 and Figure 1-2 illustrate the graphical abstracts of the first and second objectives, respectively. To achieve these objectives, the following steps were pursued:

- Developing a design of experiments (DoE) framework to generate various surface roughness conditions by modifying process parameters such as laser power, scanning speed, and hatch distance.
- Preprocessing light intensity data collected from an in-situ co-axial photodiode and extracting key features.
- Measuring surface roughness for both top and vertical surfaces using a laser scanning confocal microscope.
- Applying machine learning algorithms to correlate photodiode signals with measured surface roughness.
- Testing and validating the trained machine learning models for accurate roughness prediction.

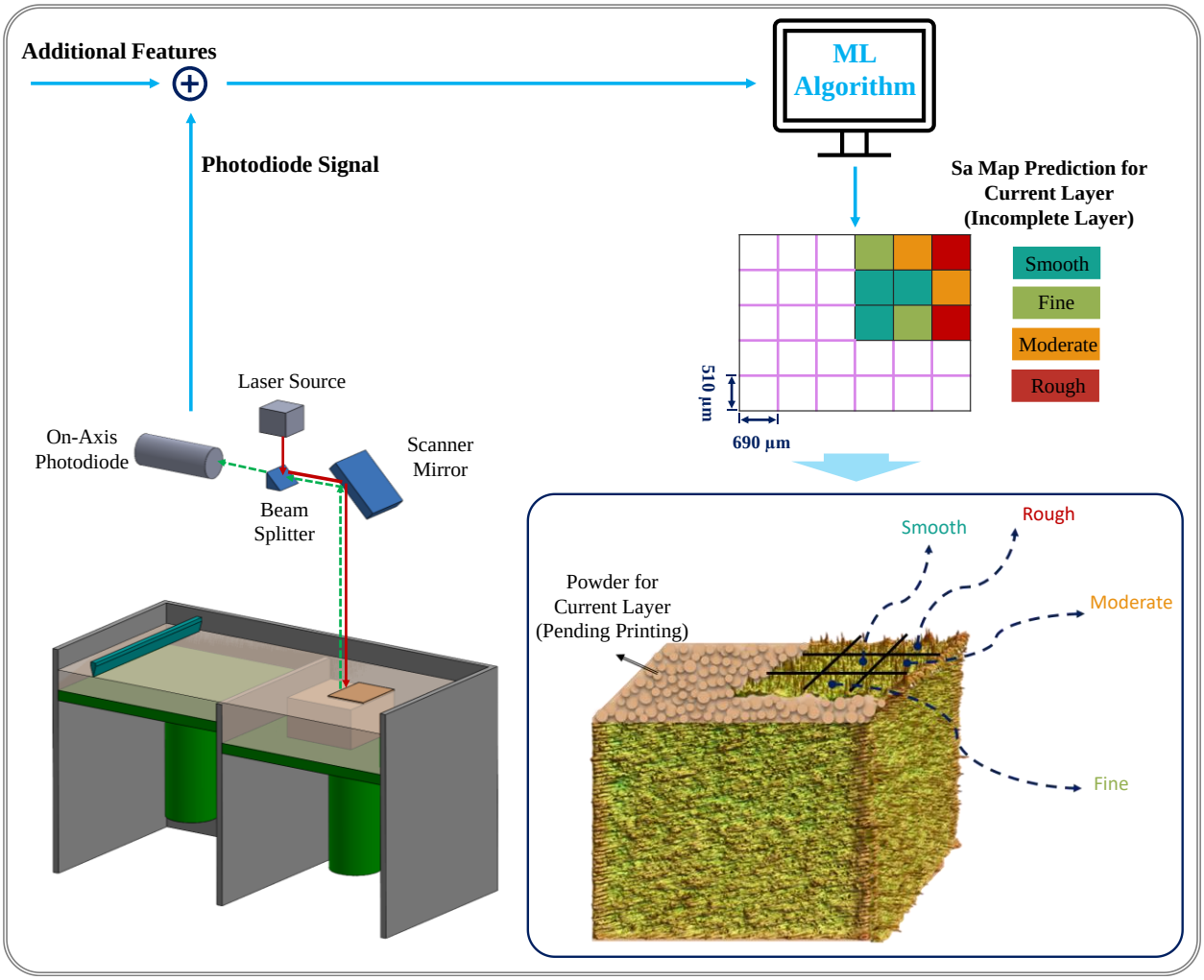


Figure 1-1. Graphical illustration of the first objective of the present study. The photodiode signal at each point is captured and integrated with additional features. This combined data serves as input for a machine learning model, which predicts the Sa value categorized into four classes. This methodology enables Sa class predictions for every small area (690 µm × 510 µm) of the top surface, including edges and corners across each layer. In this illustration, while the layer is incomplete, the model predicts the Sa class for the printed area, with the remaining regions awaiting data to complete the prediction map for that layer [5].

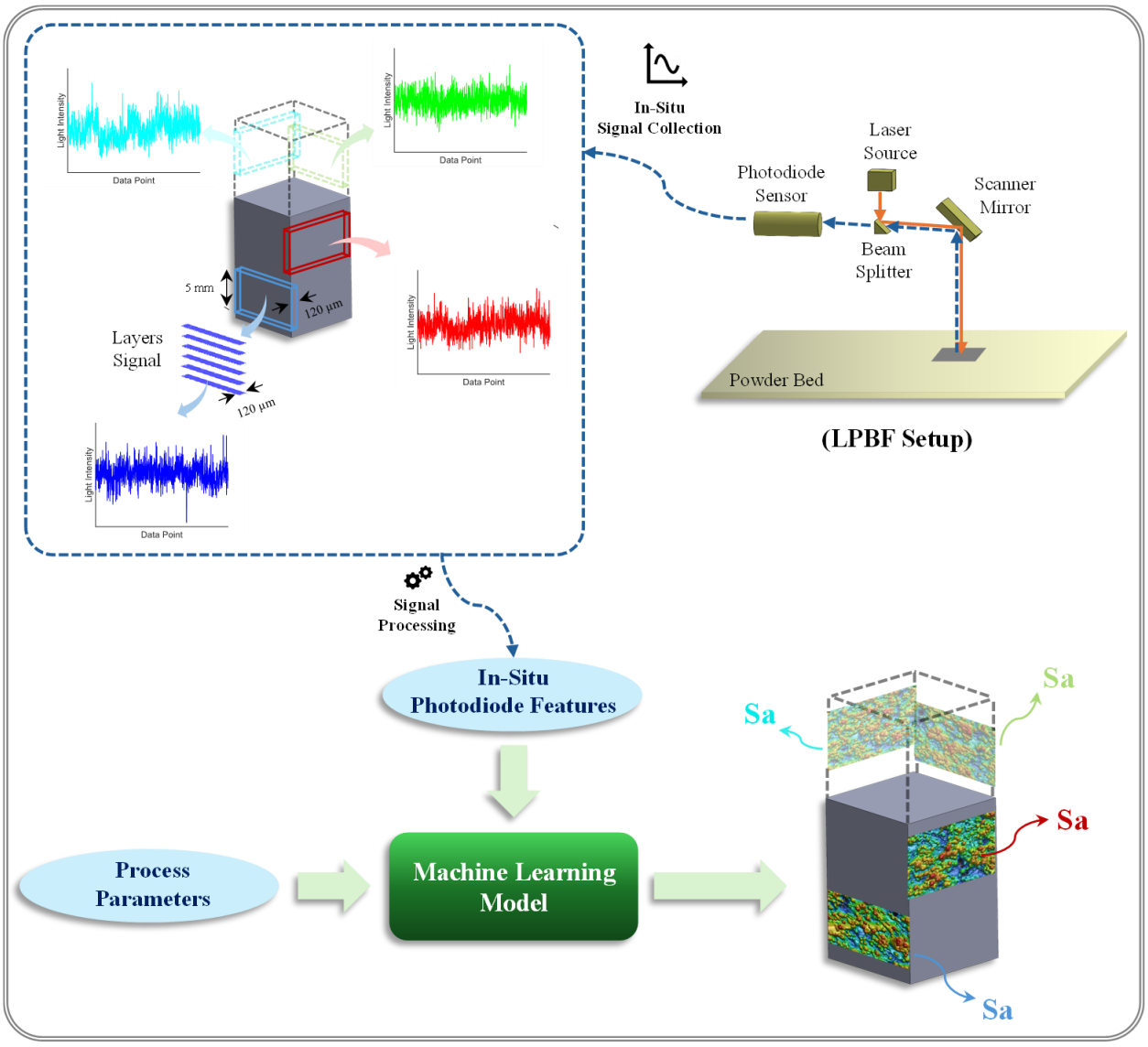


Figure 1-2. Graphical illustration of the second objective of the present study. By selecting any vertical side and any specific region of interest along that side, light intensity signals are collected from areas near the edges of the chosen region. Through signal processing, key features are extracted and integrated with essential process parameters to predict the surface roughness of the vertical side within the specified region of interest.

1.3. Thesis Outline

The thesis is comprised of five chapters. Chapter 1 introduces the motivation for the study, the challenges faced, and the objectives outlined. Chapter 2 presents a comprehensive literature review, covering challenges in LPBF and the in-situ monitoring techniques used in LPBF. It further discusses previous research on both ex-situ and in-situ surface roughness prediction for both top and vertical surfaces. Chapter 3 details the development of an in-situ platform for top surface roughness prediction using various ML algorithms and a photodiode sensor in LPBF. Chapter 4 outlines the experimental procedures and ML model development for the prediction of vertical surface roughness in LPBF using a photodiode sensor. Finally, Chapter 5 summarizes the conclusions of the research, evaluates how the objectives were met, and discusses potential future work.

Chapter 3 and Chapter 4 are adapted from the author's published work and manuscripts submitted for publication, as follows:

- Chapter 3 is a journal article published in the Journal of Additive Manufacturing:
  Sahar Toorandaz, Katayoon Taherkhani, Farima Liravi, Ehsan Toyserkani. A novel machine learning-based approach for in-situ surface roughness prediction in laser powder-bed fusion. Additive Manufacturing, 2024.

- Chapter 4 is an article that has been submitted to the Journal of Manufacturing Systems:
  Sahar Toorandaz, Farima Liravi, Osazee Ero, Ehsan Toyserkani. A Pioneer Machine Learning-Driven Platform for In-Situ Vertical Side Surface Roughness Prediction in Laser Powder Bed Fusion.

The content of these publications has been slightly modified to fit within the scope of this thesis. The license agreements are provided in the letter of copyright permissions section.

Chapter 2. Literature Review and Background

2.1. Abstract

LPBF, a type of Additive Manufacturing (AM) technique, enables the production of complex, high-density parts. However, defects such as surface roughness remain a challenge, affecting properties like fatigue life, durability, and dimensional accuracy. Real-time monitoring using in-situ sensors and machine learning has become essential for enhancing process understanding and improvement. This chapter provides an overview of LPBF, and the common defects found in fabricated parts. It also briefly discusses in-situ monitoring and machine learning techniques in LPBF and reviews existing studies on surface roughness prediction for both top and vertical surfaces.

2.2. Additive Manufacturing (AM) and Laser Powder Bed Fusion (LPBF)

Additive Manufacturing (AM) is a process that creates 3D objects layer by layer using CAD or 3D scanning. It offers several advantages over traditional manufacturing, such as the ability to produce complex geometries, unique properties, and reduced cost and lead time, making it widely adopted in academia and industry.

A highly advanced AM technology is powder bed fusion (PBF), which uses a heat source to selectively melt and fuse powder layers into solid objects. The process involves spreading thin layers of powder with a re-coater and selectively scanning each layer with a laser or electron beam. PBF is categorized into laser powder bed fusion (LPBF) and electron beam powder bed fusion (EPBF), depending on the energy source used.

LPBF is among the most widely used AM techniques due to its ability to process a broad range of metallic materials and produce high-density, high-quality complex parts [6]. Its versatility makes it a preferred choice for manufacturing industries across various sectors.

2.3. Defects and Process Challenges in LPBF

Despite significant advancements, LPBF continues to face fundamental challenges due to the presence of defects in printed parts. These defects remain critical issues, ultimately impacting the performance, reliability, and quality of the final product. The formation of these defects in metal LPBF processes is influenced by various parameters, including laser power, scanning speed, scan

strategy, hatch spacing, re-coater speed, and gas flow [7], [8]. Defects in LPBF can be broadly categorized into two types: volume defects and surface defects. Volume defects, such as keyholes and irregular pores, can alter mechanical properties and compromise the internal integrity of the part. Surface defects, on the other hand, result in increased roughness, affecting surface quality, dimensional accuracy, and fatigue resistance. Table 2-1 presents examples of common defects in LPBF.

Extensive research has been conducted to improve part quality through trial-and-error methods and process parameter optimization. However, these approaches are often costly, inefficient, and unable to fully address persistent challenges. Key issues, such as accurately predicting and controlling internal defects or achieving surface roughness within a desirable range, remain unresolved. Additionally, external factors such as gas flow, spatter, and powder uniformity introduce further complexities, leading to unpredictable variations in part quality. Addressing these challenges requires innovative solutions that go beyond traditional optimization approaches to ensure consistent and reliable outcomes.

Table 2-1. Different types of defects in LPBF.

Defect category	Defect type	Significant formation reasons	Ref.
Volume	Spherical pores (gas holes)	Gas entrapment, including: • Nitrogen in starting powders • Argon trapped in the process • Evaporation of low melting elements in alloys	[9], [10], [11], [12]
	Keyholes	• High power and low scanning speed • Excessive volume energy density	
	Irregular pores (lack of fusion)	• Low power and high scanning speed • Very low volume energy density	[9], [13]
Volume & Surface	Crack	• Extensive columnar grains under high-stress conditions • Higher scan speed and scan length • Material voids during cyclic loading by acting as stress concentration sites • Untreated or coarsely treated powder	[9], [14], [15], [16], [17], [18]

Surface	Balling	• Low laser power and high scanning speed • Low energy density • Non-preheated powder • Small particles of powder • Increase in solute oxygen in the chamber	[16], [17], [19], [20]
	Lack of overlap	• High hatch spacing • Low laser power	[21]
	Partially melted-adhered particles	• Ejection of spatters from the melt pool (Low scanning speed and High laser power, leading to increased spatter formation) • Contact between a hot surface and un-melted powders, especially on the side surfaces of a part	[22], [23], [24]

2.4. Quality Assurance in LPBF

Quality assurance (QA) is a key approach to achieving enhanced quality in AM products. The first step toward effective QA is improving process understanding. To address the challenges associated with traditional trial-and-error methods, in-line melt pool monitoring (MPM) devices are integrated into laser-based AM systems. These devices provide real-time data on key process features collected through sensors, enabling better control of part quality [25]. However, the massive amount of data generated, millions of data points per layer, necessitates the use of data mining algorithms for effective analysis. Therefore, real-time sensing, documenting, and analyzing these datasets are crucial for improving QA. Data collected during the LPBF process can be analyzed using various algorithms, with machine learning gaining significant attention in recent years for its speed and accuracy. Machine learning has been applied to several aspects of LPBF, including process optimization, defect detection, and surface roughness prediction [26].

This section provides an overview of different types of sensors commonly used in LPBF processes, with a particular focus on the photodiode sensor employed in this study, along with a brief overview of machine learning methods.

2.4.1. In-situ Sensors

In metal LPBF processing, various sensors are used to measure some process parameters, such as radiative rays, temperature, rate of solidification, and the size of the melt pool. These parameters are correlated with the quality of the printed parts and can be classified into two categories: radiative and non-radiative sensors [25], which are briefly described in the following.

2.4.1.1. Radiative Sensors

Radiative sensors detect radiation emissions emitted from the melt pool, which is extensively used in AM process. Common types of radiative sensors include photodiodes, pyrometers, cameras, inline coherent imaging (ICI), and X-ray imaging. There are several significant properties of these sensors, among which high reliability, fast response, and resistance to dust can be highlighted.

2.4.1.2. Non-Radiative Sensors

Non-radiative sensors detect the physical characteristics of the process without using radiation emission from the printed part. Examples of non-radiative sensors include thermocouples, acoustic sensors, and displacement sensors. In this type of sensor, the physical nature and dynamics of the process can be converted into an electrical signal.

In this study, the commercial photodiode is used, and its characteristics are discussed in the following section.

- **Photodiode**

In metal AM, photodiodes are extensively used because of their low cost and ability to provide valuable information on the process. They can monitor light emission and thermal radiation by converting photons into an electrical current [27], [28]. This current is dependent on the applied voltage, absolute temperature, Boltzmann constant, and electron charge [25]. Figure 2-1 illustrated a schematic of LPBF equipped with on-axis and off-axis photodiodes. The on-axis photodiode is aligned with the laser beam path through a beam splitter, and the off-axis is fixed and mounted on the roof of the building chamber. The photodiodes collect light intensity in the visible and near-infrared ranges emitted from the melt pool [29], [30], [31], [32]. The corresponding PC also records and stores laser modulation and X/Y scanner position data in addition to light intensity data [33].

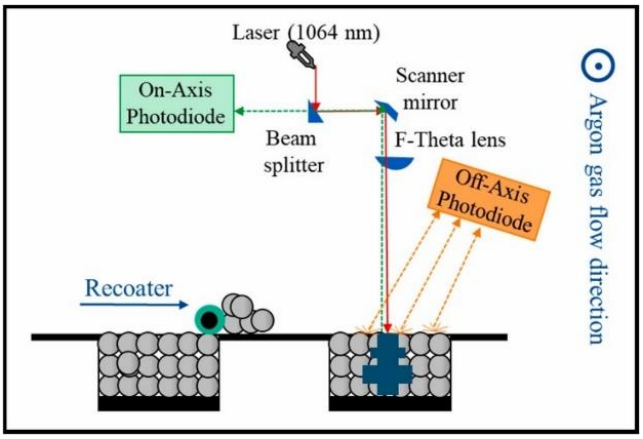


Figure 2-1. Schematic of LPBF equipped with on-axis and off-axis photodiodes [33].

2.4.2. Overview of Machine Learning

Machine learning (ML) is a type of artificial intelligence (AI) and computer science that imitates the way humans learn by using data and algorithms, gradually improving its accuracy. In general, there are three main types of learning in machine learning systems: supervised learning, unsupervised learning, and reinforcement learning [34], which are briefly described in the following section.

2.4.2.1. Supervised Learning

Supervised machine learning relies on labeled input and output training data to identify the relationship between them. This technique can be divided into two types of classification and regression. A classification model maps input to discrete output, while a regression model predicts continuous output. Some of the known supervised learning algorithms include k-Nearest Neighbors, Linear Regression, Decision Trees, Random Forests (RF), Gradient Boosting (GB), and Neural Networks (NN).

2.4.2.2. Unsupervised Learning

Unlike supervised learning, there is no clear and complete labeled dataset for unsupervised learning, and it analyzes unlabelled or raw data. The objective of this approach is to explore the underlying patterns and predict the output. This method is a kind of self-organized learning that tries to find hidden features and cluster the data in a meaningful way. The following are some of the commonly used algorithms in this method include Self-Organizing Map (SOM), Principal Component Analysis (PCA), K-Means, and Singular Value Decomposition (SVD).

2.4.2.3. Reinforcement Learning

The reinforcement learning technique is very different from other learning approaches. There is a learning system, called an agent, that can observe the environment, decide, take actions, and get rewards or penalties based on its choices. Then, the most efficient strategy, called a policy, must be determined by itself to gain the maximum reward over time. An agent's policy specifies what action should be taken in certain situations.

To analyze the data collected from sensors in LPBF, machine learning provides an effective approach for developing predictive models. As previously mentioned, a key application of machine learning in LPBF is in-situ defect monitoring, which has been widely researched. However, real-time surface roughness prediction remains less explored, likely due to the inherent challenges associated with detecting surface morphology during the printing process. Therefore, the purpose of this study is to develop an approach for in-situ surface roughness prediction during printing using photodiode sensors in LPBF. The next section reviews existing studies on surface roughness prediction for both top and vertical surfaces.

2.5. Surface Roughness Prediction in LPBF

Surface roughness plays a significant role in the overall quality of LPBF-produced parts. It affects key properties such as fatigue [35], tensile strength [36], corrosion [37], durability [38], and porosity [39], [40], highlighting the need for effective surface roughness inspection in LPBF. Surface roughness monitoring and quality control are typically performed using either ex-situ or in-situ techniques. Ex-situ inspection involves post-process evaluation of printed components to assess quality, whereas in-situ monitoring captures real-time data during fabrication. The latter approach utilizes sensors such as photodiodes and cameras installed on LPBF machines to detect surface defects and process variations as they occur [41].

This section reviews studies on the detection and prediction of surface roughness in LPBF, using both ex-situ and in-situ approaches for top and vertical surfaces. Despite advancements in surface roughness monitoring, a gap remains in the literature regarding in-situ surface defect monitoring and control, especially on vertical surfaces.

2.5.1. Ex-Situ Surface Roughness Prediction

2.5.1.1. Top Surface (Ex-Situ)

Ex-situ techniques for monitoring and predicting top surface roughness in LPBF have been widely explored, with a focus on understanding the influence of process parameters on surface quality. Various statistical and machine learning models have been employed to predict surface roughness and optimize LPBF processing conditions. Shan et al. investigated the surface roughness of AlSi10Mg in the LPBF process using RF regression. Experimental samples were fabricated under varying process conditions, including laser power, scanning speed, and hatch distance, with roughness measurements ranging from 2.98 to 11.28 μm. A 2D RF model outperformed a 1D RF model, achieving an R^2 of 0.907, demonstrating that RF regression is effective for surface roughness prediction. Their findings suggest that higher laser power, lower scanning speed, and optimized hatch distance contribute to improved surface quality [42]. Arunadevi et al. applied Bayesian learning and Artificial Neural Network (ANN) classifiers to predict the surface roughness of S30 alloy. A dataset of 30 cube samples was analyzed, considering current, line offset, and scan speed as key process parameters. The ANN model outperformed Bayesian learning, achieving 100% accuracy, while the Bayesian model reached 96% accuracy. Surface roughness was classified as either "Good" (1) or "Bad" (0), though the exact classification threshold was not explicitly stated [43]. La Fé-Perdomo et al. explored the prediction of surface roughness and mechanical properties of 316L stainless steel produced through Selective Laser Melting (SLM). The study assessed the impact of laser power, scanning speed, hatch spacing, and layer thickness on relative density, material hardness, and ultimate tensile strength, employing six different modeling approaches: Response Surface Methodology (RSM), Multi-Layer Perceptron (MLP), Support Vector Regression (SVR), Random Forest (RF), Gaussian Process Regression (GPR), and Adaptive Neuro-Fuzzy Inference System (ANFIS). Their findings showed that GPR provided the most accurate roughness prediction, while MLP excelled in predicting mechanical properties. An ensemble model combining multiple regressors achieved the highest accuracy in predicting relative density and elongation at break, highlighting the benefits of multi-model integration for robust surface roughness prediction [44]. Akhil et al. investigated the surface texture of Ti-6Al-4V in the SLM process using image processing and machine learning. Surface texture parameters were extracted using first-order and second-order statistical analysis of top-surface images. Five regression approaches—Linear, Polynomial, Support Vector Regression (SVR), Gaussian Process

Regression (GPR), and Artificial Neural Networks (ANN)—were compared. Results indicated that GPR provided the most accurate surface roughness predictions, with roughness values ranging from 2 to 32 µm [45]. Khorasani et al. applied ANN modeling to predict Sa surface roughness of Ti-6Al-4V in LPBF. Process parameters included scan speed, laser power, hatch distance, scan pattern increment angle, and heat treatment conditions, with an L25 Taguchi design of experiment (DOE) guiding parameter selection. Figure 2-2 illustrates the real and predicted values of Sa obtained using the ANN algorithm, demonstrating that the model successfully predicted surface roughness trends. The study also revealed that heat treatment above the beta transus temperature significantly increased roughness. The most influential parameters, ranked from highest to lowest, were heat treatment, laser power, scan pattern angle, hatch distance, and scan speed [46]

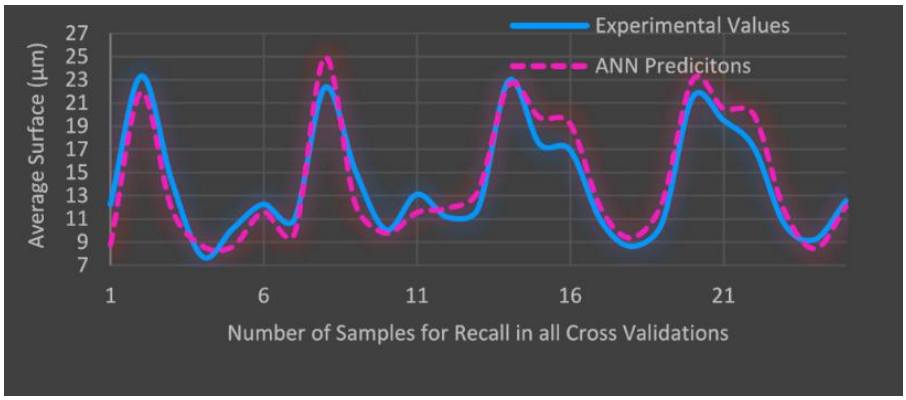


Figure 2-2. Results of ANN modeling for each cross-validation. Figure reproduced from [46].

In a separate study, Khorasani et al. examined the effect of process parameters on surface roughness (Ra) and surface tension of LPBF-processed Ti-6Al-4V, considering perpendicular, parallel, and angled orientations relative to laser movement. A Poisson regression model was employed to predict Ra values, achieving strong correlation with experimental results. Findings showed that surface tension remained consistent across orientations, whereas roughness varied significantly depending on the build direction [47].

Wang et al. applied a heterogeneous hypergraph learning framework to analyze surface defects in LPBF-produced 316L stainless steel and CoCr components. A hypergraph model was constructed using 114 workpieces, capturing relationships among process parameters, material properties, and surface quality. A novel embedding method, exp2vec, extracted low-dimensional feature representations, which were used in a variational graph auto-encoder with correction (VGAE-Corr) for defect prediction. The model outperformed baseline approaches in identifying

porosity, cracks, and unmelted powder, demonstrating the potential of graph-based learning for surface roughness analysis [48]. In another study, Wang et al. developed a physics-based analytical model to predict the upper surface roughness of 316L stainless steel in LPBF. Their approach used an analytical thermal model to estimate melt pool temperature distributions and solidification profiles. By assuming a half-elliptical cap shape for the molten pool, the authors derived an expression for the top surface profile as a function of material properties and process parameters. As shown in Figure 2-3, the predicted Ra values exhibited strong agreement with experimental measurements, validating the cap-based analytical approach for top surface roughness prediction [49]

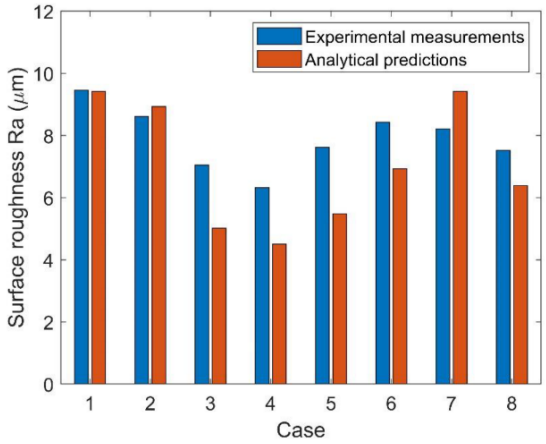


Figure 2-3. Comparison between predicted and measured surface roughness Ra. Figure reproduced from [49].

These studies collectively underscore the importance of machine learning, statistical modeling, and physics-based approaches in ex-situ surface roughness prediction. While regression-based techniques (GPR, RF, and ANN) consistently yield high accuracy, physics-based models offer mechanistic insights into roughness formation. The integration of graph-based learning and hybrid modeling presents a promising avenue for enhancing predictive reliability and process optimization in LPBF.

2.5.1.2. Vertical Surface (Ex-Situ)

Despite the significant impact of vertical surface roughness on the mechanical properties and overall quality of LPBF-fabricated parts, it has been comparatively underexplored in the literature. Recent studies have sought to address this gap by investigating the effects of process parameters, part orientation, and scanning strategies on vertical surface roughness, employing both

experimental characterizations and ML models. Detwiler et al. characterized and predicted the surface topography of Inconel 718 in LPBF using ML models. Their study assessed the influence of bulk laser power, scan speed, layer thickness, and build orientation on surface topography parameters, including summit density, summit height standard deviation, and mean summit radius. Surface roughness was analyzed on multiple as-built surfaces, including vertical side surfaces oriented along the re-coater movement and gas flow direction. Using confocal laser scanning microscopy (CLSM), they compared five ML models—k-Nearest Neighbors (KNN), Decision Trees, Random Forest (RF), Support Vector Machines (SVM), and Artificial Neural Networks (ANN)—against a multivariate regression benchmark. Results showed that Decision Trees (interpretable) and ANN (non-interpretable) achieved the highest prediction accuracy, identifying thermocapillary convection and melt track overlap as key contributors to surface roughness. Their findings highlight that ML-based models provide effective predictive insights for optimizing vertical surface quality, reducing the need for extensive post-processing [50].

Whip et al. investigated the effect of contour laser parameters (laser power and speed) on vertical side surface roughness of LPBF-fabricated Inconel 718. Surface roughness was analyzed using both non-destructive areal measurements and destructive profile measurements, employing ISO 25178 and ISO 13565-1 roughness metrics. Results indicated that higher laser power reduced valley depths, leading to smoother surfaces, while laser speed had a lesser impact. Destructive profile measurements revealed deeper valleys and surface notches that were often obscured in non-destructive areal scans, suggesting that areal methods may underestimate roughness due to powder adhesion artifacts. Their findings emphasize the importance of selecting appropriate measurement techniques for accurately characterizing fatigue-critical surface features [51]. Li et al. explored the impact of energy density and part orientation on the surface roughness of AlSi10Mg LPBF components, analyzing both top and vertical side surfaces. Vertical side roughness was affected by scan strategy, gas flow, and wiper movement, with results showing that roughness initially decreased with increasing energy density but later increased. Optimal surface quality was achieved at an energy density of 175–200 J/mm³, and a 90° scan rotation increment effectively reduced roughness variation across different surfaces. Their study highlights the significant role of part orientation in determining vertical surface quality, with left and back surfaces exhibiting higher roughness due to thermal accumulation and spatter deposition [52]. Ozel et al. examined the surface texture of Inconel 625 produced via LPBF, evaluating the influence of energy density and scan

strategy on both top and vertical side surfaces. Focus Variation Microscopy (FVM) was used to acquire areal height maps for texture analysis. Findings revealed that vertical side surfaces exhibited higher roughness than top surfaces due to powder adhesion and melt track irregularities. Additionally, a 67° scan stripe rotation reduced roughness more effectively than a 90° rotation. The study employed Genetic Programming (GP) and ANN to predict surface texture, with GP achieving better accuracy across most roughness parameters. Their results underscore the importance of optimizing scan strategies and energy input to improve vertical surface quality and reduce post-processing requirements [53]. Masiagutova et al. investigated side surface roughness formation in LPBF of AlSi10Mg, focusing on process optimization and roughness control. The study analyzed the influence of primary (laser power, scan speed, hatch distance) and secondary (contour and compensation settings) process parameters on vertical roughness. As shown in Figure 2-4, the roughness distribution on different sides of a produced cube was analyzed. The study also demonstrated that vertical surfaces exhibited higher roughness than top surfaces due to melt track geometry, powder adhesion, and process instabilities. By optimizing volumetric energy density (VED: 60–85 J/mm³) and contour scanning strategies, vertical roughness Sa was reduced from 40 to 10 µm. Additionally, positive compensation values were found to improve surface quality by mitigating melt pool irregularities and balling effects. Their findings highlight that careful tuning of process parameters can significantly enhance vertical surface quality, reducing reliance on extensive post-processing [54].

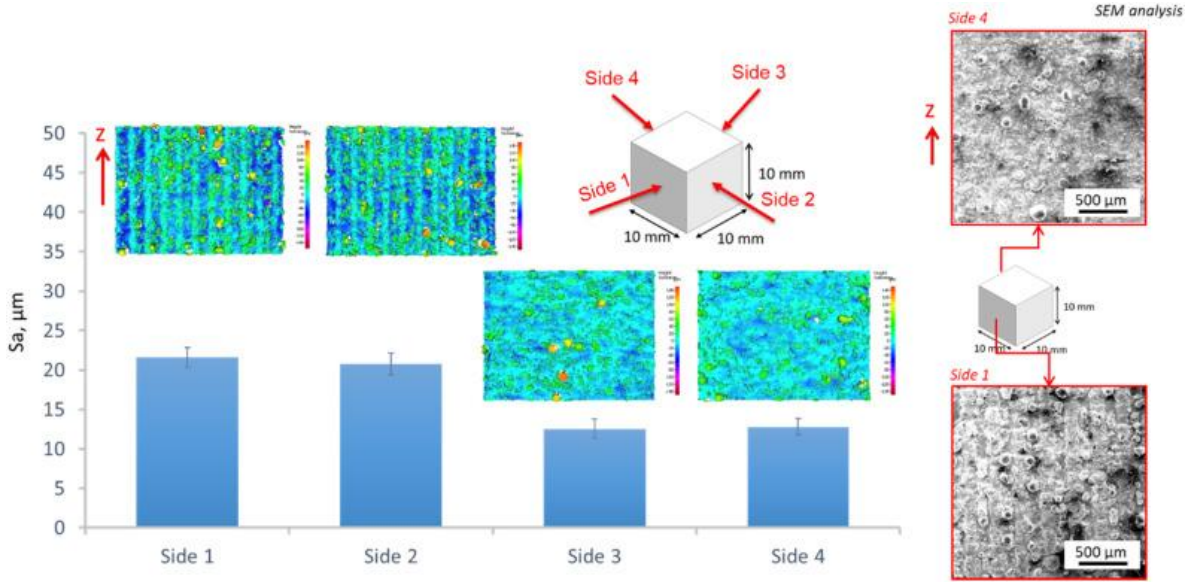


Figure 2-4. Roughness distribution on different sides of one produced cube. Figure reproduced from [54].

Rott et al. explored the interdependency between surface orientation and laser incidence in LPBF, introducing a novel surface laser relation angle (ζ) to predict and homogenize surface roughness. Their study examined Inconel 718 samples built on an EOSINT M290 system, analyzing roughness variations across multiple build orientations, including vertical side surfaces. Results indicated that laser incidence angle strongly influences surface roughness, with vertical side surfaces exhibiting greater roughness due to melt pool geometry and powder adhesion. By maintaining a constant ζ angle, roughness Ra was reduced from 19 μm to 11 μm, with a standard deviation reduction from 5 μm to 2 μm. Their findings suggest that optimizing laser incidence can enhance vertical surface predictability and consistency, minimizing roughness variations and the need for extensive post-processing [55].

Collectively, these studies highlight the critical influence of process parameters, scanning strategies, part orientation, and laser incidence on vertical surface roughness in LPBF. While machine learning and statistical models have been successfully applied to predict and optimize surface quality, additional experimental and analytical research is required to develop robust solutions for minimizing vertical roughness. Future work should focus on integrating in-situ monitoring, advanced data-driven modeling, and process parameter optimization to further improve the surface quality of LPBF-fabricated components.

2.5.2. In-Situ Surface Roughness Prediction

2.5.2.1. Top Surface (In-Situ)

In-situ monitoring and prediction of top surface roughness in Laser Powder Bed Fusion (LPBF) have gained increasing attention due to their potential to enhance process control and reduce post-processing efforts. Various optical, thermal, and machine learning-based techniques have been employed to track and analyze layer-wise roughness evolution and its correlation with process parameters, spattering behavior, and melt pool dynamics. DePond et al. pioneered the use of high-speed spectral domain optical coherence tomography (SD-OCT) to measure layer-to-layer surface roughness in LPBF-fabricated 316L stainless steel. Their study assessed the effects of scan rotation, spatter particles, laser power, and energy density on roughness evolution. As shown in Figure 2-5, scan rotation significantly reduced roughness accumulation, minimizing porosity formation regardless of the scan strategy. Additionally, spatter particles introduce high points in the powder bed, which may persist on the melted surface of subsequent layers. The study also revealed that

high-energy density conditions lead to excessive dross, while low-energy density conditions promote balling and capillary-driven coalescence, both of which degrade surface quality [56].

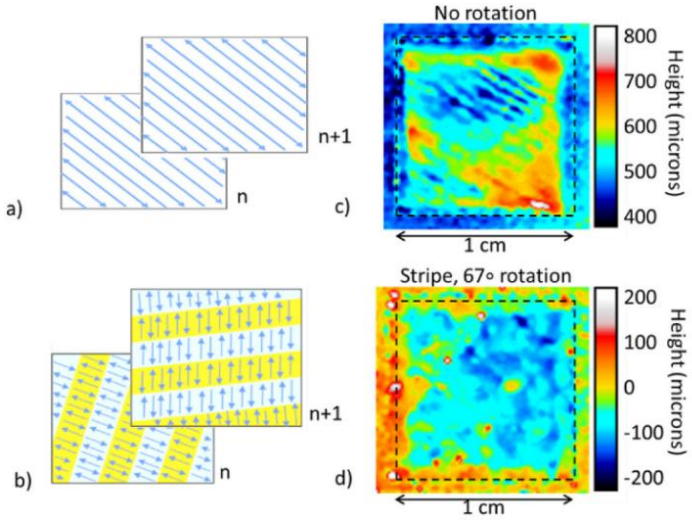


Figure 2-5. Impact of scan strategy on surface roughness: a) Simple bidirectional scan strategy with no rotation between layers, used for Cube 1. b) Stripe scan strategy with 67° rotation between layers, used for Cube 2. c) 2D height map for layer 22 of Cube 1. d) 2D height map for layer 22 of Cube 2. Figure reproduced from [56].

Fleming et al. investigated real-time tracking and control of surface morphology in LPBF using Inline Coherent Imaging (ICI). Their approach enabled immediate roughness measurement per layer, with defects identified based on height distribution variations. Two correction techniques were implemented: laser ablation for raised defects and powder refilling for depressions. Their findings demonstrated that active correction strategies effectively reduce surface roughness, enhancing the uniformity of layer deposition [57]. As illustrated in Figure 2-6, the height distribution of several layers is shown before and after correction, where a more homogeneous color after correction indicates a smoother surface. Raihan et al. developed an augmented surprise-guided sequential learning framework (CT-SurpriseAF-BO) for predicting melt pool geometry, which directly impacts top surface roughness. Their Bayesian optimization framework employed a novel surprise-guided acquisition function to optimize data collection, minimizing the number of required experimental runs. Additionally, a Conditional Tabular Generative Adversarial Network (CTGAN) was used to generate synthetic data, improving prediction accuracy without additional physical experiments. The CT-SurpriseAF-BO model outperformed traditional machine learning techniques, demonstrating its potential for real-time surface roughness optimization and LPBF process control [58].

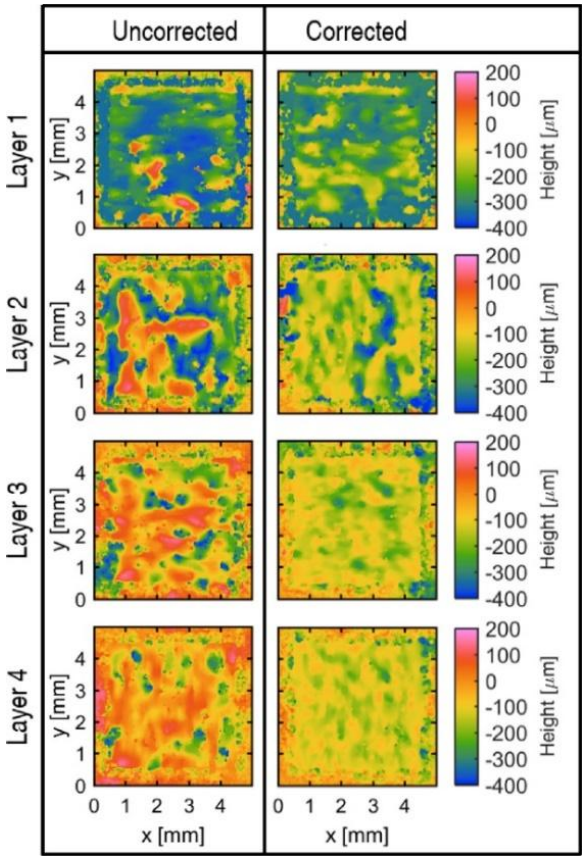


Figure 2-6. Height distribution of Layers 1 through 4, before and after correction using Inline Coherent Imaging (ICI), Figure reproduced from [57].

Gerdes et al. utilized a convolutional neural network (CNN) and a hyperspectral imaging system to predict surface roughness (Rz) in LPBF-fabricated magnesium alloy WE43. Their experimental dataset comprised 40 samples with three different parameter sets, capturing a range of surface roughness values. Hyperspectral images were correlated with confocal microscope-measured Rz values, and the trained CNN model achieved a mean absolute error (MAE) of 4.1 μm, demonstrating its capability to accurately predict surface roughness from in-situ imaging data [59]. Yan et al. explored the relationship between in-situ thermal signatures and surface roughness using high-speed infrared (IR) imaging. Their study extracted temperature gradients, maximum temperatures, and temperature standard deviations from melt pool IR images and correlated these metrics with local surface roughness. A machine learning model trained on experimental data identified a strong correlation between temperature gradients and surface roughness, highlighting the potential for thermal monitoring-based roughness prediction and real-time process optimization [60]. Knaak et al. investigated the prediction of Inconel 718 surface roughness using high-dynamic-range (HDR) optical imaging combined with CNN-based classification. A dataset of 44 samples,

each divided into 16 sections, was collected, with each section labeled according to surface roughness measurements. Roughness values were categorized into five distinct classes, with Class 1 representing the smoothest surfaces (0–3 μm roughness). Their CNN model achieved over 80% classification accuracy, demonstrating that HDR imaging and deep learning techniques can effectively predict surface roughness variations [61].

Bhatt et al. conducted an in-situ characterization of surface roughness evolution during multilayer LPBF of Ti-6Al-4V using synchrotron X-ray imaging and optical imaging. Their findings showed that surface roughness is multimodal and multiscale, influenced by pre-layer humping, spattering, and rippling defects. The study introduced a surface topology matrix combining eight roughness metrics, such as Ra, Rq, skewness, and melt pool size ratio, to describe surface evolution more effectively. Results indicated that linear energy density (LED) significantly impacts top surface roughness, with optimal surface quality achieved by balancing energy input to minimize spattering and waviness effects [38]. Qu et al. utilized in-situ synchrotron X-ray imaging to analyze the effect of nanoparticles on melt pool behavior and top surface roughness in LPBF of Al6061 + TiC nanoparticles. Their results demonstrated that TiC nanoparticles dampen surface waves, reduce melt pool turbulence, and improve smoothness by increasing viscosity and controlling melt flow dynamics. A 68% reduction in surface roughness was achieved due to nanoparticle-induced wave damping, highlighting the potential of nanoparticle-based process modifications for real-time surface roughness control [62]. Zhang et al. investigated melt pool spattering and its influence on in-process layer roughness using a lab-designed Fringe Projection Profilometry (FPP) system. By correlating melt pool spatter characteristics (e.g., count, ejection angle, and spatial distribution) with measured surface roughness, they developed a machine learning-based segmentation model to automatically extract spatter features from in-situ imaging. Their roughness prediction model, which incorporated spatter count and volumetric energy density (VED) as inputs, achieved a 50% error reduction compared to conventional process-parameter-based models. Their findings suggest that in-situ spatter monitoring can enhance LPBF process control, reducing surface roughness variability and defect formation [63]. In a related study, Zhang et al developed a machine learning-enhanced high-dynamic-range (HDR) Fringe Projection Profilometry (FPP) method for in-situ layer-wise surface topography measurement in LPBF. Their HDR projection-based approach mitigated shadowing and intensity saturation artifacts common in traditional FPP imaging. Additionally, machine learning models, including Residual Dense

Networks (RDN) and Denoising Diffusion Probabilistic Models (DDPM), were employed to improve resolution from 38 μm to 5 μm laterally and from 10 μm to 1 μm vertically. Results indicated that DDPM-SR3 outperformed other models, yielding the most accurate surface reconstructions and enabling real-time defect detection. Their study highlights that ML-enhanced HDR-FPP can significantly improve in-situ top surface monitoring, providing higher accuracy and resolution for LPBF process optimization [64].

These studies collectively demonstrate that in-situ monitoring techniques, ranging from optical and thermal imaging to machine learning and X-ray-based analysis, offer significant advantages in predicting and controlling top surface roughness in LPBF. Advanced deep learning models, Bayesian optimization, and nanoparticle-driven melt control are emerging as powerful tools for real-time surface quality assessment and defect mitigation, ultimately enhancing the reliability and repeatability of LPBF-fabricated components.

2.5.2.2. Vertical Surface (In-Situ) - No Studies Available

Despite significant advancements in in-situ monitoring for top surface roughness in LPBF, no prior studies have specifically investigated real-time measurement or prediction of vertical surface roughness. This gap in research is likely due to technical challenges, including limited sensor accessibility, difficulty in capturing high-resolution side surface data, and the complex interaction of process parameters affecting vertical roughness formation. Current in-situ monitoring techniques, such as high-speed imaging, fringe projection profilometry, and thermal monitoring, primarily focus on top surface evolution, where data acquisition is more straightforward.

To address this gap, the present study aims to develop an in-situ vertical surface roughness prediction framework for LPBF. By leveraging signal processing from photodiode sensor and machine learning models, this research seeks to provide real-time roughness monitoring and process optimization for vertical surfaces, which is crucial for improving part quality and reducing post-processing requirements.

2.6. Summary

This chapter provided an overview of LPBF and the common defects that occur in fabricated parts. These defects can be broadly categorized into volume defects and surface defects, with the latter significantly contributing to surface roughness, which affects the overall quality of the printed components. To mitigate these defects, real-time process monitoring using various sensor

technologies has been explored. By leveraging machine learning algorithms, researchers have sought to establish correlations between in-situ process data and defect formation, enabling the prediction and reduction of surface roughness. However, existing studies on surface roughness prediction in LPBF, whether ex-situ or in-situ, remain limited. This limitation may be attributed to the challenges of detecting and analyzing surface structures during fabrication, particularly in real-time. Further research is needed to overcome these challenges and develop more effective monitoring and prediction methods. Notably, no prior studies have specifically addressed the in-situ measurement or prediction of vertical surface roughness. This research gap underscores the need for innovative approaches to extend in-situ monitoring capabilities beyond the top surface, ultimately enhancing process control, defect prevention, and part quality in LPBF.

Chapter 3. A Novel Machine Learning Based Approach for In-situ Surface Roughness Prediction in Laser Powder-Bed Fusion

3.1. Abstract

Controlling and optimizing surface roughness remain a significant challenge in laser powder bed fusion (LPBF). Surface roughness affects printed part quality, particularly fatigue life, leading to costly post-processing. Nevertheless, tailored roughness can be beneficial to specific fields in engineering and medicine, such as cooling or osteointegration. Consequently, the importance of quality assurance, in-situ monitoring, and automatic anomaly detection has been elevated among the users of the LPBF process. In-situ surface roughness detection remains a less explored area within all in-situ defect detection. Additionally, existing studies primarily employ camera-based methods, which come with inherent limitations, including sensitivity to ambient light conditions, compromises between resolution and field of view, and the requirement for additional equipment such as adaptive optical filters. This study pioneers using a photodiode sensor, offering faster response times for real-time surface roughness prediction. Integrating this sensor with machine learning (ML) algorithms establishes a robust framework for surface roughness prediction. The methodology involves analyzing the captured light intensity from the melt pool by a on-axial photodiode and incorporating additional process variables into ML models to predict surface roughness within each small area of the printed part (690 μm × 510 μm), even at edges and corners. Multiple ML algorithms are trained and rigorously validated with unseen data. This comprehensive analysis encompasses the impact of process parameter variations on a wide range of surface roughness values, affirming the efficiency of the proposed methodology.

3.2. Methodology and Data Preprocessing

3.2.1. Design of Experiment

In this study, parts were manufactured utilizing commercially available Ti-6Al-4V powder supplied by AP&C (a GE additive company) with the particle size distribution of D10 < 19.53 μm, D50 < 35.52 μm, and D90 < 51.29 μm. The manufacturing process was carried out using an EOS M290 LPBF machine (EOS GmbH, Krailling, Germany) for the printing of the parts. Cuboid parts, with dimensions of 10 × 10 × 15 mm (L×W×H), were designed, and surface roughness was varied by adjusting the process parameters. These parameters included a combination of laser power (125,

150, 175 W), scanning speeds (1000, 1250, 1500 mm/s), and hatch distances (0.06, 0.08, 0.1 mm), resulting in a total of 27 different configurations. Layer thickness was fixed to 40 micron and the scanning strategy for all parts was a rotated stripe scanning strategy, with a stripe-width of zero and without any skin. Based on pre screening experimentation, only the parameters with a Volume Energy Density (VED) falling within the range of 25 to 50 J/mm^3 were retained, resulting in 21 distinct process parameters. The VED was calculated by Eq. 3-1:

$$VED = \frac{P}{V.h.t} \qquad \textit{Eq. 3-1}$$

where P is power (W), V is scanning speed (mm/s), h is hatch distance (mm), and t is layer thickness. It should be noted that the VED is not an independent parameter as the layer thickness is fixed.

The build plate consists of two replicates of parts, labeled as A and B, resulting in a total of 42 parts which are labeled by their number (from P1/A to P21/A and from P1/B to P21/B). In Figure 3-1, the selected process parameters were shown, sorted by descending VED values, along with the corresponding location of each part. The location of each part was chosen based on maximizing the distance between two replicas to consider the potential effects of spatter, which will be discussed in Section □.

Part Name	Power (W)	Scanning Speed (mm/s)	Hatch Distance (mm)	VED (J/mm3)
P10	150	1250	0.06	50.00
P19	175	1500	0.06	48.61
P8	150	1000	0.08	46.88
P16	175	1000	0.10	43.75
P17	175	1250	0.08	43.75
P13	150	1500	0.06	41.67
P3	125	1250	0.06	41.67
P1	125	1000	0.08	39.06
P9	150	1000	0.10	37.50
P11	150	1250	0.08	37.50
P20	175	1500	0.08	36.46
P18	175	1250	0.10	35.00
P6	125	1500	0.06	34.72
P2	125	1000	0.10	31.25
P4	125	1250	0.08	31.25
P14	150	1500	0.08	31.25
P12	150	1250	0.10	30.00
P21	175	1500	0.10	29.17
P7	125	1500	0.08	26.04
P5	125	1250	0.10	25.00
P15	150	1500	0.10	25.00

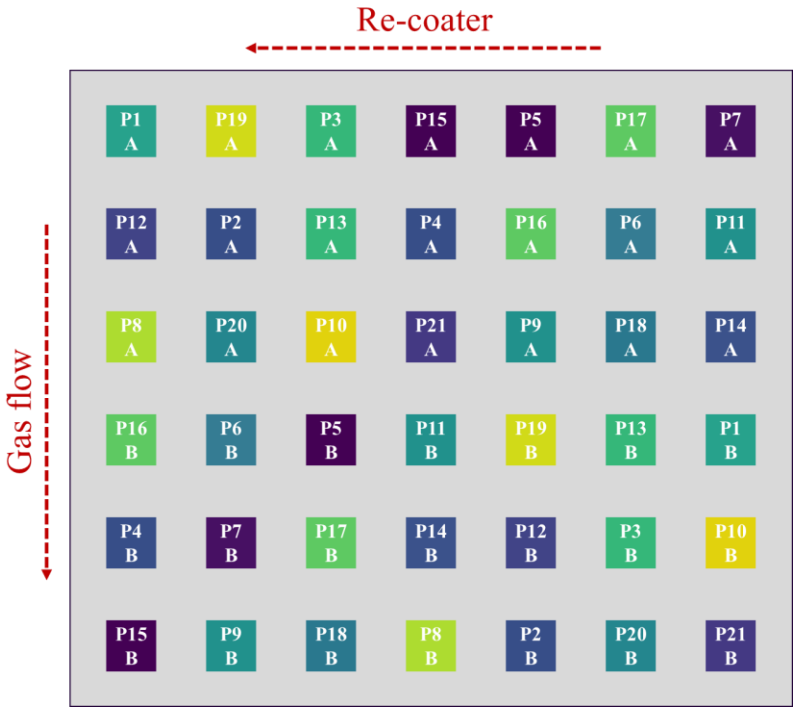


Figure 3-1. Process parameters, sorted by descending VED values, aligned with part locations (replicates A and B).

3.2.2. Data Collection

The data collection process consisted of two steps:

- The first step involved collecting light intensity data during the printing process using an in-situ monitoring on-axial photodiode sensor.
- The second step involved measuring the height of each point from peak to valley of the entire top surface of the printed parts through a laser scanning confocal microscope (LSCM), to calculate *Sa*.

The graphical illustration of data collection is shown in Figure 3-2 and will review in Sections 3.2.2.1 and 3.2.2.2. This collected data is used to extract input features and outputs for ML algorithms that can be employed for the next step of analysis.

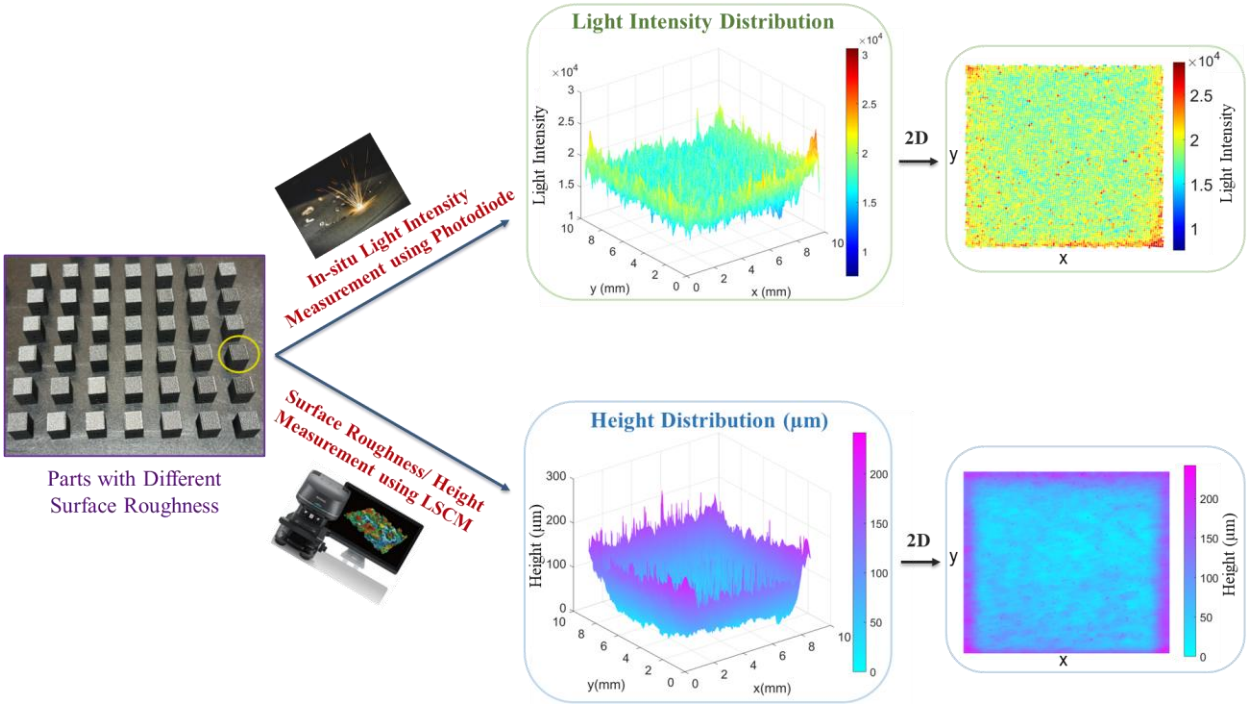


Figure 3-2. Visual representation of data collection process. Step one: Capturing light intensity data during printing with an in-situ monitoring photodiode sensor. Step two: Measuring the entire top surface height of parts using a laser scanning confocal microscope (LSCM).

3.2.2.1. In-situ Light Intensity Measurement

In this study, a commercial on-axial photodiode integrated into the EOS M290 machine was used with a sampling frequency of 60 kHz. For example, for a processing speed of 1250 mm/s, the distance between two points where the data is collected is 21 microns. On-axial photodiode captures the light intensity signals from the melt pool in the 750 – 900 nm wavelength range [65].

The light intensity distribution for the last layer of one of the parts is displayed in Figure 3-2, and it can be seen that the values differ based on the point. The light intensity is a 1D signal, which can be mapped to the build plate geometry based on recorded *x* and *y* positions to represent a spatial distribution.

It is worth noting that this study focused specifically on the light intensity of the last three layers, a deliberate choice driven by the significant impact of pre-layer issues such as humping and spattering on surface roughness. Based on our team's prior research, it was discovered that defects like lack of fusion can be effectively monitored by examining the light intensity up to three layers where these defects occur [66]. Consequently, in this study, which is primarily focused on the top layer surface roughness, the light intensity of the last three layers was considered to provide crucial insights.

3.2.2.2. Height Measurement of the Top Surface of Printed Parts

As shown in Figure 3-2, the second step of data collection for this study involves obtaining the height values of the top surface to calculate surface roughness. Measurements were conducted using a Keyence LSCM (Keyence, Osaka, Japan). LSCM is a non-destructive technique, which measures non-contact height profile, roughness, and film thickness on any material or shape in nanometer-level resolution. Compared to conventional widefield microscopy, it offers several advantages. In addition to allowing control over depth-of-field, it allows the collection of serial optical sections from thick specimens. The confocal microscope can also be used to create 3D images of structures [67], [68], [69]. These advantages make it ideal for measuring surface roughness on LPBF parts. The setup also includes a *20X* objective lens with a field of view of 709.6 μm × 532.2 μm to capture higher-quality images. An assembly mode was used to collect multiple image data by moving the measurement cell and assembling the data into one image with a surface area of 10 mm × 10 mm, covering the entire top surface. In this case, only the height distribution of the surface from peak to valley is extracted, and all desired surface texture parameters [70], [71] can be calculated using any programming language. In this study, *Sa* was considered as a surface roughness parameter calculated using Eq. 3-2.

$$Sa = \frac{1}{A}\iint_{A} |Z(x,y)|dxdy \qquad \textit{Eq. 3-2}$$

where *A* is the evaluation cell, i.e., the area over which the roughness is measured, *Z(x,y)* is the difference between the roughness profile height and the mean plane at any given position (*x*,*y*).

3.2.3. Correlation between the Collected Data

As previously discussed, the study involves two data collection steps: capturing in-situ light intensity during printing using a photodiode and measuring post-print height distribution of surface with an LSCM. The subsequent analysis aims to determine if there is any correlation between the in-situ light intensity and the height distribution of the top surface of printed parts. This investigation attempts to explore connections between real-time monitoring of the melt pool dynamics and the final surface characteristics of the printed parts.

Figure 3-3 shows the light intensity of the three top layers (layers N, N-1, and N-2) and the height distribution of top layer (layer N) in Parts P10/A, P19/B, P13/A, P1/B, P18/A, P4/B, and P5/A. This selection includes both replicates of A and B and covers a diverse range of VED values. The order in the figure is arranged from the highest to lowest VED. Each part follows a distinct color order on the color maps, attributed to specific processing parameters yielding diverse ranges of light intensity, as explained in Section 3.2.1. The light intensity data, originally in one dimension, is transformed into a 2D plot using *x* and *y* coordinates, where the color signifies the magnitude of light intensity at each corresponding point. Additionally, the figure illustrates the height distribution of the top surface (the top layer) of each part, which has its specific color map order due to different ranges of height. The height data was a 2D matrix based on the *x* and *y* positions, with the color representing the magnitude of the height.

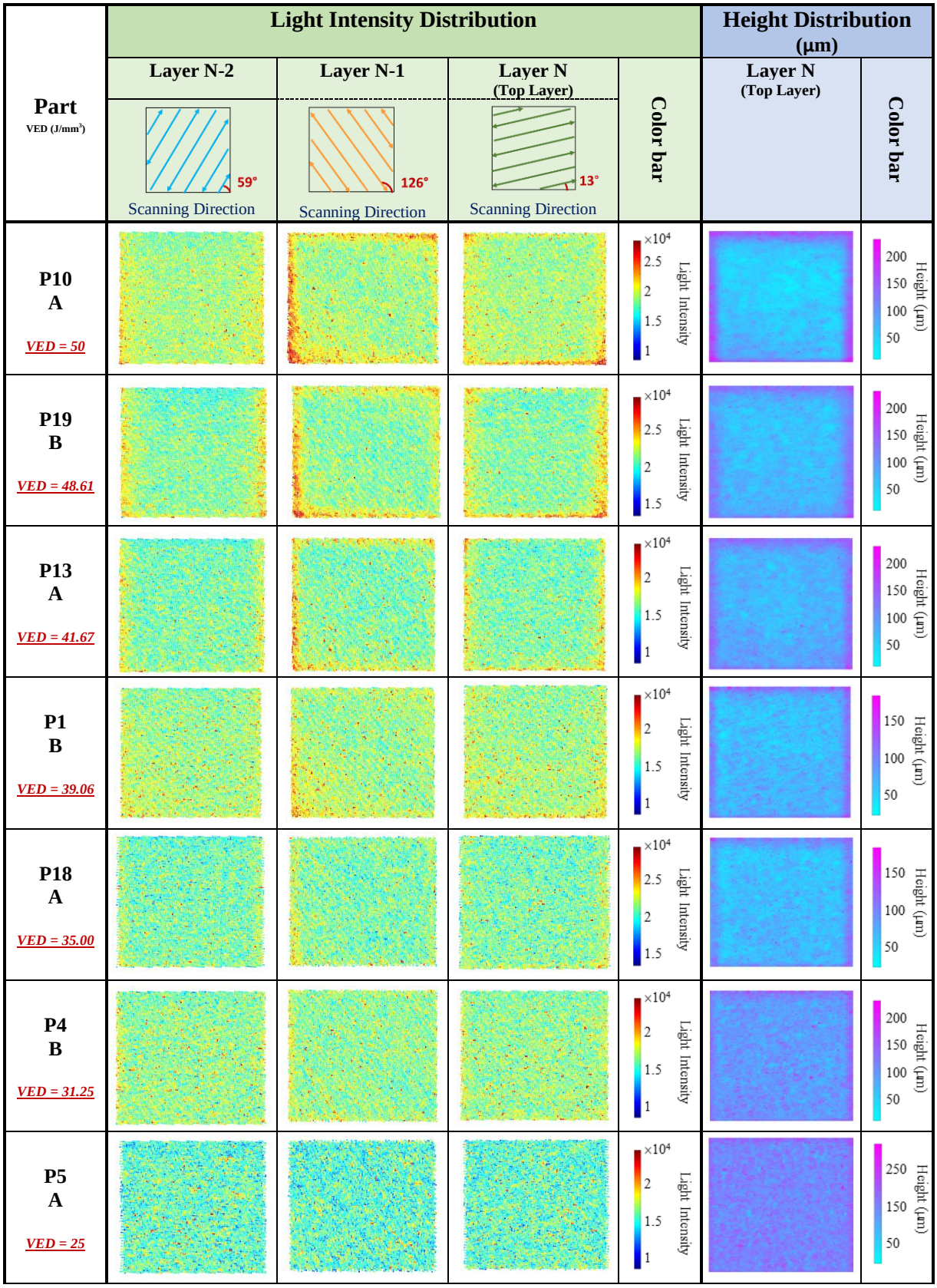


Figure 3-3. Light intensity distribution of the last three layers and height distribution of the top layer for some parts.

Upon analyzing Figure 3-3, it becomes evident that the light intensity distribution is significantly influenced by VED and partially by the scan direction in each layer. The laser back-and-forth paths over a short distance can result in heat accumulation, leading to increased light intensity at the edges/corners. As seen, this effect is more pronounced in parts with a higher VED. For instance, in Parts 10/A, 19/B, and 13/A, which have a higher VED, there is greater light intensity at the corners and edges. Conversely, in Parts 18/A, 4/B, and 5/A, where the VED is lower, this effect is less noticeable. Another hypothesis regarding the increased light intensity in the corners could be attributed to the dynamics of the melt pool, creating a different angle of light irradiation due to different melt pool variations at hot zones. This phenomenon may result in increased light intensity as measured by the photodiode. Interestingly, this observation correlates with a rise in height as seen in Figure 3-3. The figure demonstrates that a significant contrast in the light intensity between the corners and the core is mirrored in the height distribution. For instance, in Part 10/A, elevated light intensity at corners results in increased heights at those regions. In contrast, in parts where light intensity is more evenly distributed, as seen in Part 5/A, a uniform height distribution is observed, with no notable distinction between edges and the core. This suggests a complex interconnected relationships between the melt pool dynamics, the corresponding light intensity behavior, and surface morphology.

An additional explanation is required to clarify the importance of considering the last three layers of light intensity. If only the last layer (the top layer) of the light intensity data is examined, it may appear that there is not a clear correlation between light intensity and height distribution. However, if the last three layers are analyzed, considering that each layer has a thickness of 40 μm, the cumulative effect of these layers better explains the distribution of heights. As an example, in Part 19/B, layer N-2 impacts the left and right edges, layer N-1 affects the left and top edges, and layer N (the top layer) influences the right and bottom edges.

The observation of the collected data indicates a correlation between light intensity and height data, and thus surface roughness. Therefore, by extracting the feature of the dataset and employing ML algorithms to identify the above-mentioned correlation, it may be possible to predict surface roughness efficiently, which is the aim of this study.

3.2.4. Feature Engineering

Assuming that there is a relationship between light intensity data and height data, an appropriate ML algorithm could be utilized to identify this relationship. Therefore, the next step is to establish

a method for organizing the data into a specific input and output format. To achieve this, the four 2D maps of each part, comprising three maps for the light intensity of the last three layers and one for the associated height data, were segmented into small cells sized at 690 µm × 510 µm, resulting in 266 cells for each map. This specific dimension was chosen to align with the field of view of the 20X objective lens of the LSCM (709 × 532 µm) utilized in the experiment. However, a slight adjustment in the cell dimensions was necessary to ensure the same size for all cells, considering the dimensions of the top surface of the parts (10 × 10 mm). It should also be noted that the top surface area was slightly less than 100 mm², which is mainly attributed to the shrinkage [72], [73]. Figure 3-4 shows an example of how all maps of Part 10/A are segmented into small cells. Due to the large number of cells (266) generated, Figure 3-4 only provides a schematic representation of the segmentation. Each of these small cells corresponds to cells at the same location on the other maps; one of them is bolded. Based on 42 parts, a total of 11,172 (42×266) cells were generated for each layer of light intensity data, and 11,172 cells were generated for the height data. This implies that a total of 11,172 datasets are available for use in any ML algorithms.

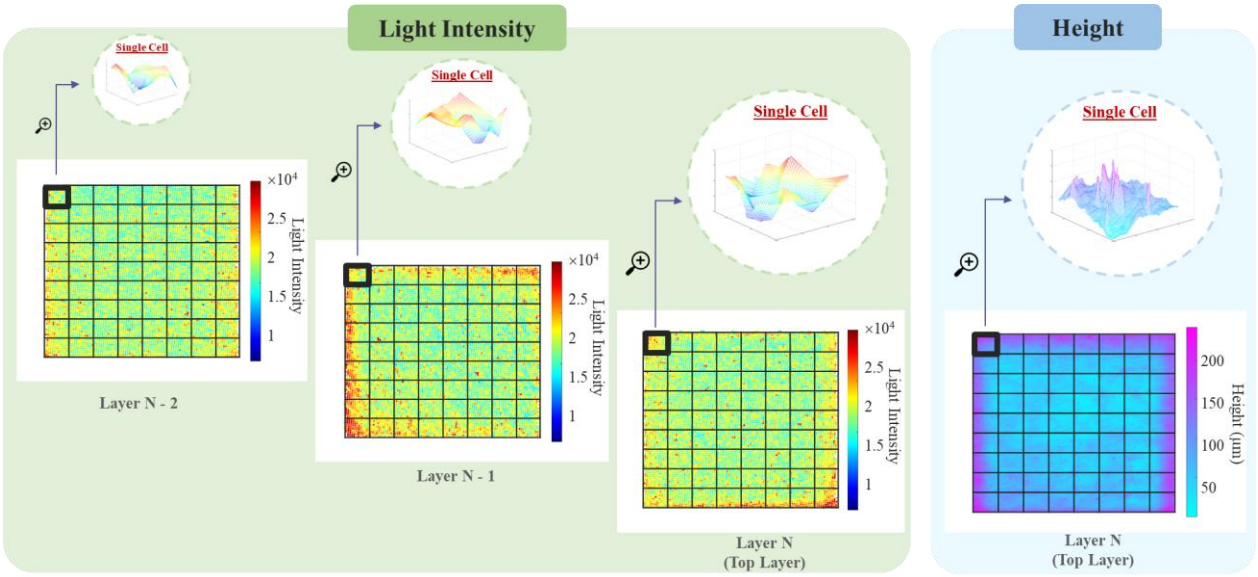


Figure 3-4. An example of the segmentation of light intensity and height distribution of Part 10/A (dimension of each cell is 690 µm ×510 µm). Each cell has a distinct distribution of light intensity or height.

By considering each cell separately, a distinct distribution of light and height can be obtained. The next phase is to extract features from each of these cells (light intensity and height), as outlined in Sections 3.2.4.1 and 3.2.4.2, respectively.

3.2.4.1. Feature Extraction from Each Cell – Input

Each cell is analyzed, and the necessary information are extracted in four steps, as elaborated upon in the subsequent sections.

- **Clustered Light Intensity**

Each cell consists of many data points representing light intensity which may include noise. Rather than utilizing all these data points, extracting key features can be beneficial. Unsupervised clustering algorithms have demonstrated significant potential for a wide range of applications. Using clustering analysis, datasets are grouped based on their similarity. According to the literature, K-means, agglomeration, and Self-Organizing Map (SOM) were applied to cluster in-situ data in LPBF [26], [33], [74]. This study uses SOM to cluster light intensity data for each cell due to its promising results. The SOM algorithm organizes data in a one/two-dimensional grid or map, where each grid unit (or node) represents a cluster or group of similar data points. During training, the SOM learns to map the input data onto this grid by adjusting the weights associated with each grid unit [75], [76]. Since light intensity data is a 1D signal, the SOM input is one-dimensional data. Therefore, applying SOM to 1D data results in clustering the signal into $1 \times N$ clusters.

Different cluster numbers (N=3 to 9) were chosen and applied to the light intensity signal to determine the effect of cluster numbers on the accuracy of the prediction of surface roughness which will be explained in Section 3.3.2. Based on the preliminary observation, six clusters performed better than the others. Figure 3-5 (I) demonstrates an example of the clustered data within a single cell. After clustering the signal into six clusters, the centroid of each cluster, representing the mean of points assigned to that cluster, serves as a representation of the light intensity data points for that specific cell.

- **Process Parameters**

The LPBF technique has numerous process parameters, with some being controllable/adjustable and others not. These parameters, including laser power, scanning speed, powder flow rate, and layer thickness, can significantly impact the final parts quality and properties. [77], [78], [79]. Some of these parameters can be adjusted during the printing process, such as laser power and scanning speed, which can be changed from one layer to the next to optimize the process for different regions of the part [25]. Considering the significant effect of process parameters on surface roughness [80], [81], integrating some key parameters into algorithms can enhance their

effectiveness by making them process-aware. These parameters, selected for their widespread industry usage and ability to be controlled and adjusted within the process, include laser power, scanning speed, hatch distance, and VED.

- **Spatter Region Index**

The location of each part on the build plate affects the quality of the parts, primarily due to the presence of spatters and nonuniform distribution of loose powder particles throughout the bed, which are correlated with the direction of both the re-coater motion and gas flow. Esmaeilizadeh et al. [82] examined how the part location on the build plate affects the surface roughness. They discovered a correlation between increased spattering and higher surface roughness along the re-coater and gas flow directions, identifying a spatter-rich region at their end. To enhance our study, a feature termed the "spatter region index" was introduced that is defined based on both ascending *i* and *j* indices representing the location of each part with respect to the gas flow and the re-coater directions, respectively, as shown in Figure 3-5 (III). In Figure 3-5 (III), one part is highlighted as an example, with the spatter index of i=3 and j=5. Considering the spatter rich zone introduced in [82], this indexing system ensures that the higher values of *i* and *j* correspond to regions with a potentially higher concentration of spatter. Each part is assigned unique *i* and *j* indices, with all cells within a part sharing the same indices for *i* and *j*.

- **Edge Proximity Index (epi)**

The quality of each individual cell of the top layer of a part can be influenced by various factors, such as its proximity to the edges (i.e., relative location of the cell in the given layer). To accurately measure the impact of this factor, a specific variable known as the "edge proximity index" has been defined. This variable considers the proximity of each cell to the edges of the part by dividing the part into four quadrants at the cell of interest (Figure 3-5 (IV)). Then, the number of cells that belong to each quadrant is counted, and four values are obtained (epi1, epi2, epi3, and epi4), reflecting how close the cell is to the edges of the part. For instance, in Figure 3-5 (IV), the highlighted cell values are epi1= 30, epi2= 100, epi3= 80, and epi4= 24, indicating its proximity to the edges. The inspiration for defining this variable in this study came from the research conducted by Kozjek et al. [83]. Kozjek attempted to predict the melt pool temperatures of the next layer using thermometry measurements. They introduced "edge detection," defining a ring around the toolpath point and counting points within four regions. However, our study expanded on this concept by

considering the entire top surface area rather than just a ring and counted cells with a specific dimension instead of counting data points. This modification aimed to provide a more thorough measure of edge proximity.

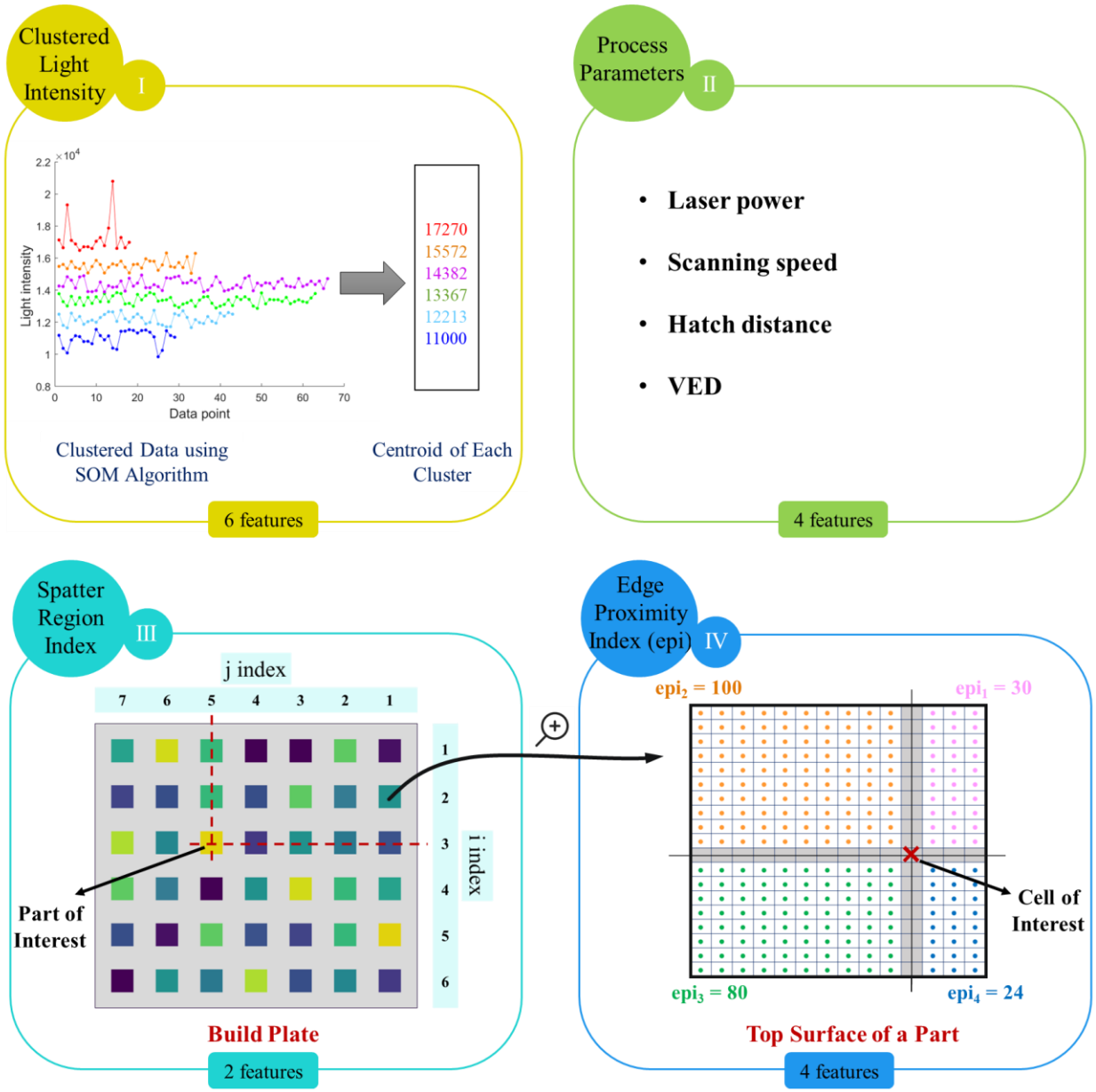


Figure 3-5. Feature extraction from each cell. I) ***Clustered Light Intensity:*** *Clustering light intensity data in a single cell using SOM and calculating the centroid of each cluster. These values are different for each cell, even within one part. II)* ***Process Parameters:*** *Considering some specific process parameters. These values are the same for all cells within one part but vary from part to part. III)* ***Spatter Region Index:*** *Factoring in part location on the build plate and potential spatter presence by utilizing i and j indices. These values are the same for all cells within one part but vary from part to part. IV)* ***Edge Proximity Index (epi):*** *Considering the distance between a cell and the edges of a part through quadrant partitioning at the cell of interest and counting the density of cells in each quadrant. These values are different for each cell, even within one part.*

3.2.4.2. Area Surface Roughness (Sa) Calculation for Each Cell - Output

The primary goal of this study is to predict the *Sa* of individual cells. This involves obtaining the height distribution for each cell and using it to calculate the *Sa* value with Eq. 3-2. Following the *Sa* value computation for each cell, they were divided into four classes (see Figure 3-6 (a)):

- Class 1: $Sa < 8$ µm,
- Class 2: $8 \leq Sa < 14$ µm,
- Class 3: $14 \leq Sa < 22$ µm,
- Class 4: 22 µm $\leq Sa$.

The selection of class ranges was informed by a boxplot, a graphical representation of the distribution of a dataset. After calculating the *Sa* values for all cells (11,172 cells), a boxplot was plotted (see Figure 3-6 (b)), and statistical parameters such as the minimum, lower extreme, first quartile (Q1), median, third quartile (Q3), upper extreme, and maximum were determined. Through several attempts, it was determined that considering minimum to Q1 as Class 1, Q1 to Q3 as Class 2, Q3 to the upper extreme as Class 3, and outliers as Class 4 (notably having fewer data points) yielded promising results. It is worth noting that there was a deliberate decision not to eliminate the outliers, because there was an intention to identify cells with very high surface roughness values for further investigation.

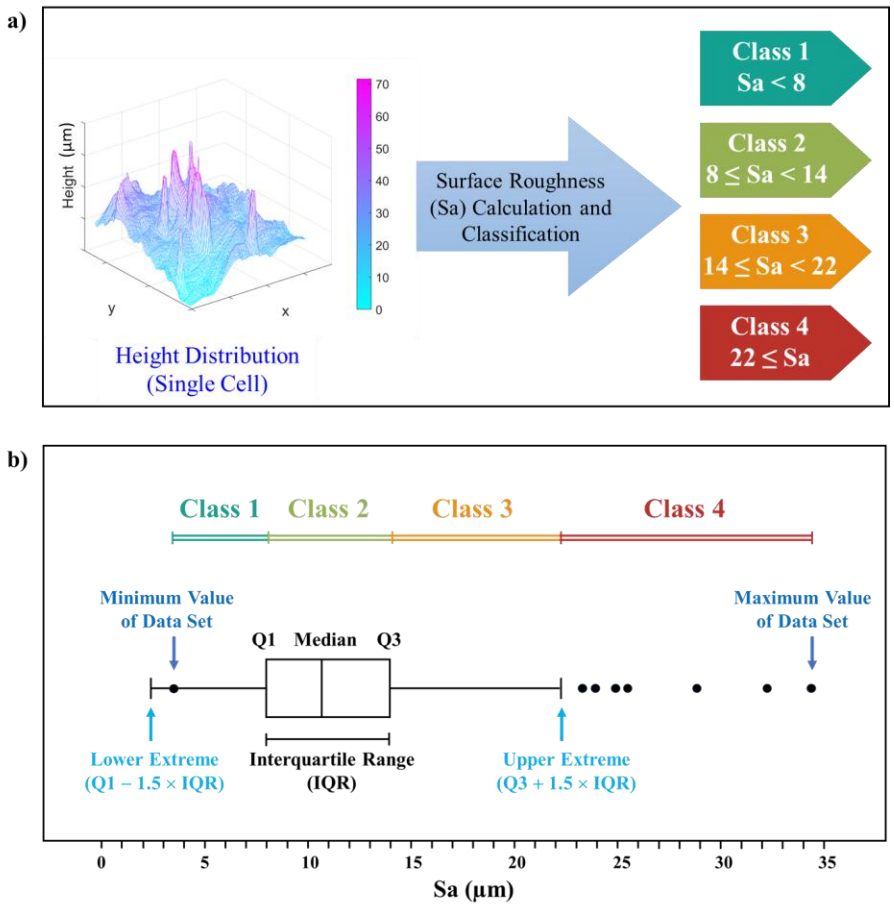


Figure 3-6. a) Quantifying surface roughness (Sa) by analyzing the height distribution of each cell and classifying the results into distinct classes. b) Boxplot diagram displaying Sa values for all cells, highlighting statistical parameters and aligning with the selected range of Sa classes.

3.2.5. Dataset Splitting

Within the set of the 42 parts, totaling 11,172 cells, a decision was made to split the data into training and unseen test sets. Instead of randomly selecting 20% of the total shuffled 11,172 cells (approximately 2,234 cells), which might overly favor optimistic data distribution, a more realistic approach was preferred. Thus, it was determined that setting aside 20% of the total parts, roughly 8 parts, for the unseen test set, corresponding to 2,128 cells. The remaining 34 parts, comprising 9,044 cells, are designated for training purposes. This approach ensures a more realistic representation of data for both training and testing phases, enhancing the reliability and robustness of the model. Notably, the selection of the 8 parts was conducted with a focus on covering a comprehensive range of VED, spanning from low to high.

Given the variations in scale observed within the dataset, normalization or standardization was deemed necessary. Normalization involves rescaling the values of a feature to a range between 0

and 1, while maintaining the relative relationships between data points. This is achieved using the following formula:

$$X_{normalized} = \frac{X - X_{min}}{X_{max} - X_{min}} \quad \textit{Eq. 3-3}$$

On the other hand, standardization transforms features to have a mean of 0 and a standard deviation of 1, using the formula:

$$X_{standardized} = \frac{X - \mu}{\sigma} \quad \textit{Eq. 3-4}$$

where μ is mean and σ is standard deviation of data.

Both methods were applied, and it was found that the standardization method demonstrated better results with increased accuracy. This could be because it helps to center the data around zero and keeps the variation consistent, which seems to suit our dataset better.

3.2.6. Strategies for Handling Imbalanced Data

The categorization of *Sa* into four distinct classes reveals that the samples are not evenly distributed across each class, indicating an imbalance in data per class. For instance, Class 4, has a relatively low frequency. In classification problems, imbalances in the class distribution of training data can lead to poor model performance, as they tend to be biased towards the majority class. To address this, techniques like synthetic minority oversampling technique (SMOTE) [84], [85] and class weights are employed. SMOTE generates synthetic instances for underrepresented classes, while class weights adjust training by assigning higher weights to minority classes [86]. Throughout our analyses, both methods were employed and SMOTE consistently outperformed class weights, improving the F1-score by over 10%.

3.2.7. Implementation of Machine Learning Algorithms

After extracting the features and splitting the training and unseen test datasets, the next phase involves applying various ML algorithms to them. As previously outlined, the input features fall into four distinct groups: the clustered light intensity data group with six features, the process parameters group with four features, the spatter region index group with two features, and the edge proximity index group with four features, totaling 16 features. The algorithms output represents the *Sa* class. Therefore, a dataset comprising 11,172 cells (9,044 trainset and 2,128 testset), with 16 input features was utilized to assess various ML algorithms. Multiple algorithms, including Random Forest (RF), Gradient Boosting (GB), eXtreme Gradient Boosting (XGB), Support Vector

Machine (SVM), feedforward Neural Network (NN), and Long Short-Term Memory (LSTM) were employed on the data.

As discussed earlier, it is crucial to note that the light intensity of the last three layers were considered. A question may arise regarding how these three layers should be treated. To address this, it is essential to mention that while all feature extractions are performed for all three layers, only the first group of features (clustered light intensity) differs among the three layers. The other groups (process parameters, spatter region index, and edge proximity index) remain constant across the three layers.

The choice of the algorithm determines how the data from the three layers should be utilized. For instance, in LSTM, a sequence-based algorithm, these three layers can be treated as a sequence. However, in other models like RF and GB, a sequence cannot be used. In such cases, the light intensity of these three layers was weighted and averaged per each cell.

Figure 3-7 illustrates inputs and outputs for any algorithms, excluding those that can use a sequence like LSTM, and demonstrates how the clustered light intensity of the three layers is combined. The values of the weights for the layers were selected as 0.6 for layer N, 0.2 for layer N-1, and 0.1 for layer N-2, based on our team's previous studies [33], [66]. These studies revealed that in the case of lack of fusion, the first layer displays this defect three times more than the second layer, and the second layer shows it twice as much as the third layer. It was assumed that this observation could be extended to surface roughness, which is influenced by previous layers, leading to the calculation of these coefficients.

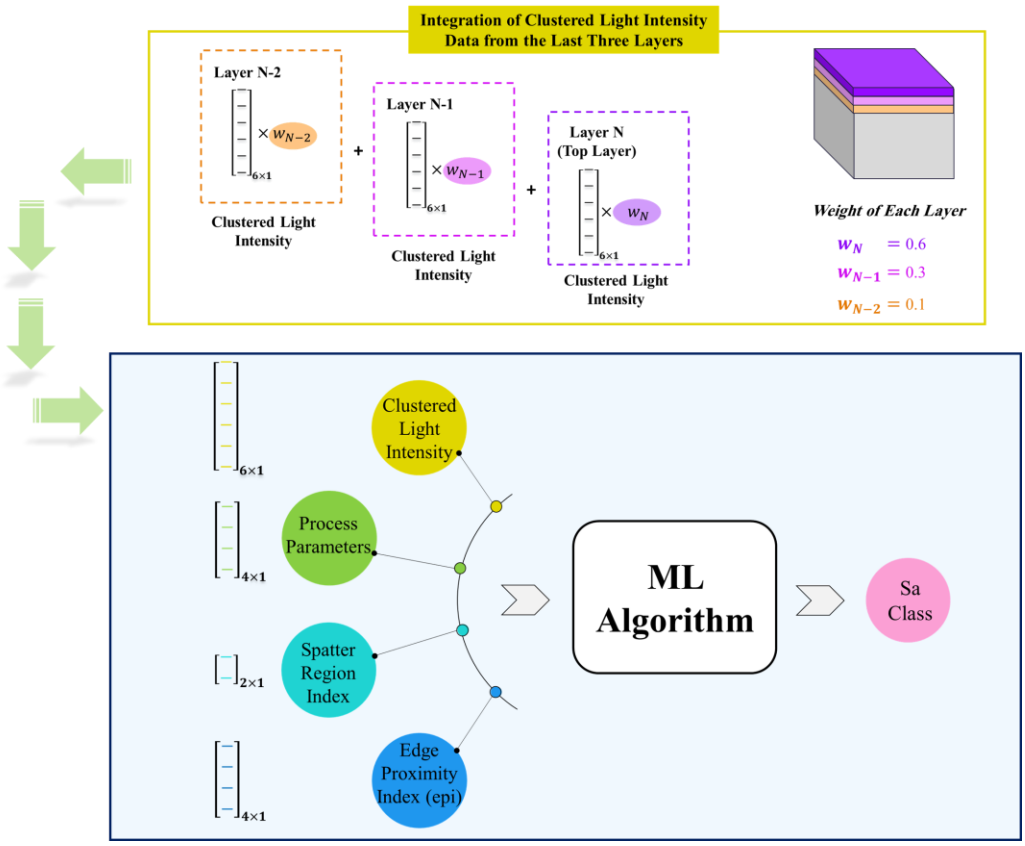


Figure 3-7. An illustration depicting the application of a ML algorithm, showing input features and output, along with the process of combining the first group of features for the last three layers. Note that the other feature groups remain constant across all layers.

The following section provides brief introductions to the ML algorithms used, with a more detailed discussion of their performance in Section 3.3.

3.2.7.1. Random Forest (RF)

The RF model consists of many decision trees that classify data. During training, each tree is built on a random subset of the dataset, making its own predictions. These predictions are then combined to produce the final result, enhancing accuracy and robustness.[87].

3.2.7.2. Gradient Boosting (GB)

GB trees improve decision tree performance by using ensemble learning. Each new tree corrects errors of previous ones using gradient descent optimization, aiming to minimize a predefined loss function. This iterative process reduces residuals between predicted and actual values, resulting in higher accuracy than standalone decision trees, albeit at the expense of increased complexity and computational time [88].

3.2.7.3. eXtreme Gradient Boosting (XGB)

XGB is a specific implementation of GB in which the regularization technique is employed to prevent overfitting. This model is known for its efficiency, scalability, and performance optimizations, making it a popular choice in real-world applications [89].

3.2.7.4. Support Vector Machine (SVM)

SVM is a supervised learning method that separates data points by finding the optimal line or hyperplane to maximize the distance between different class points. Initially designed for linear data, SVM now employs various kernel functions to classify complex datasets. [90].

3.2.7.5. Neural Network (NN)

A feedforward NN analyzes complex relationships between input and output data. It uses forward propagation to pass input through layers of interconnected neurons with nonlinear activation functions. Backpropagation adjusts network weights based on error between predicted and actual outputs, improving performance over time. Through this training process, the network learns patterns in data to make accurate predictions or classifications. [91], [92].

3.2.7.6. Long Short-Term Memory (LSTM)

LSTM is a specialized model for time series analysis. Its architecture, with long-short term memory units, retains information over time, effectively capturing short-term dependencies and long-term patterns in sequential data. This makes LSTM more effective than traditional models for processing and interpreting sequential data. [93].

3.3. Results and discussion

3.3.1. Tuning Models Hyperparameters

The performance of a model is significantly affected by selecting appropriate hyperparameters. Therefore, it is crucial to fine-tune them for better results. For this purpose, the widely used Python package GridSearchCV was used to fine-tune hyperparameters for the RF, GB, XGB, and SVM models. Some specific hyperparameters were selected for each model, and corresponding ranges were defined to explore the parameter space comprehensively. Through grid search methodology, various combinations of hyperparameters were systematically evaluated to determine the optimal configuration, thus improving model predictive accuracy.

For the NN and LSTM models, a different approach was employed for finding the best hyperparameters, as GridSearchCV tends to elongate the runtime. The keras_tuner package, specifically designed for hyperparameter tuning with Keras, was utilized for this purpose. By employing advanced techniques such as Bayesian optimization or Random search, the hyperparameter space was thoroughly explored to identify configurations that improved model performance [94]. This careful tuning ensured the NN and LSTM models were finely tuned to capture important data features, making them better predictors.

In Table 3-1, the selected hyperparameters, their brief definitions, and the ranges studied for each model are provided. Throughout the process of optimizing these hyperparameters, efforts were made to cope overfitting by avoiding overly complex model configurations. The table also presents the final selected value of each hyperparameter. All subsequent results and evaluations discussed in the following sections are based on using these values.

Table 3-1: Selected hyperparameters and their defined range

ML Algorithms	Hyperparameters	Definition	Defined range	Value
RF	n_estimators	Number of decision trees in the forest	50-300	100
	max_depth	Maximum depth of each decision tree	[None,10, 20, 30]	None
	min_samples_split	Minimum number of samples required to split an internal node in a decision tree	2-10	2
	min_samples_leaf	Minimum number of samples required to be at a leaf node in a decision tree	1-5	1
	max_features	Maximum number of features considered for splitting at each node in a decision tree	['sqrt', 'log2', None, 'auto']	'auto'
GB	n_estimators	Number of boosting rounds (or trees) to be built	50-300	100
	max_depth	Maximum depth of each tree in the ensemble	3-7	3
	min_samples_split	Minimum number of samples required to split an internal node in a decision tree.	2-10	2
XGB	n_estimators	Number of boosting rounds (or trees) to be built	50-300	100
	max_depth	Maximum depth of each tree in the ensemble	3-7	6
	learning_rate	Step size for updates to prevent overfitting	[0.01, 0.1, 0.3]	0.3
SVM	C	Regularization parameter	[0.1, 1, 10]	1
	Kernel	Type of kernel function	['linear', 'rbf']	'linear'
	gamma	Kernel coefficient	['scale', 'auto']	'scale'
	decision_function_shape	Decision function strategy	['ovr']	'ovr'
NN	num_layers	Number of layers in the neural network	1-5	1
	units	Number of neurons in each layer	32-512	512
	activation	Activation function applied to the output of each neuron	['relu', 'tanh', 'sigmoid']	'relu'
	optimizer	Optimization algorithm used to update weights during training	'adam'	'adam'
LSTM	num_layers	Number of LSTM layers in the network	1-5	1
	units	Number of neurons in each layer	32-512	512
	activation	Activation function applied to the output of each neuron	['relu', 'tanh', 'sigmoid']	'relu'
	optimizer	Optimization algorithm used to update weights during training	'adam'	'adam'
	kernel_regularizer	Regularization applied to the weights of the connections between neurons	[None, 'l1', 'l2']	'l1'
	bias_regularizer	Regularization applied to the biases of the neurons	[None, 'l1', 'l2']	'l1'

3.3.2. SOM Cluster Size Evaluation

As previously mentioned, the first group of input features, i.e., light intensity, was clustered using a SOM algorithm. Within each cell, the light intensity signal was clustered, and the centroids of these clusters were subsequently calculated and employed as features in the models. Subsequently, an investigation was conducted into the impact of varying cluster numbers, ranging from three to

nine, on the effectiveness of the models. Higher cluster values, such as ten or eleven, led to an increase in NaN (Not a Number) occurrences due to insufficient data points within specific cells. To determine the optimal cluster number, cross-validation on the training dataset and evaluation on unseen test data were conducted.

Cross-validation serves as a fundamental method to assess the performance of ML models. Among the commonly employed variants, such as 5-fold, 10-fold, and 20-fold cross-validation, the choice relies on factors such as dataset size, computational resources, and desired precision. In this study, 10-fold cross-validation was employed, dividing the trainset data into ten equal-sized subsets. During each iteration, the model was trained on nine subsets and evaluated on the remaining one, when this process repeated ten times using different subsets each time.

In addition to cross-validation, model performance was evaluated using common metrics: accuracy, precision, recall, and F1-score. Accuracy measures true predictions among all instances, while precision assesses true positive predictions relative to all instances predicted positive. Recall gauges true positives among all actual positives. F1-score combines precision and recall, offering a balanced performance measure [95]. These metrics were calculated for each class individually and can be combined using averaging techniques including macro (equal weighting), micro (weighted by class instances), and weighted (weighted by class proportions).

In Figure 3-8, the results of 10-fold cross-validation are presented. Figure 3-8(a) illustrates the average F1-score values and standard deviation error bars obtained from 10 iterations of each model across different numbers of SOM clusters. It is observed that RF and XGB exhibit the higher average F1-score values. RF also demonstrates the highest value at cluster numbers 6 and 7, with the least standard deviation.

It is important to note that there is a severe imbalance in the dataset, especially in Class 4 (the highest *Sa* value). Despite employing SMOTE method to address this data shortage in this class, all models struggle to predict Class 4 accurately. However, the overall average value remains acceptable as they perform well in predicting other classes. Therefore, exploring F1-score per class can offer deeper insights into the models' performance. Figure 3-8(b) shows the F1-score per class of different models using 6 SOM clusters. Despite the close average values observed in Figure 3-8(a), significant variations are evident across individual classes. RF and XGB notably excel in predicting Class 4, which is the most challenging class to predict. Therefore, RF not only achieves

the higher average F1-score values but also performs better across each individual classes. This comprehensive analysis suggests that RF is the preferred model for this classification task.

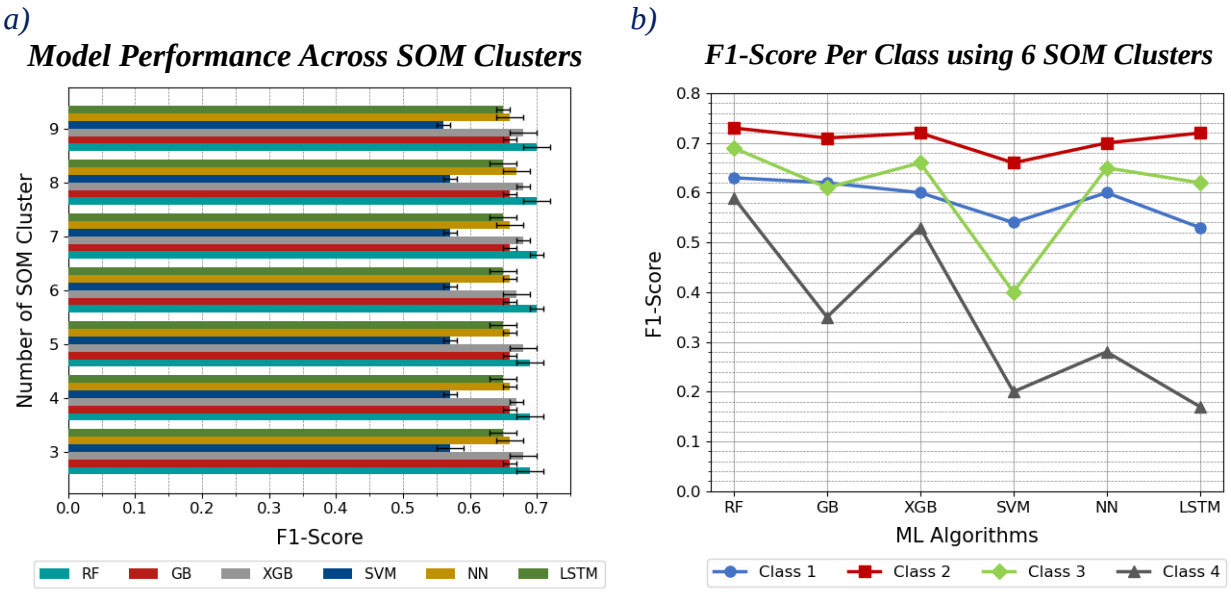


Figure 3-8: Results of 10-fold cross-validation. a) Average F1-score with standard deviation error bars across 10 iterations. b) F1-score comparison per class for each model using 6 SOM clusters.

To determine the optimal number of SOM clusters, the unseen test set was also evaluated. Building upon the previous sections where the superior performance of RF was discussed, the performance of the test set (accuracy, precision, F1-score, and recall) using RF for different numbers of SOM clusters was assessed. Figure 3-9 depicts some of these results, showcasing F1-score per class and macro F1-score in Figure 3-9(a) and recall per class and macro recall in Figure 3-9(b).

The cross-validation results in Figure 3-8(a) revealed that clusters 6 and 7 exhibited the most promising outcomes. However, upon further analysis of the test dataset (see Figure 3-9), it was found that employing 6 clusters led to superior performance. Specifically, this configuration demonstrated higher performance in Class 4 without compromising predictions for other classes, a conclusion supported by the macro-average of both F1-score and recall. Therefore, it can be inferred that utilizing 6 clusters yields the most favorable results for this study.

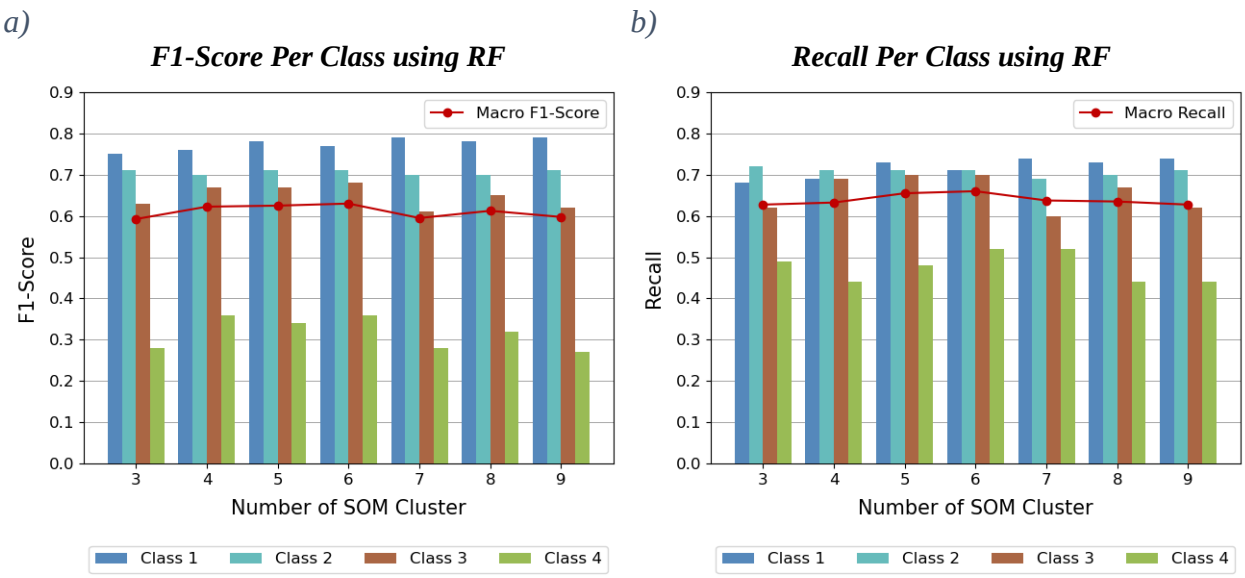


Figure 3-9: Result of unseen test dataset for different number of SOM cluster using RF model. a) F1-score comparison per class and macro F1-score. b) Recall comparison per class and macro recall.

3.3.3. Feature Combination Analysis

In section 3.2.4.1, the four distinct groups of input features were introduced, including the clustered light intensity, process parameters, spatter region index, and edge proximity index (epi). This section investigates the performance of the models with different combinations of input features. Specifically, by removing one of these groups of input features at a time, we aim to observe how the models' performance is impacted. This analysis sheds insights into the relative significance of each group of input features and their contributions to the overall performance of the models.

Figure 3-10 depicts a comparison of four different combinations of input features. In Figure 3-10(a), all four groups were utilized, while Figure 3-10(b) excludes the process parameters, Figure 3-10(c) excludes the spatter region index, and Figure 3-10(d) excludes the edge proximity index (epi). Each plot presents metrics including accuracy, precision, weighted F1-score, and macro F1-score. The inclusion of macro F1-score allows for an overall insight into the model performance, particularly on Class 4. Given the limited number of data points in Class 4, its poor performance might not significantly impact the weighted F1-score. However, the macro F1-score, treating each class equally, can effectively demonstrate the models' overall performance.

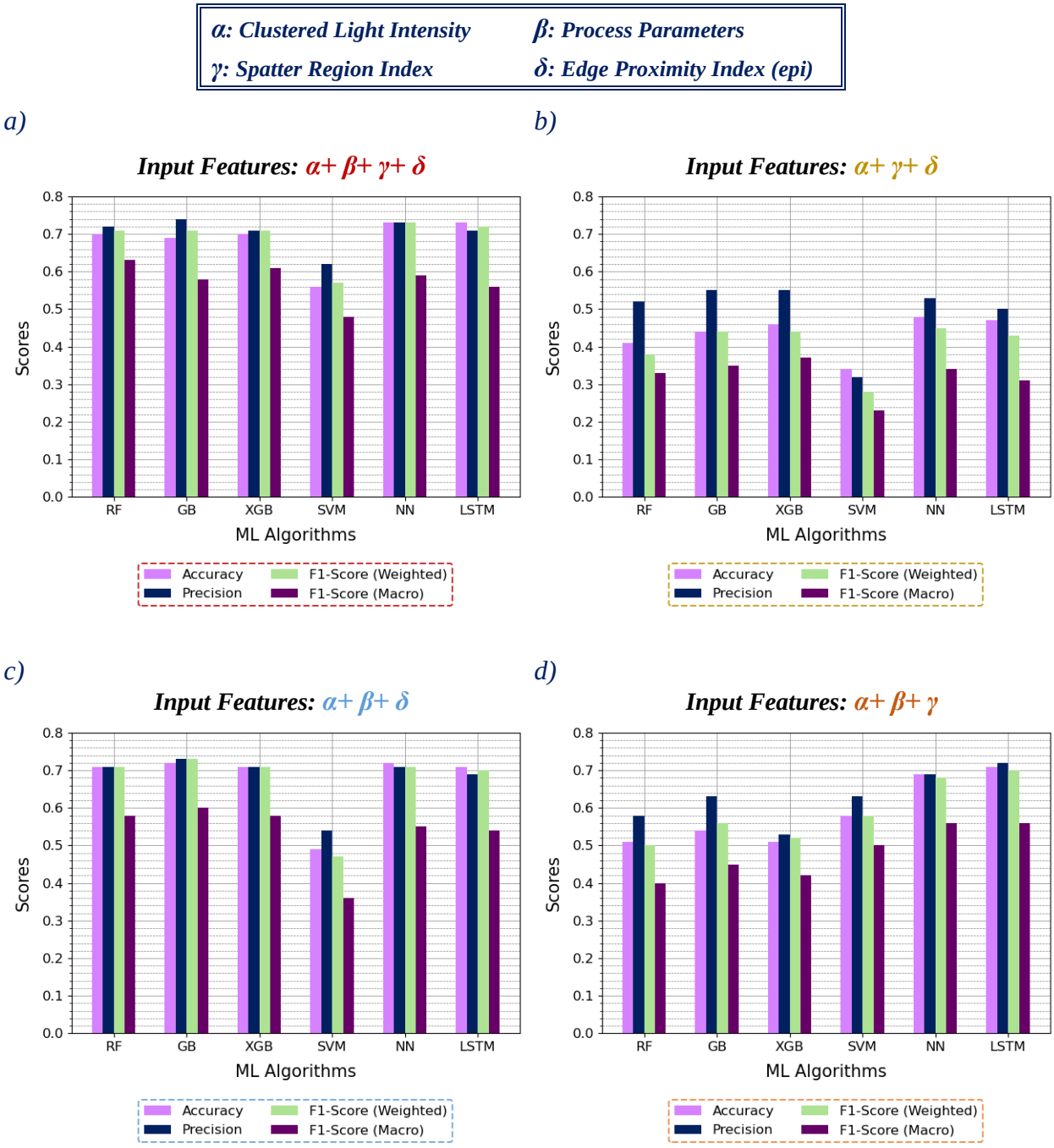


Figure 3-10: Comparison of the models' performance using different combinations of input features on unseen test set. a) All four groups employed. b) Exclusion of the process parameter group. c) Exclusion of the spatter region index group. d) Exclusion of the edge proximity index (epi) group.

In Figure 3-10(a), which utilizes all four feature groups, the metrics demonstrate the highest scores compared to the other graphs. Upon comparing the models' performance within this graph, it becomes evident that while the accuracy, precision, and weighted F1-score of all models, except SVM with a poorer performance, are nearly equivalent, the macro F1-score of RF surpasses others.

This indicates a superior performance of RF, particularly in Class 4. In Figure 3-10(b), where the process parameters group is excluded, it is apparent that the plot exhibits the lowest performance compared to the other graphs in this figure. This observation emphasizes the significant contribution of process parameters in the prediction task. Figure 3-10(c) illustrates the models' performance when excluding the spatter region index. At first glance, it may seem that the exclusion of this feature group does not significantly impact the models' performance, as it appears similar to Figure 3-10(a). However, upon the closer inspection, focusing on the macro F1-score reveals a slight but a noteworthy difference. Without the spatter region index, a lower macro F1-score is observed, indicating decreased performance, particularly in Class 4. This observation suggests that the inclusion of the spatter region index enhances the models' predictive capabilities. This feature group aids in identifying areas of the build plate with higher potential for spatter, typically associated with the higher *Sa* values. Given that Class 4 corresponds to the highest *Sa* values (*Sa* greater than 22 µm), the spatter region index contributes to better predictions for Class 4. Consequently, there is a higher performance in Class 4, resulting in a higher macro F1-score. In Figure 3-10(d), the exclusion of the edge proximity index is observed. Apparently, this exclusion has a significant impact on the performance of RF, XGB, and GB models, albeit a lesser effect on NN and LSTM. This observation suggests that NN and LSTM, being more complex models, can still uncover intricate relationships between input and output, even with the removal of one feature group. However, it is worth noting that NN and LSTM models exhibit a poor performance on Class 4. Considering the data imbalance, ensemble models like RF and XGB tend to outperform neural network models [96]. Therefore, focusing on RF and XGB models, the removal of the edge proximity index significantly impacts the models' performance, indicating its substantial contribution to the accurate prediction of the *Sa* class.

3.3.4. Models Performance Assessment

To delve deeper into comparing the performance of various models, additional metrics, such as Confusion Matrices and Receiver Operating Characteristic (ROC) Curves are widely utilized for evaluating the classification ML problems.

A confusion matrix is a table that presents a clear overview of the performance of a classification algorithm. It consists of the actual class labels on one axis and the predicted class labels on the other axis. The confusion matrix enables visualization of where the model is making errors and which classes it tends to confuse.

In Figure 3-11, the confusion matrix derived from all six models for an unseen test set are presented. One axis represents the four true classes, while the other axis depicts the four predicted classes. The matrix provides the count of data points within each category and their relative frequencies (in percentage), visually depicted via a color bar. Notably, the matrix highlights the significance of the class imbalances. For instance, the differences in the data points among Class 1, Class 2, Class 3, and Class 4, with respective counts of 618, 919, 530, and 61, illustrate the challenge posed by the imbalanced datasets. Consequently, the models struggle particularly with the prediction of Class 4 due to its limited dataset. Upon the closer examination, it becomes evident that RF exhibits superior adaptability in handling data imbalances, yielding acceptable performance, especially concerning Class 4. While NN and LSTM models produce competitive results for Class 1, Class 2, and Class 3, they fail notably when predicting Class 4, indicating their weakness to the dataset imbalances. Following RF, both XGB and GB demonstrate promising performance.

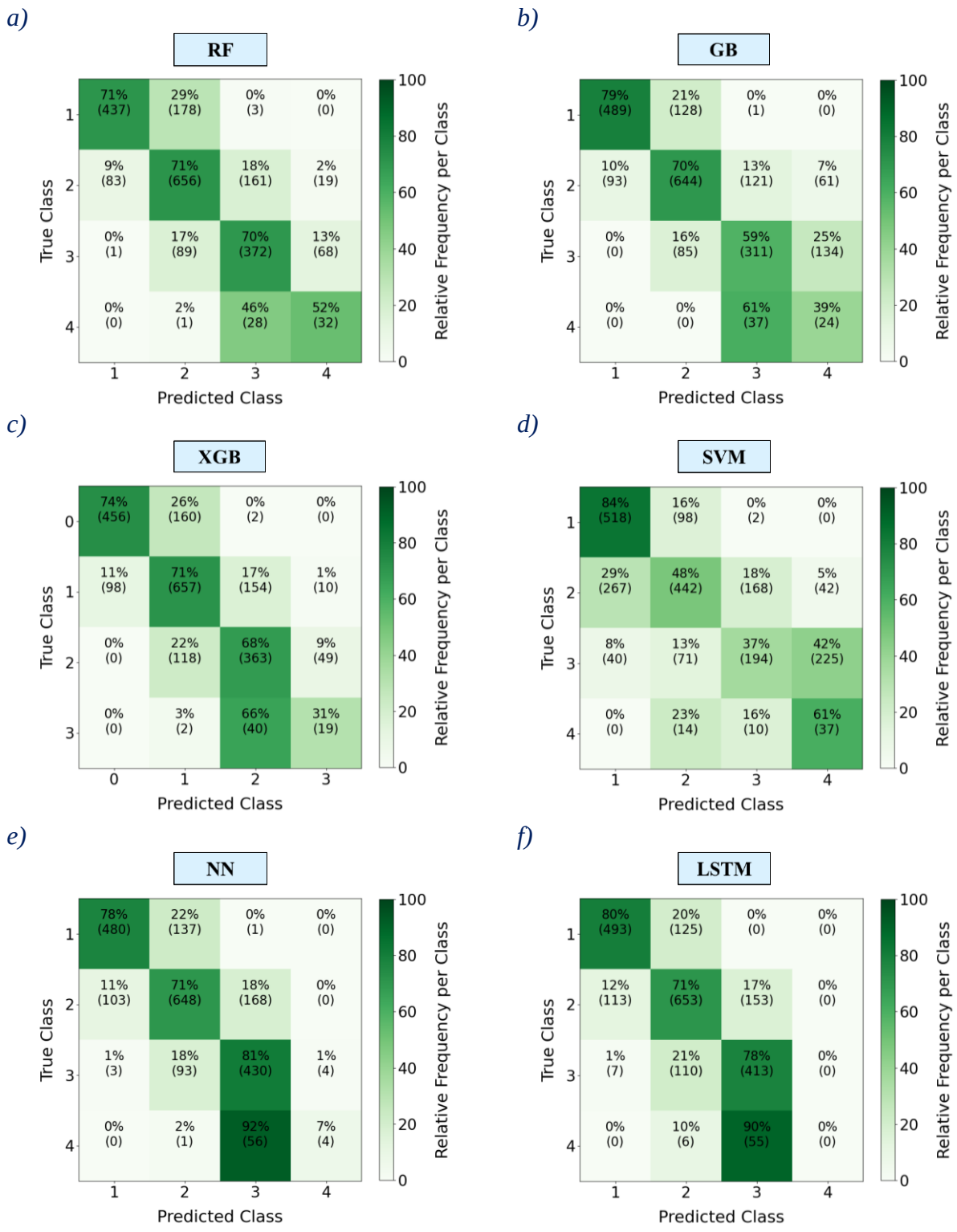


Figure 3-11: Confusion matrix generated by a) RF, b) GB, c) XGB, d) SVM, e) NN, and f) LSTM on unseen test set.

Additionally, ROC curves rely on two crucial metrics: the True Positive Rate (TPR) and the False Positive Rate (FPR). TPR measures the ratio of correctly predicted positive instances to the

total number of positive examples in the dataset, while FPR indicates the proportion of negative instances incorrectly classified as positive. The classifier performance is quantified through the Area Under the ROC Curve (AUC), where a higher AUC denotes a superior classifier. It's noteworthy that any classifier with an AUC exceeding 0.5 outperforms the random chance. Typically, ROC curves are employed for binary classification tasks. However, for the multi-class classification, the output needs to be binarized. This involves treating each class as the positive class once and all other classes as the negative class. Subsequently, separate ROC curves are computed for each class. The micro-average ROC curve aggregates the contributions of all classes by giving equal weight to each prediction, making it suitable for imbalanced class distributions.

Figure 3-12 depicts the ROC curve generated by all models for the unseen test set, comprising five curves: four for individual classes and one for the micro-average. Each plot showcases the AUC value for every class alongside the micro-average curve. Upon analysis of this figure, it becomes apparent that despite encountering challenges associated with the dataset imbalance among the classes and particularly lower accuracy in Class 4, the AUC values indicate excellent performance across all classes. Furthermore, classes 1, 3, and 4 exhibit AUC values around 0.90, demonstrating robust discrimination capability and indicating the model efficacy in distinguishing instances belonging to these classes from others. However, Class 2 exhibits comparatively lower performance, with an AUC ranging from 0.7 to 0.8, which can be attributed to its unique characteristics. Class 2 spans *Sa* values ranging from 8 to 12 µm, exhibiting the highest frequency among all classes. Instances within this class may exhibit greater variability or overlap with instances from neighboring classes, such as those lying marginally below 8 or slightly above 12 microns. This inherent variability poses a considerable challenge for the model in accurately classifying such instances. In total, a thorough comparison of the models reveals that RF, XGB, and GB outperform the others.

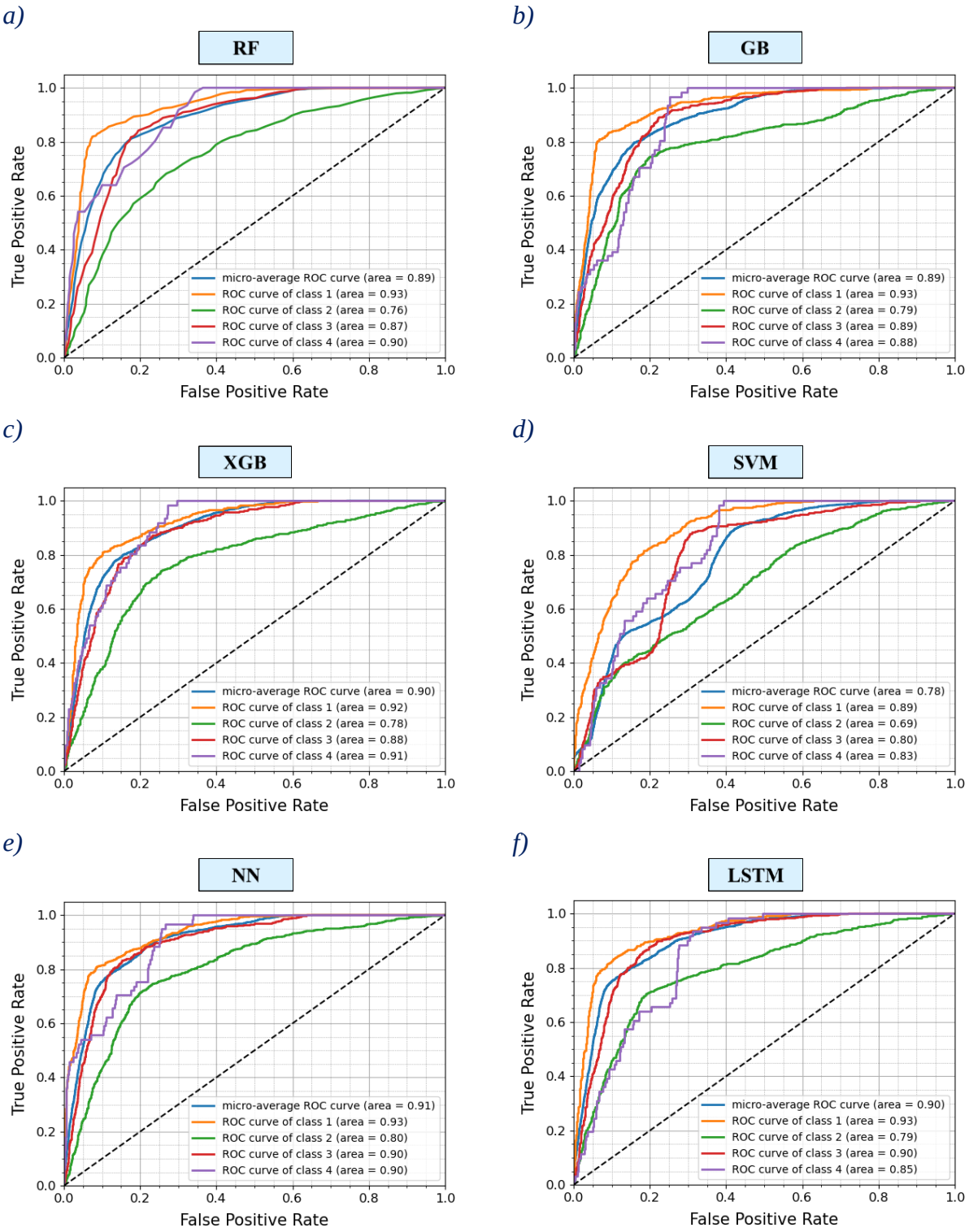


Figure 3-12: Receiver operating characteristic (ROC) curve generated by a) RF, b) GB, c) XGB, d) SVM, e) NN, and f) LSTM on unseen test set.

Table 3-2 presents a comprehensive summary of the performance of all models alongside their respective training times. In the context of the LPBF process, where computational efficiency

directly impacts real-time analysis between layer depositions, models with shorter computational time are favored to prevent process delays. While the training time may not directly affect real-time analysis, as the model is pre-trained and used on new datasets, the runtime serves as a valuable parameter for evaluating the speed of a model in analyzing fresh data. Based on Table 3-2, the RF and XGB models stand out as the fastest, making them promising candidates for integration into LPBF machines. Conversely, LSTM exhibits the longest running time, which may not be optimal for this application. Notably, RF and XGB not only excel in speed but also perform well in evaluation metrics, indicating their potential for superior performance in LPBF processes, where timely and accurate predictions are essential.

Table 3-2: Comparative performance on unseen test set and training times of models

ML Algorithms	F1-Score (Weighted)	F1-Score (Macro)	Accuracy	AUC (Micro)	Training time
RF	0.71	0.63	0.70	0.89	3 s
GB	0.71	0.58	0.69	0.89	12 s
XGB	0.71	0.61	0.70	0.9	3 s
SVM	0.57	0.48	0.56	0.78	45 s
NN	0.73	0.59	0.73	0.91	1 min 14 s
LSTM	0.72	0.56	0.73	0.90	4 min 50 s

3.3.5. Training Set Size Exploration

In this section, we explore the impact of varying train set sizes on model performance. As previously mentioned, we maintained 8 parts (2,128 cells) as an unseen test set, while designating 34 parts (9,044 cells) as the original train set. To examine the effect of reducing the train set size while keeping the test set constant, we considered train set proportions of 80% (~27 parts), 60% (~20 parts), 40% (~14 parts), and 20% (~7 parts). The selection of parts for each batch of the train set was based on covering the range of VED from low to high. Figure 3-13 (a) and Figure 3-13 (b) illustrate the weighted F1-score and macro F1-score values on unseen test set respectively for all models across different train set sizes. It is evident that the weighted F1-score remains favorable for models trained with 27 and 20 parts, outperforming the RF model. However, the macro F1-score decreases, indicating less effective performance for Class 4. Furthermore, as the train set size decreases further to 14 and 7 parts, a noticeable drop in performance is observed, albeit this drop is less pronounced for XGB and GB models compared to others.

It is worth noting that while RF appears to be the better option with sufficient data points, when data points are limited, XGB and GB might offer better performance. This underscores the

importance of considering both the volume and quality of data when selecting the appropriate model for a given scenario.

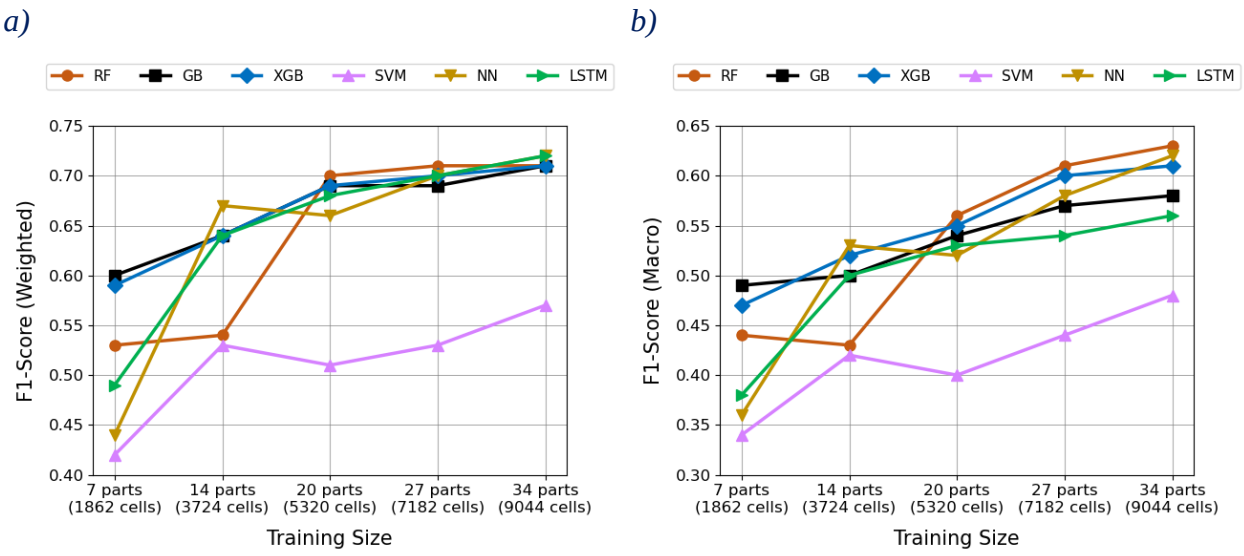


Figure 3-13: Effect of the train set size on the models' performance on unseen test set. a) Weighted F1-score. b) Macro F1-score.

3.3.6. Random Forest Feature Importance

Based on the prior discussion, the RF model has demonstrated a remarkable capability in handling data imbalances, outperforming other applied models. This section delves deeper into the model by analyzing its feature importance.

Feature importance refers to the relative significance of each feature in making relatively accurate predictions. These scores can provide valuable insights into the predictive power of each feature, and highlight which features are most relevant and influential in making predictions. These findings can guide further data exploration and feature selection. For instance, features with high importance scores can be used for developing simpler models, while those with low importance scores can be omitted to reduce the complexity of the model.

In Figure 3-14, we observe the feature importance generated by RF across various combinations of input features, each denoted by distinct color codes representing four different groups of input features (refer to Figure 3-5). In Figure 3-14(a), where all four groups are considered, the "VED" feature from the "process parameters" group exhibits the highest score, indicating its significant impact on prediction accuracy. Additionally, features such as "clustered light intensity" (labeled as C1 to C6) and "edge proximity index (epi)" also display notable importance scores, contributing

significantly to the model accuracy. Conversely, features like "power," "scanning speed," and "hatch distance" from the "process parameters" group show relatively lower importance scores, suggesting minimal impact on predictions. In should be however noted that VED has a relationship with laser power, scanning speed and hatching distance. This suggests that integrating these factors into a unified number (VED), could enhance correlation with the ML model. VED usually offers better consistency in deviation, potentially optimizing the weights in the RF structure, enhancing predictive capabilities and operational efficiency. Figure 3-14(b) illustrates the scenario where the "process parameters" group is excluded. Here, all three remaining groups exhibit almost equal contributions to prediction accuracy, even including "spatter region index," which showed lower scores in Figure 3-14(a). This implies that in the absence of "process parameters," the model relies more on other features to enhance prediction accuracy. Moving to Figure 3-14(c), where "spatter region index" is excluded, the feature importance plot closely resembles Figure 3-14(a) with all four groups considered. However, in Figure 3-14(d), the exclusion of "epi" induces a notable shift; as "VED" is no longer the most important feature; instead, "clustered light intensity" takes precedence. This shift can be attributed to the removal of "epi," which distinguishes edges potentially having higher surface roughness from centers, prompting the model to rely more on in-situ light intensity data for classifying different surface roughness values.

Overall, it is evident that while process parameters were expected to influence surface roughness, external factors also play a significant role. Variables such as spatters, re-coater and argon gas flow direction introduce variability in surface roughness across different locations. Therefore, accurate prediction and control of surface roughness necessitate in-situ monitoring and consideration of each area specific characteristics.

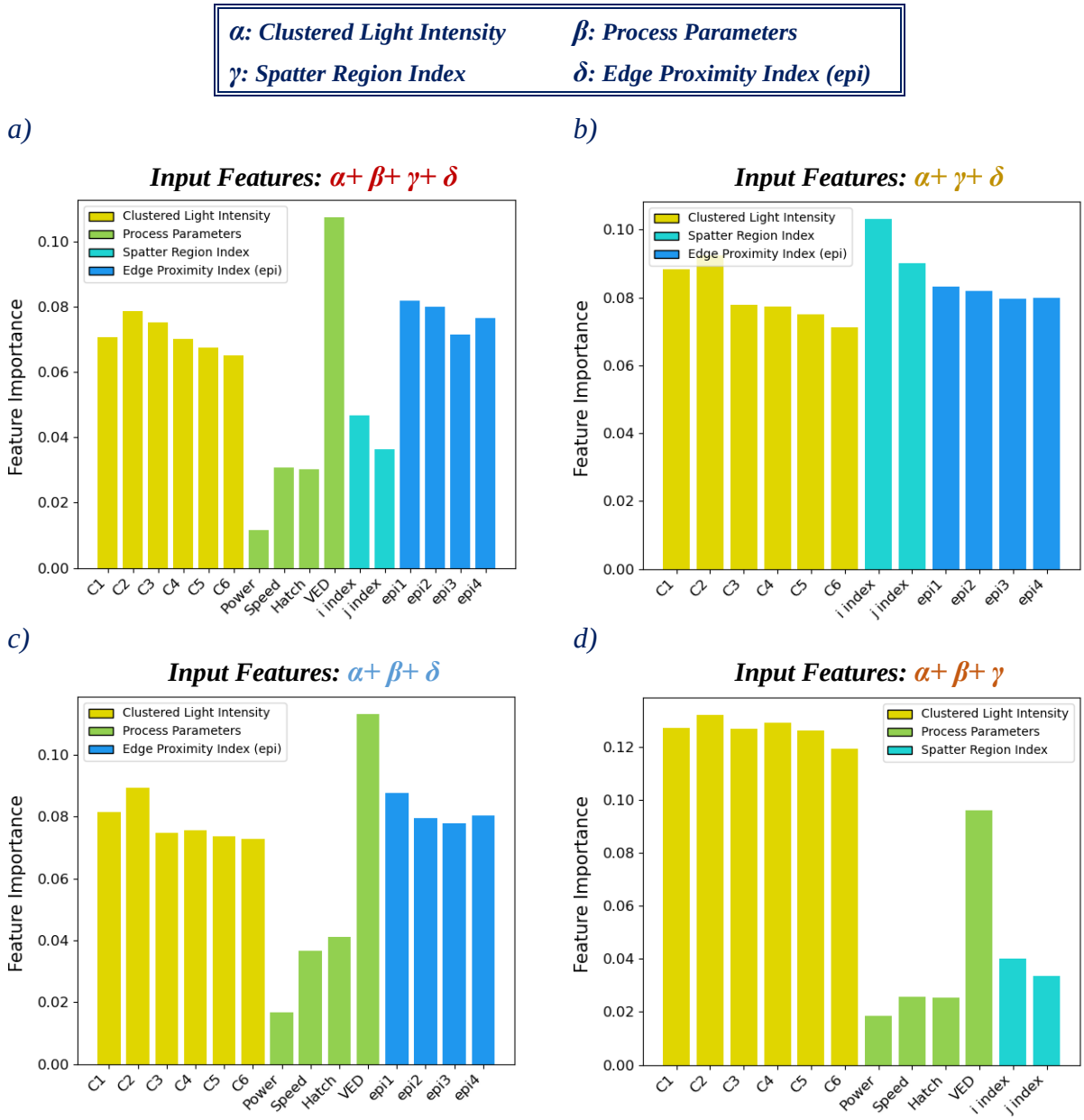


Figure 3-14: Comparative assessment of random forest feature importance across different input feature combinations, distinguished by color to represent four distinct input feature groups. a) All four groups employed. b) Exclusion of the process parameter group. c) Exclusion of the spatter region index group. d) Exclusion of the edge proximity index (epi) group. (Note: C1-C6 denote clustered light intensity)

3.4. Summery

This study investigated the relationship between top surface roughness and the light intensity signal emitted from the melt pool, captured by an in-situ photodiode from the last three layers of the build. The collected intensity data were clustered using SOM algorithm and combined with key process parameters to serve as input for various ML models. These models were trained to predict surface roughness at a fine resolution (690 µm × 510 µm) for each small area, including edges and

corners across each layer. The performance of the models was rigorously evaluated using an unseen test dataset, ensuring their reliability and generalization capability.

Chapter 4. A Pioneer Machine Learning-Driven Platform for In-Situ Vertical Side Surface Roughness Prediction in Laser Powder Bed Fusion

4.1. Abstract

Real-time surface roughness prediction in laser powder bed fusion (LPBF) is crucial for achieving effective control and enhancing part quality. Surface roughness directly impacts fatigue life and contributes to increased post-processing costs. While in-situ monitoring has become a paradigm for real-time defect detection in LPBF, surface roughness prediction, particularly for vertical surfaces of printed components with respect to the build plate, remains entirely unexplored. Existing studies primarily address in-situ detection of the top surface roughness of printed parts, while vertical surface assessments relying on ex-situ methods that lack real-time capabilities. This limitation is attributed to the coverage of vertical walls with loose powder particles within the powder bed, obstructing the visibility/sensing of the site of interest. This study pioneers a framework for in-situ prediction of vertical surface roughness using a photodiode sensor integrated with machine learning (ML) detection algorithms. The photodiode sensor enables fast response times, capturing light intensity signals from regions adjacent to vertical surfaces during the printing process. Key time-domain and frequency-domain features are extracted from the photodiode signals and combined with essential process parameters to predict the surface roughness of each vertical side. The performance of five ML models was evaluated across multiple configurations of input features. Random Forst (RF) and eXtreme Gradient Boosting (XGB) emerged as the most robust models, achieving high accuracy and low error rates. Incorporating in-situ data significantly enhanced model performance, improving RF's R^2 from 0.35 (using process parameters alone) to 0.78, demonstrating the effectiveness of this approach. This work establishes a novel pathway for real-time vertical surface roughness prediction and provides a foundation for improved quality control and optimization in additive manufacturing processes.

4.2. Methods and Data Preparation

4.2.1. Experimental Design Strategy

In this study, parts were fabricated from Ti-6Al-4V powder using a LPBF process. Manufacturing was performed on an EOS M290 LPBF machine, utilizing a fixed layer thickness, a rotated stripe scanning strategy, and a zero-width stripe, without contour scanning, skin, or post-exposure. A systematic variation of process parameters, including laser power, scanning speed, and hatch distance, was employed to achieve a wide range of surface roughness characteristics. These parameters were refined based on a Volume Energy Density (VED) ranging from 25 to 50 J/mm³, calculated as the ratio of laser power to the product of process speed, hatching distance, and layer thickness. This range was selected to ensure the integrity of the fabricated parts while minimizing common defects such as lack of fusion, overheating, and cracking [97], [98]. This refinement resulted in 21 unique parameter combinations. To ensure statistical reliability and account for external factors such as part location on the build plate and the influence of spatter, each process configuration was replicated, resulting in a total of 42 samples. A summary of the selected process parameters and their corresponding VED values is presented in Table 4-1, while Figure 4-1 illustrates the location of each part on the build plate along with its duplicate.

Table 4-1. Process parameters and corresponding VED values, calculated using $VED = \frac{P}{V.h.t}$ *(layer thickness t = 0.04 mm)*

Part Name	Power (P) [W]	Scanning Speed (V) [mm/s]	Hatch Distance (h) [mm]	VED [J/mm3]
P1	125	1000	0.08	39.06
P2	125	1000	0.10	31.25
P3	125	1250	0.06	41.67
P4	125	1250	0.08	31.25
P5	125	1250	0.10	25.00
P6	125	1500	0.06	34.72
P7	125	1500	0.08	26.04
P8	150	1000	0.08	46.88
P9	150	1000	0.10	37.50
P10	150	1250	0.06	50.00
P11	150	1250	0.08	37.50

P12	150	1250	0.10	30.00
P13	150	1500	0.06	41.67
P14	150	1500	0.08	31.25
P15	150	1500	0.10	25.00
P16	175	1000	0.10	43.75
P17	175	1250	0.08	43.75
P18	175	1250	0.10	35.00
P19	175	1500	0.06	48.61
P20	175	1500	0.08	36.46
P21	175	1500	0.10	29.17

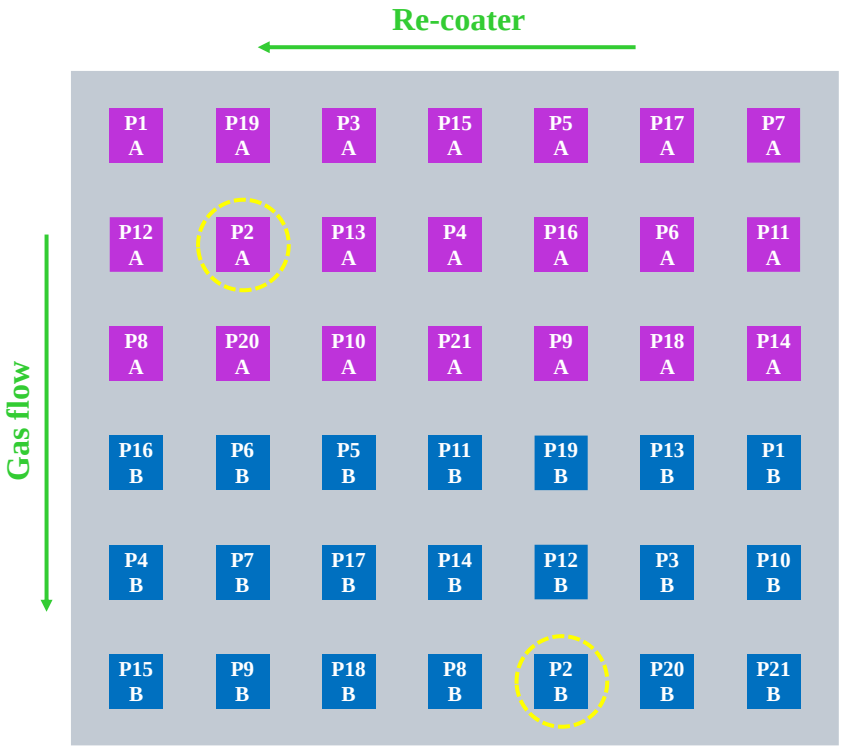


Figure 4-1. Layout of part locations on the build plate for replicates A and B. As an example, part 2 (replicates A and B) is highlighted.

To further enhance dataset robustness and ensure consistency in sample fabrication, the build plate was reproduced under the same process conditions, yielding an additional 42 parts (Build Plate 2). This duplication minimized variability and provided a comprehensive dataset of 84 parts for subsequent analysis.

It is worth noting that this study complements our prior work by shifting the focus from top surface roughness to vertical (side) surface roughness, further expanding the understanding of surface characteristics in LPBF-processed parts. For a more detailed description of the experimental design and methodology, refer to our previous study [5].

4.2.2. Data Acquisition and Measurements

After designing the experiment, a two-step process was employed to collect data for subsequent use in ML models as inputs and outputs. The first step involved real-time collection of light intensity data during the printing process using a photodiode sensor. Measurements were taken from all four vertical sides of each part (Front, Left, Back, and Right). After preprocessing this data, it was utilized as the input for the ML model.

The second step, conducted post-printing, involved measuring the surface roughness of all four sides of each part. These measurements were considered as the output of the ML model. Further details on these two steps are provided in the following sections.

4.2.2.1. In-Situ Monitoring of Light Intensity (Photodiode Sensor Measurements from Vertical Sides—Front, Left, Back, and Right)

This study employed a commercial on-axis photodiode integrated into the EOS M290 system to record light intensity signals in real time. The photodiode operates at a sampling rate of 60 kHz, capturing light intensity within a wavelength range of 750–900 nm [65]. During the printing process, light intensity data are collected from the melt pool for each layer, a process referred to as Melt Pool Monitoring (MPM). These data include the recorded light intensity values alongside the corresponding x- and y-coordinates. Figure 4-2 schematically illustrates the light intensity collected for several layers, showing how datapoints are distributed across the x-y plane of the melt pool. Each layer contains approximately 36,000 data points.

In our previous study, which focused on top surface roughness, the light intensity data from the last three layers (spanning the entire layer area) were considered. However, this study shifts focus to side surfaces, where light intensity data are collected from specific depths near the edges of some sequential layers. This parameter is defined as the "Edge Margin Zone" (EMZ) and introduced to capture relevant edge data for side surface roughness analysis.

Figure 4-2 focuses on the Front Side as an example. To predict the surface roughness of the Front Side, the light intensity data from layers within a specific EMZ relative to the "front edge"

of each layer are collected. The same process is repeated for the other three sides (Left, Back, and Right), with the respective EMZ values applied near their corresponding edges.

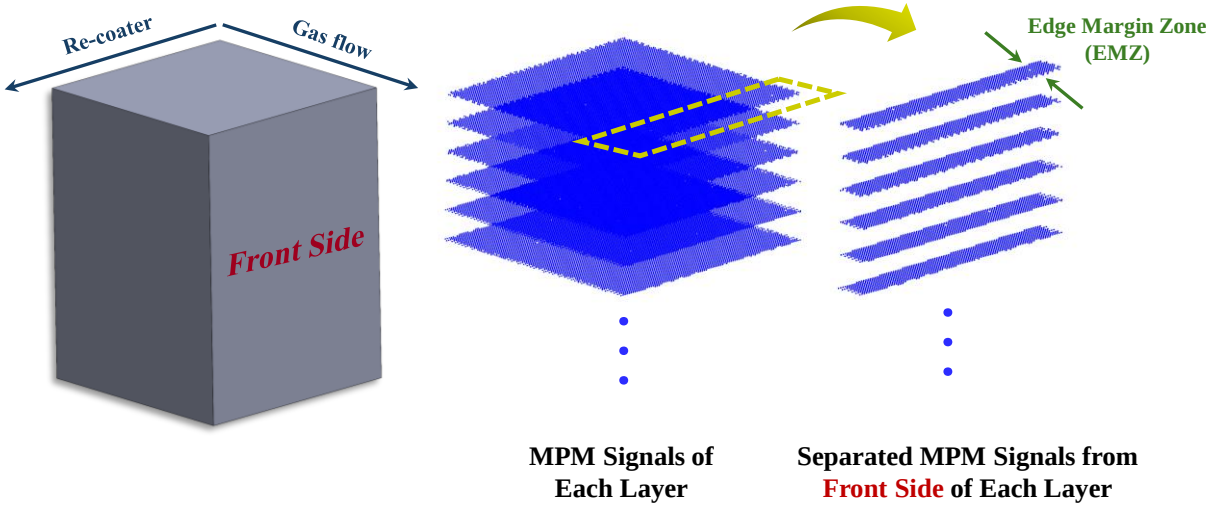


Figure 4-2. Schematic of light intensity data collection during Melt Pool Monitoring (MPM), showing datapoints recorded across the x-y plane and the concept of the Edge Margin Zone (EMZ) for the Front Side.

The number of sequential layers depends on the area of interest. For instance, this study focuses on the top 5 mm of the parts (equivalent to the last 125 layers). Thus, the light intensity data for the top 5 mm of each side surface are used. If another area, such as the lower section, needs to be analyzed, the corresponding layers for that area can be considered.

A critical question concerns the optimal EMZ length. To address this, 10 different EMZ dimensions were investigated: 40, 80, 120, 160, 200, 240, 280, 320, 360, and 400 μm. These values correspond to 1 to 10 times the layer thickness (40 μm).

Figure 4-3 illustrates the EMZ concept and its relationship with data collection. The schematic depicts three EMZ values (120, 280, and 400 μm), represented by progressively thicker zones near the edges of the layers. As the EMZ increases, the data density also increases, reflecting a larger number of datapoints being stacked together. Different sides (Front, Left, Back, and Right) are color-coded—red, blue, cyan, and green, respectively— to represent the data collected from each side. The schematic specifically highlights the top 5 mm of the parts for clarity.

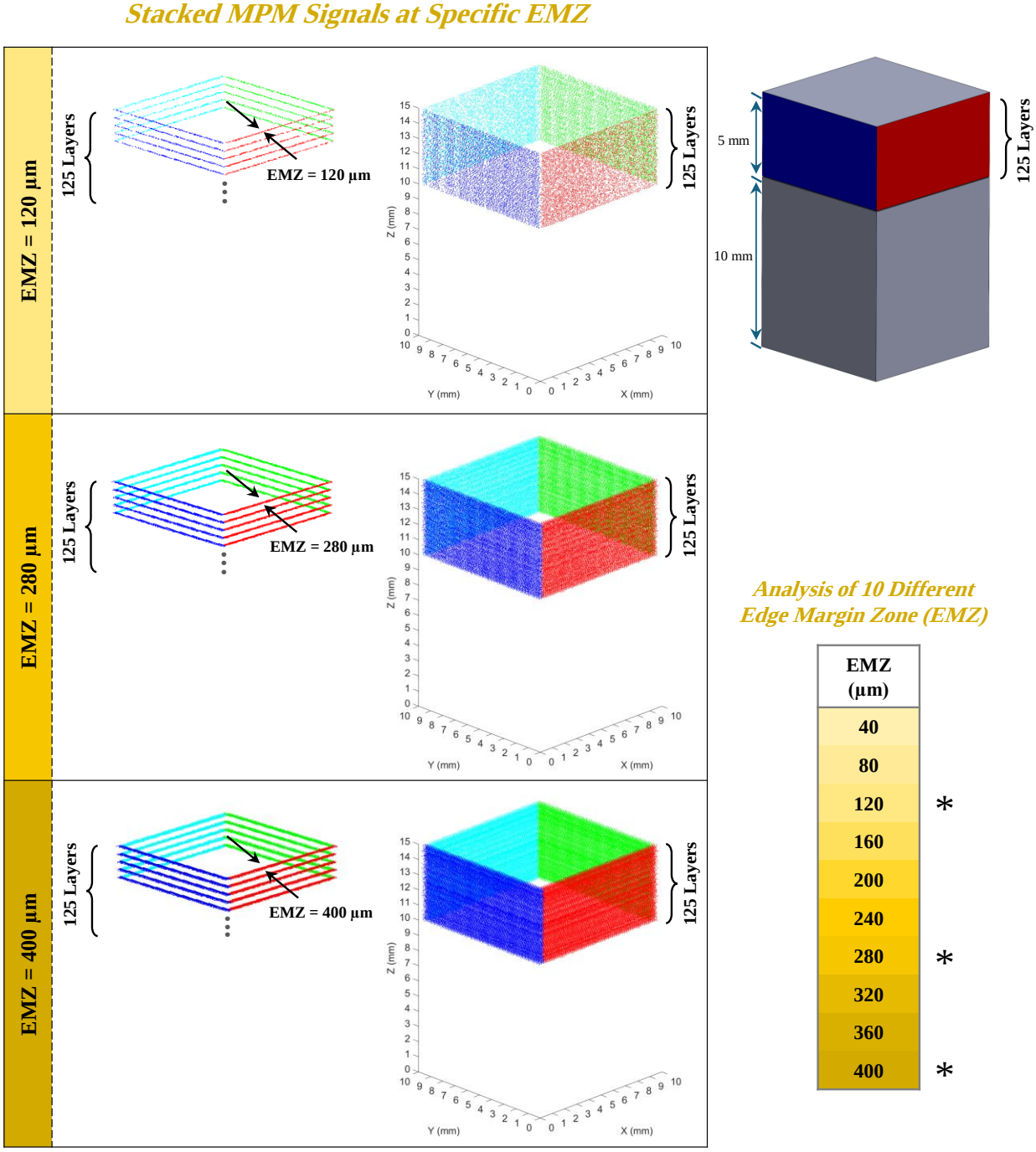


Figure 4-3. Illustration of the Edge Margin Zone (EMZ) concept with three values (120, 280, and 400 µm) marked with (*). Color coding (red for Front, blue for Left, cyan for Back, and green for Right) represents the data collected from each side, highlighting the top 5 mm of the part.

After stacking, the data for each side are converted into a one-dimensional (1D) signal (i.e., data array) through a process known as "flattening," as shown in Figure 4-4. This process organizes the datapoints sequentially from the bottom to the top layer of the area of interest. The schematic in

Figure 4-4 demonstrates how the 2D layered data transform into a continuous 1D signal, highlighting both the structure and inherent noise in the data. The example focuses on the Front Side, but the same procedure is applied to the other three sides.

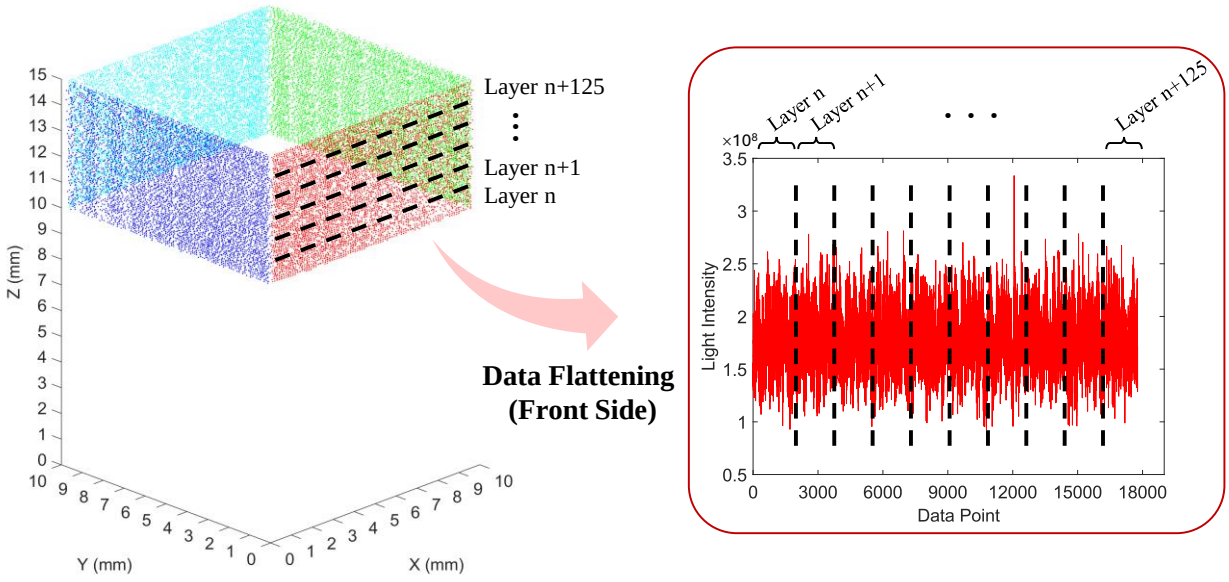


Figure 4-4. Flattening process to convert 2D layered data into a continuous 1D signal, shown for the Front Side as a representative example and sequentially ordered from the bottom to the top of the area of interest.

The resulting 1D signal contains noise, making it unsuitable for direct use in the ML models. To address this, feature extraction methods are employed to derive meaningful characteristics from the signal. Figure 4-5 outlines this process, where the 1D signal for each side undergoes feature extraction to compute both time-domain and frequency-domain features. These extracted features serve as the inputs for the ML model. For instance, time-domain features may include statistical measures such as mean, variance, and skewness, while frequency-domain features may involve dominant frequencies or amplitude. Details of these feature extraction methods are elaborated in Section 4.2.3.

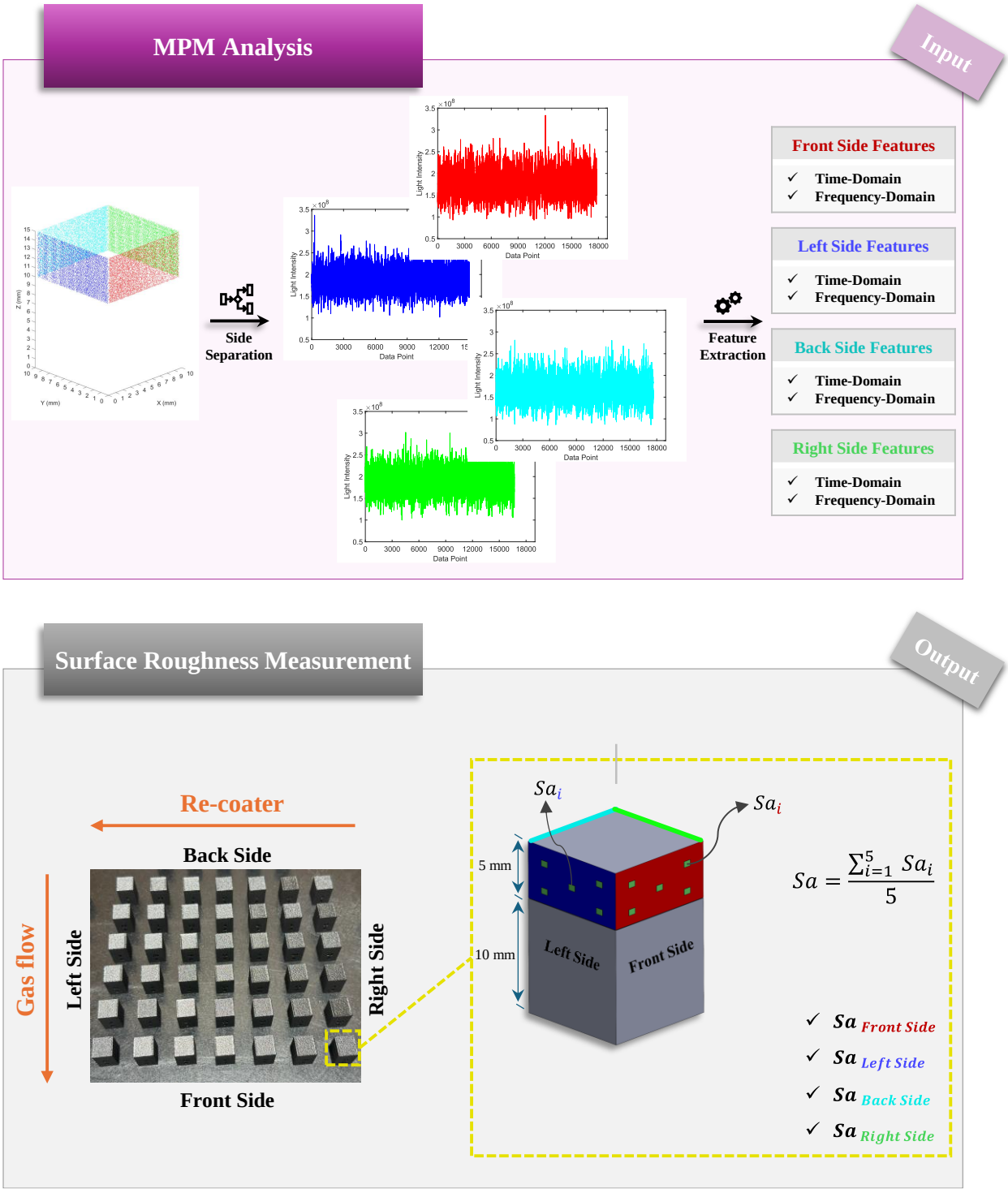


Figure 4-5. Illustration of the feature extraction process (input) and surface roughness measurement (output) for the top 5 mm of the part. Input: Time-domain and frequency-domain features extracted from the 1D signal of each vertical side. Output: Representative Sa values averaged from five discrete points per side, serving as ML model outputs.

4.2.2.2. Surface Roughness Measurements (Sa values collected from vertical sides—Front, Left, Back, and Right)

The second stage of data acquisition focused on measuring surface roughness from the vertical sides of the parts. These measurements were performed using a Keyence Laser Scanning Confocal Microscope (LSCM) with a 20× objective lens. LSCM is a non-contact, non-destructive technique capable of measuring roughness, height profiles, and film thickness with nanometer-level resolution on various shapes and materials. Unlike conventional widefield microscopy, LSCM provides enhanced depth-of-field control, supports serial optical sectioning of thick specimens, and generates high-resolution 3D structural images [67], [69]. Among various surface texture parameters [71], such as *Sq* (root mean square height, measuring overall surface deviations), *Sa* (arithmetical mean height, representing the average height of the surface), *Sz* (maximum height of the surface, representing peak-to-valley distance), and *Ssk* (skewness, describing surface asymmetry), *Sa* was selected as the surface roughness parameter for this study. *Sa* provides a straightforward, robust measure of the average height variations over a given area, making it well-suited for capturing general surface characteristics and ensuring comparability across studies. *Sa* was calculated using following equation**:**

$$Sa = \frac{1}{A}\iint_{A} |Z(x,y)|dxdy \qquad \textit{Equation 4-1}$$

where A is the evaluation area (the region over which roughness is assessed), and *Z(x,y)* is the deviation of the surface height from the mean plane at a given position *(x,y)*.

As the area of interest was the top 5 mm of the parts, measurements were performed on this region for all four vertical sides (Front, Left, Back, and Right). To ensure a representative and reliable estimation of the surface's overall roughness, five discrete points were selected on each vertical side (see Figure 4-5). The *Sa* value was calculated for each point, and the average of these five points was used as the representative *Sa* value for each side. These representative *Sa* values serve as the output variables for the ML models.

4.2.3. Feature Engineering Techniques

Based on the data collected for the vertical sides using the photodiode sensor, and then converting it into a 1D signal, significant and meaningful features must be extracted to serve as inputs for the ML model. Directly using the entire signal, particularly in the presence of noise, can result in

inefficiencies and reduced model accuracy. Feature extraction (known as data mining) plays a crucial role in isolating relevant information from the signal, thereby enhancing the model's predictive performance. For one-dimensional signals, such as time series or sensor outputs, features can be extracted from both the time and frequency domains, each offering unique insights and implications.

Time-Domain Features

Time-domain analysis examines the signal's behavior over time, capturing trends, peaks, and statistical properties. Key features include Mean, Variance, Standard Deviation, Maximum, Minimum, Root Mean Square, Skewness, Kurtosis, and Autocorrelation [99], [100]. Additionally, clustering techniques like Self-Organizing Maps (SOMs) help identify patterns and anomalies by grouping similar signals.

Frequency-Domain Features

Frequency-domain analysis, often using the Fourier Transform (FT), reveals periodic components and energy distribution across frequencies. Key features include Power Spectral Density (PSD), Dominant Frequency, Spectral Centroid, Bandwidth, Spectral Flatness, Harmonic Ratios, and Amplitude [101].

By integrating features from both domains, a comprehensive signal analysis is achieved, leading to improved modeling. This study evaluated various feature combinations for predictive accuracy using coefficient of determination (R^2) and Root Mean Squared Error (RMSE) metrics. Cross-validation ensured robustness, with models tested on unseen data. The most relevant feature set identified:

- ✓ **Time-Domain Features**: Clustering (using SOMs), Variance, Standard Deviation, Skewness, Kurtosis, and Autocorrelation.
- ✓ **Frequency-Domain Features**: Dominant Frequency and Amplitude.

This approach demonstrated the importance of integrating features from both domains to achieve accurate and insightful signal analysis, ultimately enhancing predictive performance in manufacturing applications.

4.2.4. Development of the Machine Learning Model

Following the extraction of features, the inputs and outputs required for the ML model were defined, enabling the development of its structure. This section presents the framework of the ML

model, provides brief definitions of the implemented models, and elaborates on the data splitting and training workflow in detail.

4.2.4.1. Machine Learning Framework

As described in the Introduction section, one of the quality assurance techniques in AM is ex-situ monitoring, where real-time information during the process is unavailable. In the context of surface roughness prediction, this approach typically involves developing a ML model that uses key process parameters as inputs and surface roughness as the output. This model can subsequently be employed to predict surface roughness based solely on process parameters. While process parameters such as laser power, hatch distance, scanning speed, and VED significantly influence surface roughness, external factors also play a critical role. Variables such as spatter deposition, re-coater movement, and argon gas flow direction introduce additional variability, causing fluctuations in surface roughness across different regions. Furthermore, relying solely on process parameters results in the same predicted surface roughness for all vertical sides; however, the actual surface roughness of different vertical sides often varies due to these external factors. Consequently, this conventional approach, based only on process parameters, may lack reliability and accuracy.

To address these limitations, incorporating the discussed real-time process information offers a more robust solution. In this study, as illustrated in Figure 4-6, an in-situ surface roughness prediction model for vertical sides is proposed. The features extracted from light intensity signals, obtained through MPM, were combined with key process parameters to enhance the robustness and accuracy of the model. Unlike the conventional method, which utilizes only process parameters, the proposed approach integrates extracted features from both the time-domain and frequency-domain of in-situ light intensity signals.

The key process parameters used in this study include power, hatch distance, scanning speed, and VED. By incorporating in-situ features, the model accounts for additional process variations, leading to improved predictive performance. The impact of this enhancement on the model accuracy and reliability will be discussed in detail in the section 4.3 (Results and Discussion). One of the significant advantages of in-situ prediction is the potential for adaptive process control. By predicting vertical surface roughness in real time for the region of interest, any deviation from the desired range can prompt adjustments to process parameters for subsequent layers. This iterative

adjustment enables monitoring of progress and refinement of surface quality during the manufacturing process.

To implement the predictive modeling approach, five ML models were selected: eXtreme Gradient Boosting (XGB) [102], Random Forest (RF) [103], Support Vector Regression (SVR) [104], Gaussian Process Regression (GPR) [105], and Feedforward Neural Network (FNN) [106]. These models were chosen for their diverse strengths, allowing for a comprehensive comparison of predictive performance and robustness in handling both process parameters and in-situ features.

XGB, a gradient-boosting algorithm, is well-suited for capturing complex patterns and offers high predictive accuracy with built-in regularization to reduce overfitting. However, it requires careful hyperparameter tuning and can be computationally intensive. RF, an ensemble-based method, is effective for high-dimensional data and robust to overfitting, but it is less suitable for extrapolation and can be computationally expensive with large datasets. SVR excels at modeling non-linear relationships, especially with small datasets, but it requires feature scaling and may struggle with larger datasets due to increased computational demands. GPR, a probabilistic model, provides both predictions and uncertainty estimates, making it valuable for cases where confidence intervals are needed, but its scalability is limited due to its cubic computational complexity with larger datasets. Finally, FNNs offer high flexibility for modeling intricate, non-linear relationships, but they demand significant computational resources and large datasets to perform effectively without overfitting [93], [107]. By employing these diverse models, this study ensures a robust evaluation of predictive performance, enabling the identification of the most effective approach for surface roughness prediction under varying conditions.

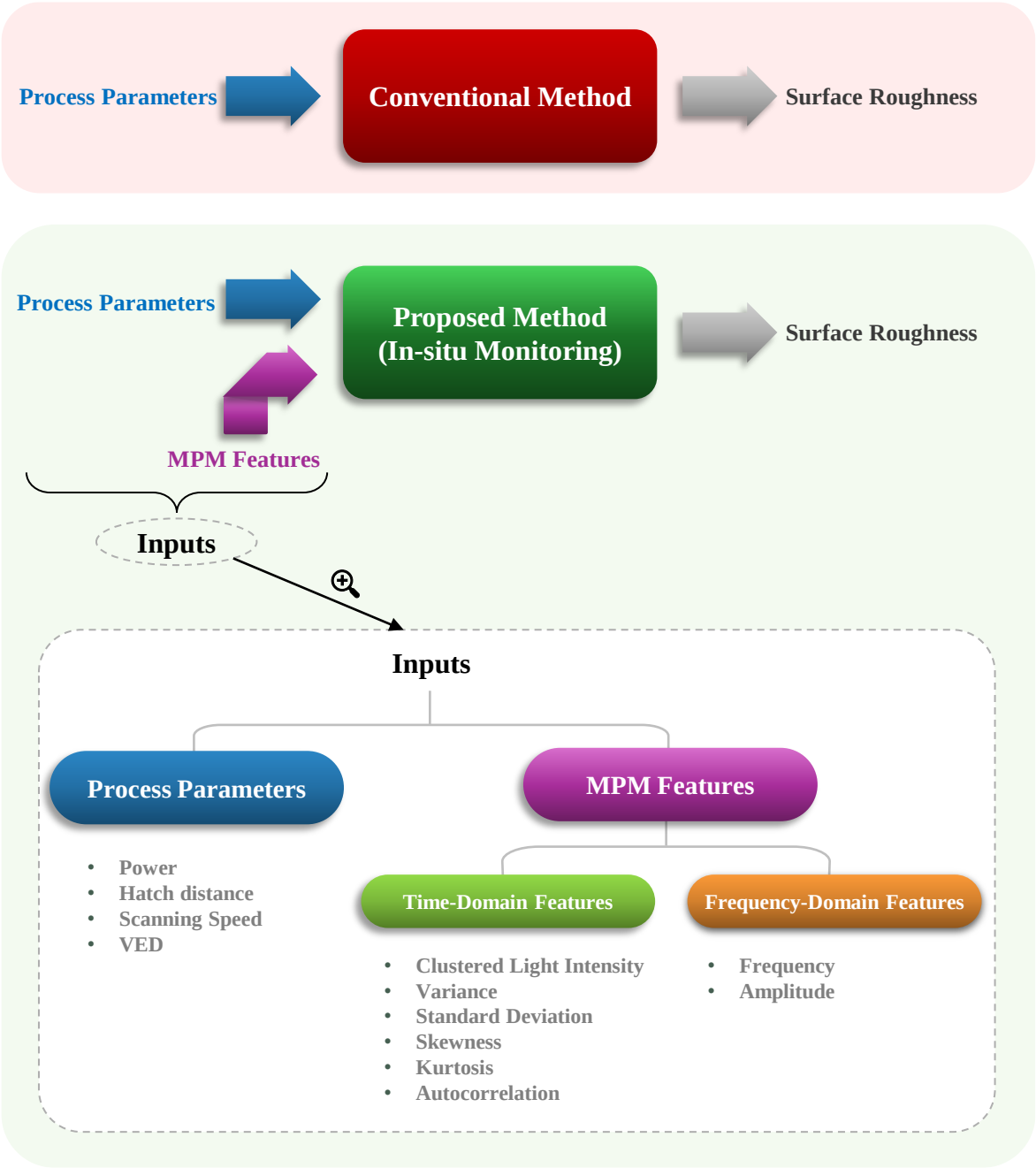


Figure 4-6. Conventional vs. proposed methods for surface roughness prediction: process parameters only vs. process parameters with in-situ features, including time-domain and frequency-domain features extracted from light intensity signals (MPM).

4.2.4.2. Dataset splitting and Preprocessing

To develop an ML model, it is crucial to train the model on a subset of data and evaluate its performance on an unseen subset. This approach ensures the reliability and generalizability of the model. The dataset used in this study consisted of 336 data points, derived from 84 parts, with 42 parts in each of two build plates, and four distinct vertical sides for each part.

To split the dataset, 80% of the data (268 data points) was allocated to the training set, and the remaining 20% (68 data points) was reserved for the testing set. While the splitting was performed randomly, it was verified to ensure that the distribution of data points from each vertical side in the test set was closely proportional to that in the training set. This approach ensures a more reliable and realistic representation of the data, preserving the balance across different categories.

Given the observed variations in scale within the dataset, standardization was applied to ensure consistent feature scaling. Standardization adjusts features so that they have a mean of 0 and a standard deviation of 1, as defined by the formula:

$$X_{standardized} = \frac{X - \mu}{\sigma} \qquad \textit{Equation 4-2}$$

where μ is the mean and σ is the standard deviation of the data. This preprocessing step was critical for achieving optimal model performance by ensuring that all features contributed equally during training.

4.2.4.3. Model Training Workflow and Hyperparameter Optimization

The overall model training and hyperparameter optimization process is illustrated in Figure 4-7. It outlines the step-by-step workflow, starting from data loading and feature engineering to the final evaluation of model performance. Table 4-2 lists the selected hyperparameters, along with their brief definitions and the ranges explored for each model. During the optimization process, measures were taken to mitigate overfitting by avoiding excessively complex model configurations. The table also highlights the final chosen value for each hyperparameter.

To achieve these final hyperparameter values, the following systematic optimization process was followed: Initially, the train and test datasets were loaded, and feature engineering was performed to extract relevant features from both the time and frequency domains. Random search was first employed with 100 iterations, where hyperparameter values were randomly selected within predefined ranges, and the best configuration was identified based on the highest R^2 value using cross-validation (CV). A threshold R^2 value of 0.7 was set, as achieving 70% accuracy in predicting surface roughness in LPBF processes is considered reasonable given the complexity of the process and influencing factors [5], [108], [109]. If the R^2 was below this threshold, the feature engineering process was revisited to remove the irrelevant features and add potentially significant missed features. Once the R^2 exceeded the threshold, additional fine-tuning was performed by

adjusting the range of hyperparameters in the “Tune Random Search” step to ensure the maximum R^2 value was achieved.

Following this, Bayesian optimization was applied to refine the hyperparameter configuration further. This method defined a narrower range around the optimal values identified by random search and used a probabilistic model to explore the hyperparameter space efficiently. The optimization process was repeated iteratively until the highest R^2 value was obtained. The final optimized hyperparameters were then evaluated on an unseen test set, and R^2 values from CV and the test set were compared to check for overfitting. If overfitting was detected, either the process was restarted from feature engineering, or hyperparameters were further tuned using random search. When no overfitting was observed, the final optimized configuration was selected. This procedure is repeated for all five models under consideration—XGB, RF, SVR, GPR, and FNN. The systematic approach ensures that the models are trained and tuned to achieve optimal performance while minimizing the risk of overfitting.

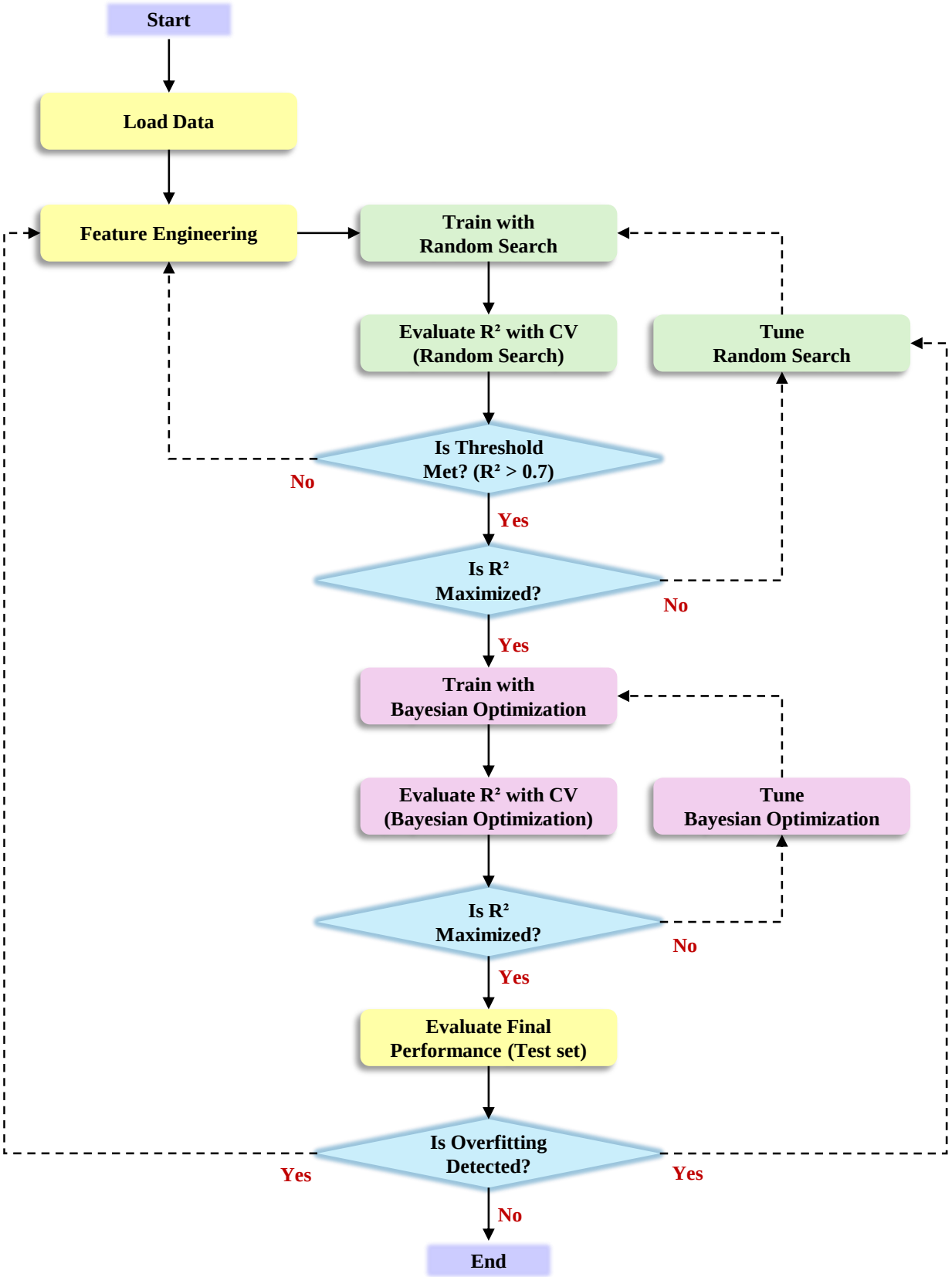


Figure 4-7. Flowchart of the model training and hyperparameter optimization process.

Table 4-2. Hyperparameters explored for each ML model, their definitions, ranges, and final selected values used in this study.

ML Model	Hyperparameters	Description	Parameter Space (Random Search)	Final Value (Bayesian Optimization)
XGB	n_estimators	Number of boosting rounds	100-1000	686
	max_depth	Max tree depth	3-16	13
	learning_rate	Step size for updates	[0.01, 0.1, 0.2]	0.01
	subsample	Fraction of samples for training each tree	[0.7, 0.8, 0.9]	0.7
	colsample_bytree	Fraction of features for each tree	[0.7, 0.8, 0.9]	0.7
RF	n_estimators	Number of decision trees	100-1000	660
	max_depth	Max tree depth	5-50	45
	min_samples_split	Min samples to split a node	[2, 5, 10]	2
	min_samples_leaf	Min samples at a leaf node	[1, 2, 4]	1
	max_features	Max features for tree splits	['sqrt', 'log2']	'log2'
SVR	Kernel	Kernel function type	['linear', 'poly', 'rbf', 'sigmoid']	'rbf'
	C	Regularization parameter	10^{-3} - 10^{3}	1.36
	epsilon	Insensitivity parameter for error	0.01 - 0.5	0.39
	degree	Degree for polynomial kernel	[2, 3, 4, 5]	5
	gamma	Kernel coefficient	['scale', 'auto']	'auto'
GPR	kernel	Combination of Constant and RBF kernels	[C(1, (10^{-4}, 10^{3})) * RBF(1, (10^{-6}, 10^{2})), C(1, (10^{-4}, 10^{3})) * RBF(10, (10^{-6}, 10^{2}))]	C(1.59) * RBF (length_scale=3.06)
	alpha	Noise level	[10^{-1}, 10^{-2} , 10^{-3}, 10^{-4}]	0.11
	n_restarts_optimizer	Number of optimizer restarts	[0,1,2,3]	0
FNN	hidden_layer_sizes	Neurons in hidden layer	50-200	66
	activation	Activation function	['relu', 'tanh', 'logistic']	'tanh'
	solver	Optimization algorithm	['adam', 'sgd']	'sgd'
	alpha	Regularization parameter	[0.0001, 0.001, 0.01]	0.09
	learning_rate	Learning rate schedule	['constant', 'invscaling', 'adaptive']	'constant'
	batch_size	Mini-batch size	['auto', 64, 128]	64
	max_iter	Max iterations (epochs)	[200, 400, 600]	489

4.3. Results and Discussion

4.3.1. Distribution of Surface Roughness (*Sa*) Measurement

The surface roughness (*Sa*) distributions shown in Figure 4-8(a) and Figure 4-8(b) reveal distinct patterns across the four vertical sides (Front, Left, Back, Right) of the build plates. For Build Plate 1, the Right Side exhibits a narrow distribution with a high peak around 14–15 µm, indicating a more uniform surface roughness on this side. In contrast, the Front and Left Sides show broader distributions with lower peaks, spanning a wider range of *Sa* values, which reflects greater variability in surface roughness. The Back Side follows a similar broader pattern to the Front and Left Sides but is distinctly shifted toward higher *Sa* values, frequently peaking around 16–18 µm, suggesting that this side is more affected by external influences. Build Plate 2 exhibits similar trends but with slightly lower peak magnitudes, suggesting that the process is generally consistent across build plates, with minor deviations due to build plate-specific factors. The variations in distribution width and peak position among the sides highlight the role of external factors, such as heat dissipation direction, gas flow, or the presence of spatter, in surface roughness formation. These observations emphasize the importance of in-situ monitoring for capturing side-specific and build plate-specific variations. By incorporating extracted features from photodiode sensor data, the ML model can achieve improved predictive accuracy by accounting for these external influences, which are otherwise overlooked when relying solely on process parameters.

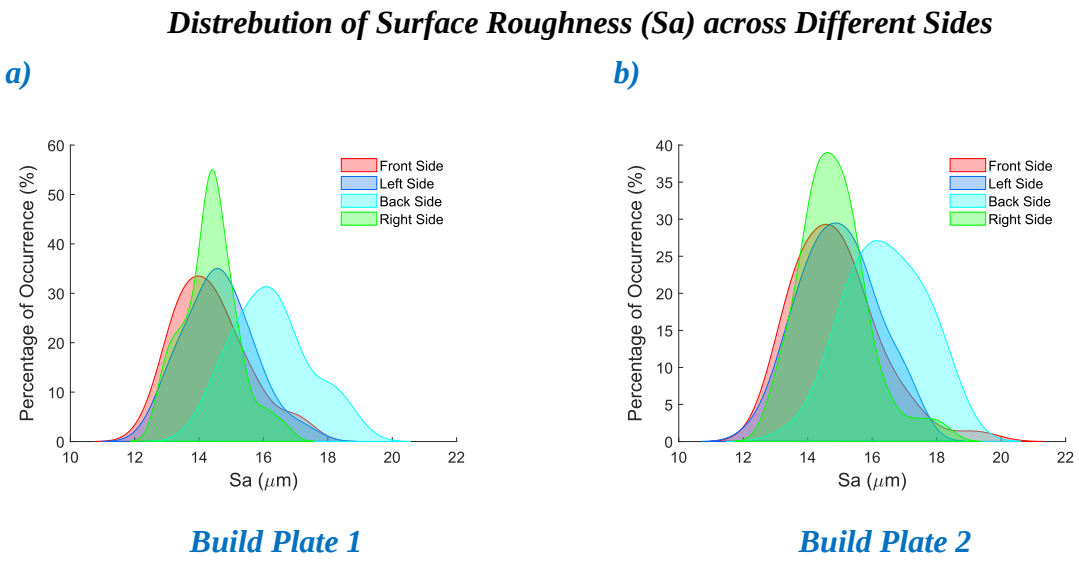


Figure 4-8. Surface roughness (Sa) distributions for the four vertical sides (Front, Left, Back, Right) of two build plates: (a) Build Plate 1, (b) Build Plate 2. The Right Side shows a narrower, more uniform distribution, while the Front, Left, and Back Sides exhibit broader distributions, with the Back Side shifted toward higher roughness values. Differences between build plates highlight the influence of external factors.

4.3.2. Cross-Validation Analysis

During model training, cross-validation was employed to evaluate performance, as described in Section 4.2.4.3. Cross-validation is a statistical technique used to evaluate the predictive performance of a model by splitting the trainset into multiple subsets (or folds). The model is iteratively trained on a portion of the folds and validated on the remaining ones. This ensures that the evaluation is robust and minimizes the influence of random fluctuations in the data.

As explained earlier, the input features included three groups: process parameters, time-domain features extracted from MPM, and frequency-domain features from MPM. Among the time-domain features, "Clustered Light Intensity" was used due to its demonstrated effectiveness in photodiode signal processing [5], [66]. The study employed the Self-Organizing Map (SOM) algorithm to cluster the light intensity data. SOM is an unsupervised learning algorithm designed to cluster input data by organizing it into a grid of nodes, where each node represents a group of similar data points. For the one-dimensional light intensity signal used in this study, SOM clusters the data into a 1 × N grid [75], [76]. The centroid of each cluster, representing the average of the assigned data points, is then used as a feature in the "Clustered Light Intensity" group.

To determine the optimum number of clusters (N) for light intensity data, eight different cluster numbers (N = 3 to 10) were tested. Additionally, the study evaluated the EMZ parameter, which, as mentioned before, defines the distance from the edge of the part used in feature extraction. Ten EMZ values ranging from 40 µm to 400 µm (in 40 µm intervals) were analyzed. This resulted in 80 conditions (8 values of N × 10 values of EMZ) being tested using 5-fold cross-validation. For each condition, the average R^2 (which should be high) and standard deviation of R^2 (which should be low) were calculated. Due to the computational expense of fine-tuning hyperparameters for these 80 conditions, this step was performed only on two models (XGB and RF) out of the five models evaluated in this study (XGB, RF, SVR, GPR, NN). These models were selected for their proven high performance and efficiency in handling complex datasets. This selective approach balanced between computational efficiency and the need for robust evaluation.

The results are presented in Figure 4-9 while revealing the following observation:

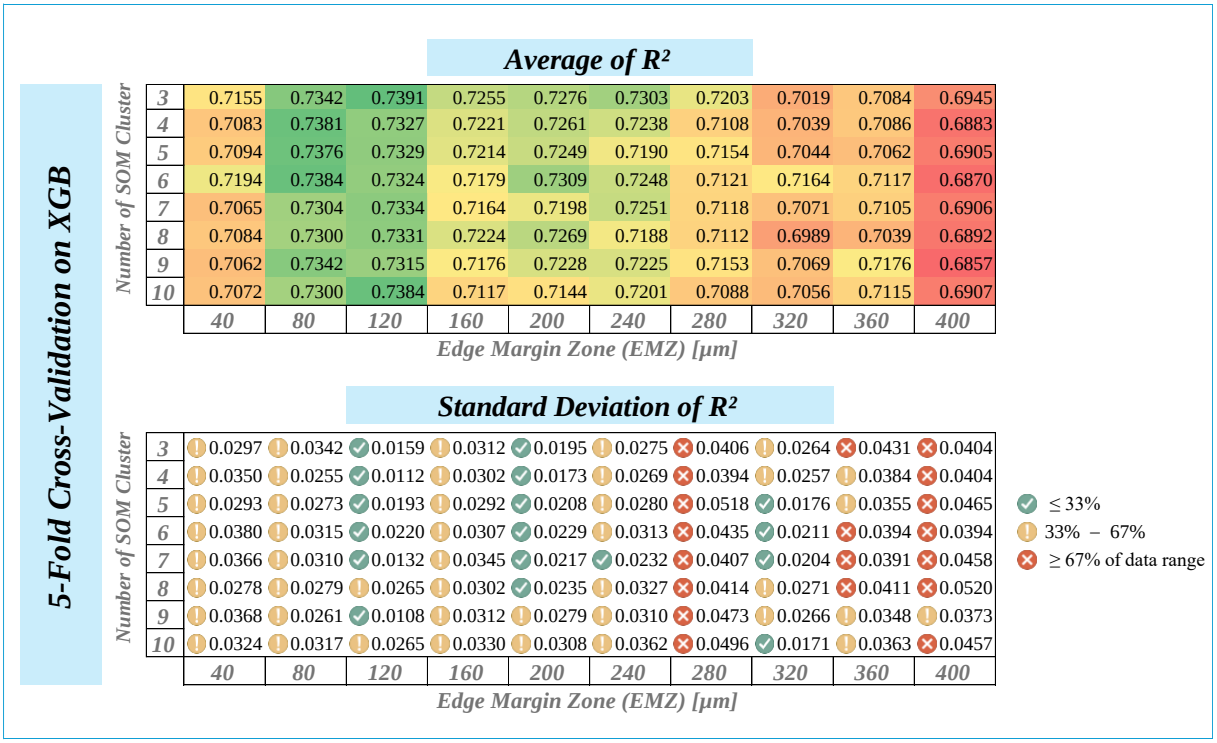
1) **XGB Model**: The best performance, with a high average R^2 and low standard deviation of R^2, was achieved at an EMZ of 120 µm and lower cluster numbers (N = 3 to

5). This indicates that fewer clusters and a moderate edge margin lead to more accurate and stable predictions of surface roughness.

2) RF Model: An interesting trend emerges, where the best performance is achieved as the parameters approach an EMZ of 120 µm and N = 3. This trend highlights the strong correlation between these parameters and improved model performance, suggesting that focusing on smaller clusters and this specific edge margin yields consistent and reliable results.

These findings confirm that an EMZ of 120 µm, corresponding to three times the layer thickness, is the optimal region of the vertical sides to consider for feature extraction. The results across both models (XGB and RF) validate the choice of EMZ = 120 µm and N = 3 as the most effective parameters. Consequently, all subsequent analyses and prediction in this study are based on these optimal values.

a)



b)

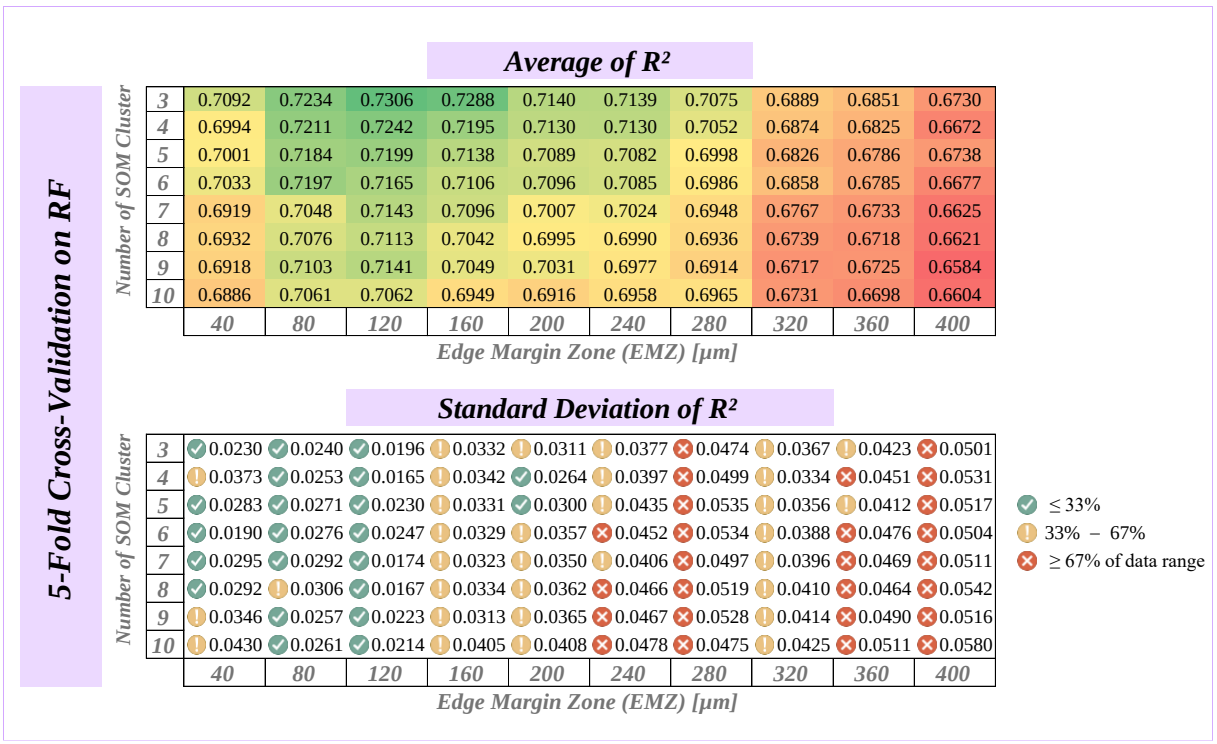


Figure 4-9. Evaluation of average R² and standard deviation of R² across different cluster numbers (N) and edge margin zones (EMZ) using 5-fold cross-validation for (a) XGB and (b) RF models. Optimal performance is achieved at EMZ = 120 µm and N = 3, indicating the most accurate and stable predictions for surface roughness.

Figure 4-10 shows the violin plots of R^2 and RMSE distributions for the five models (XGB, RF, SVR, GPR, and FNN) based on 5-fold cross-validation with EMZ = 120 µm and N = 3. The plots highlight both central tendency and variability in model performance. For R^2, XGB achieves the highest median and smallest interquartile range (IQR), demonstrating superior predictive accuracy and consistency. RF follows closely, with a slightly lower median and marginally wider IQR, while GPR shows a competitive median but greater variability. SVR and FNN exhibit lower medians and broader distributions, indicating reduced accuracy and consistency. For RMSE, XGB and RF show low medians and tight IQRs, confirming strong performance in minimizing prediction errors. GPR achieves the lowest median RMSE but shows higher variability, while SVR and FNN demonstrate higher medians and broader spreads, reflecting less reliable predictions. Overall, XGB is the best-performing model, combining high R^2, low RMSE, and consistency across folds. RF follows closely, offering comparable accuracy and reliability. These findings validate the selection of XGB and RF for determining optimal EMZ and N values in earlier analyses, as their stability and predictive power distinguish them from the other models.

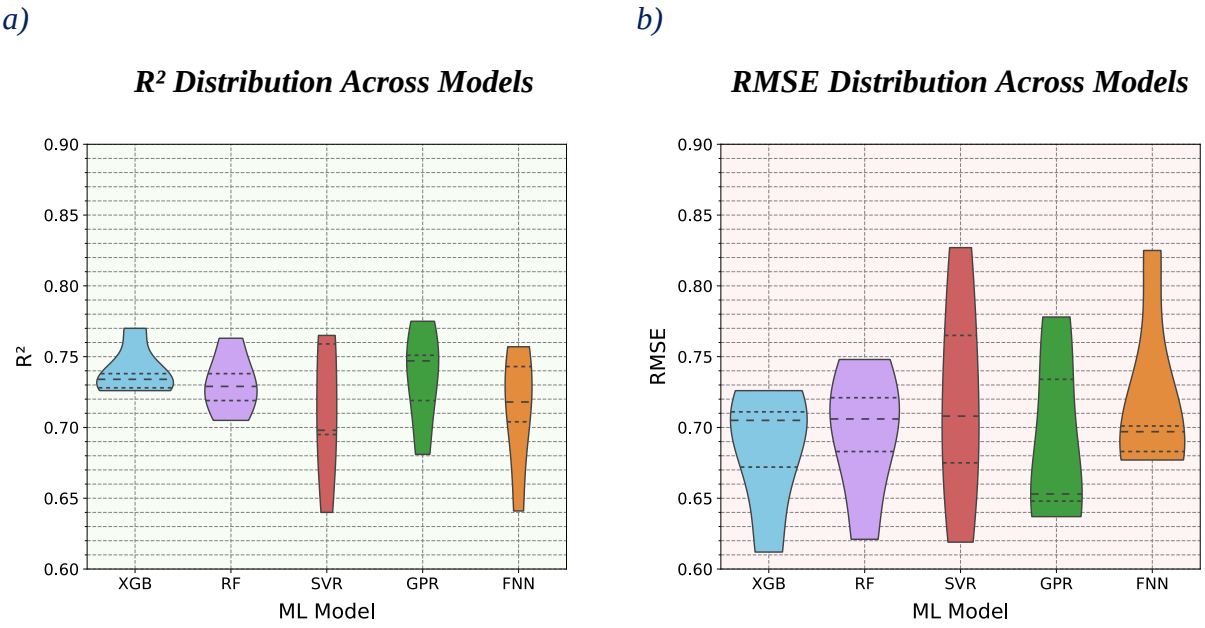
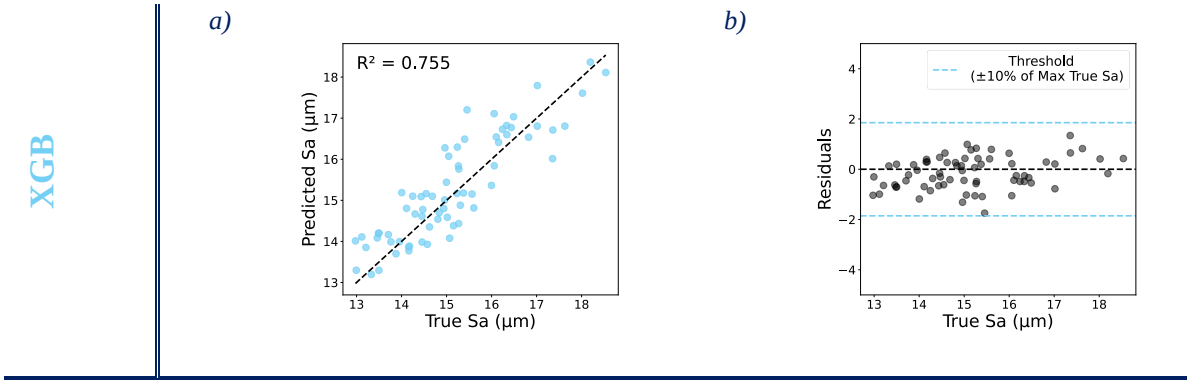


Figure 4-10. Violin plots of R^2 (a) and RMSE (b) for five models using 5-fold cross-validation with EMZ = 120 µm and N = 3. XGB and RF achieve the highest accuracy and lowest error with minimal variability, outperforming the other models.

4.3.3. Models' Performance Evaluation on Unseen Test Data

4.3.3.1. Coefficient of Determination (R^2) Analysis

To evaluate the performance of the models, an unseen test set was used to assess generalizability and accuracy. It is well known that R^2 values closer to 1 indicate better model performance and a stronger correlation between predictions and actual values. Figure 4-11 presents the R^2 values for each model on the unseen test set, alongside residual plots (True *Sa* - Predicted *Sa*) to provide further insights into the models' performance. A threshold of ±10% of the true *Sa* value is shown in the residual plots to evaluate prediction accuracy. Residuals falling within this range suggest acceptable model performance, while residuals close to zero indicate more precise predictions. As shown in the figure, all models achieve R^2 values above 74%, demonstrating strong predictive capabilities within the LPBF context that is usually considered as extremely complex process with many anomalies. Among them, RF and GPR perform slightly better, with R^2 of approximately 78%. However, the residual plots reveal that the RF model stands out, with the fewest residuals approaching the ±10% threshold, highlighting its ability to maintain high accuracy across the test set. While other models also perform well, their residuals show more variability, with a greater number of data points approaching the threshold. Although XGB has a slightly lower R^2 value than RF and GPR, its performance remains competitive, consistent with earlier cross-validation analysis. Overall, the RF model demonstrates the best balance of accuracy and consistency on the test set, confirming its suitability for surface roughness prediction.



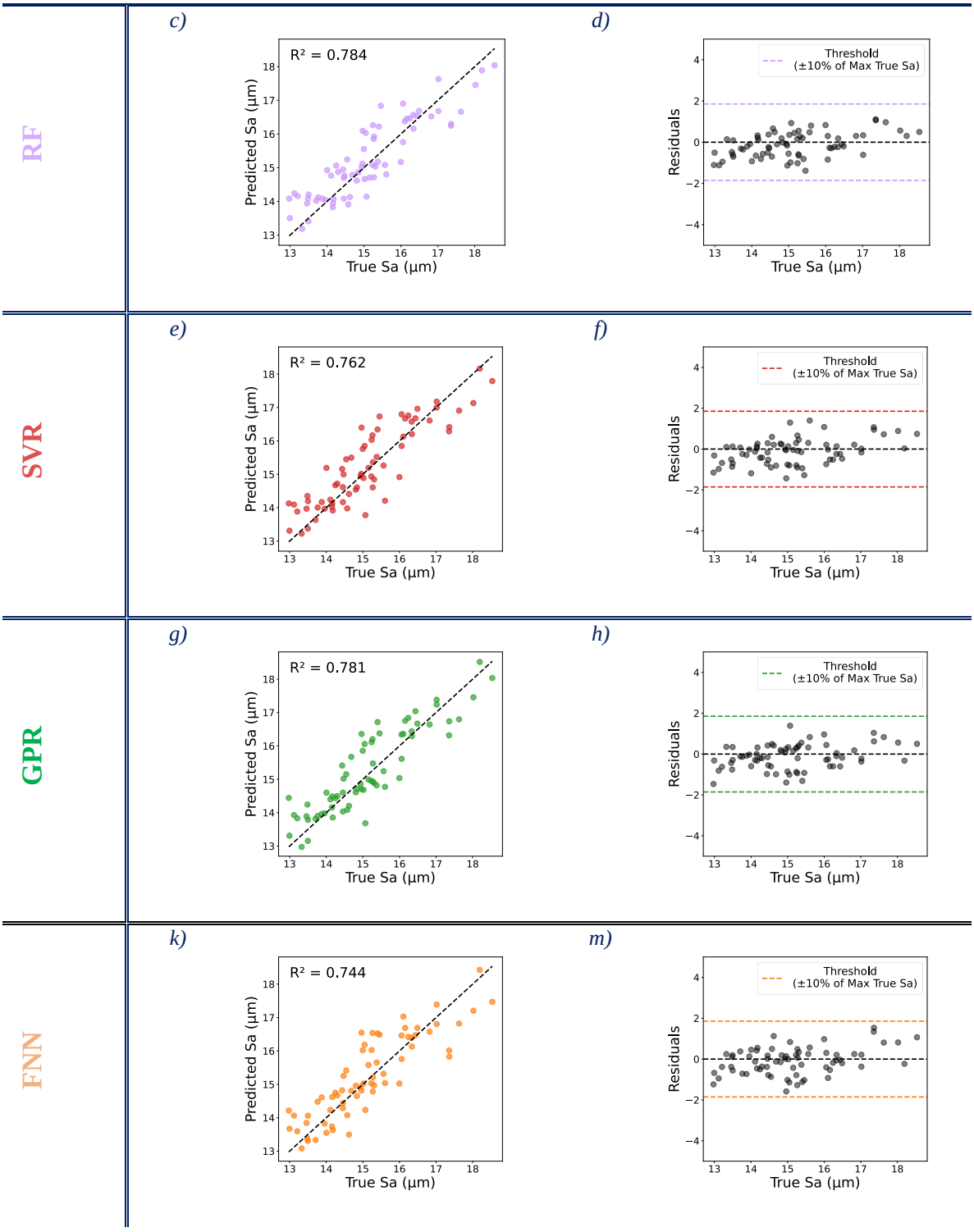


Figure 4-11. Predicted vs. true Sa values (a, c, e, g, k) and residual plots (b, d, f, h, m) for XGB, RF, SVR, GPR, and FNN models on the unseen test set. RF achieves the highest consistency with the fewest residuals near the ±10% threshold, highlighting its superior predictive accuracy.

4.3.3.2. Side-Specific Error Analysis

As the objective of this study is to predict surface roughness for all vertical sides, the performance of the models on the unseen test set was evaluated specifically for each side. Figure 4-12 presents the results for the two best-performing models, XGB and RF, in terms of Mean Absolute Percentage Error (MAPE) and Mean Absolute Error (MAE). By comparing the two models, RF demonstrates better performance across all sides, achieving a lower error rate consistently.

When comparing the sides, both models exhibit better performance on the Back Side and Right Side. This can be attributed to the *Sa* distribution characteristics of these sides. As discussed earlier (Figure 4-8), the Back Side distribution was shifted toward higher *Sa* values, which made its roughness values more distinguishable and easier for the models to learn. Similarly, the Right Side showed a narrow distribution with a high peak, indicating a more uniform surface roughness. This uniformity likely contributed to the models' improved prediction accuracy for this side.

In contrast, the Front Side and Left Side display higher error rates in both models. This can be attributed to the broader distributions of *Sa* values for these sides, which reflect greater variability in surface roughness. Furthermore, the distributions of the Front and Left Sides surface roughness value overlap significantly in Figure 4-8, as discussed previously. This overlap likely introduced ambiguity, making it more challenging for the models to distinguish between these sides and resulting in slightly higher prediction errors. However, the maximum MAE, observed for the Front Side, is only 0.58 μm with a MAPE of 4.02% (by RF), which still reflects strong model performance and further confirms RF's robustness for side-wise surface roughness prediction.

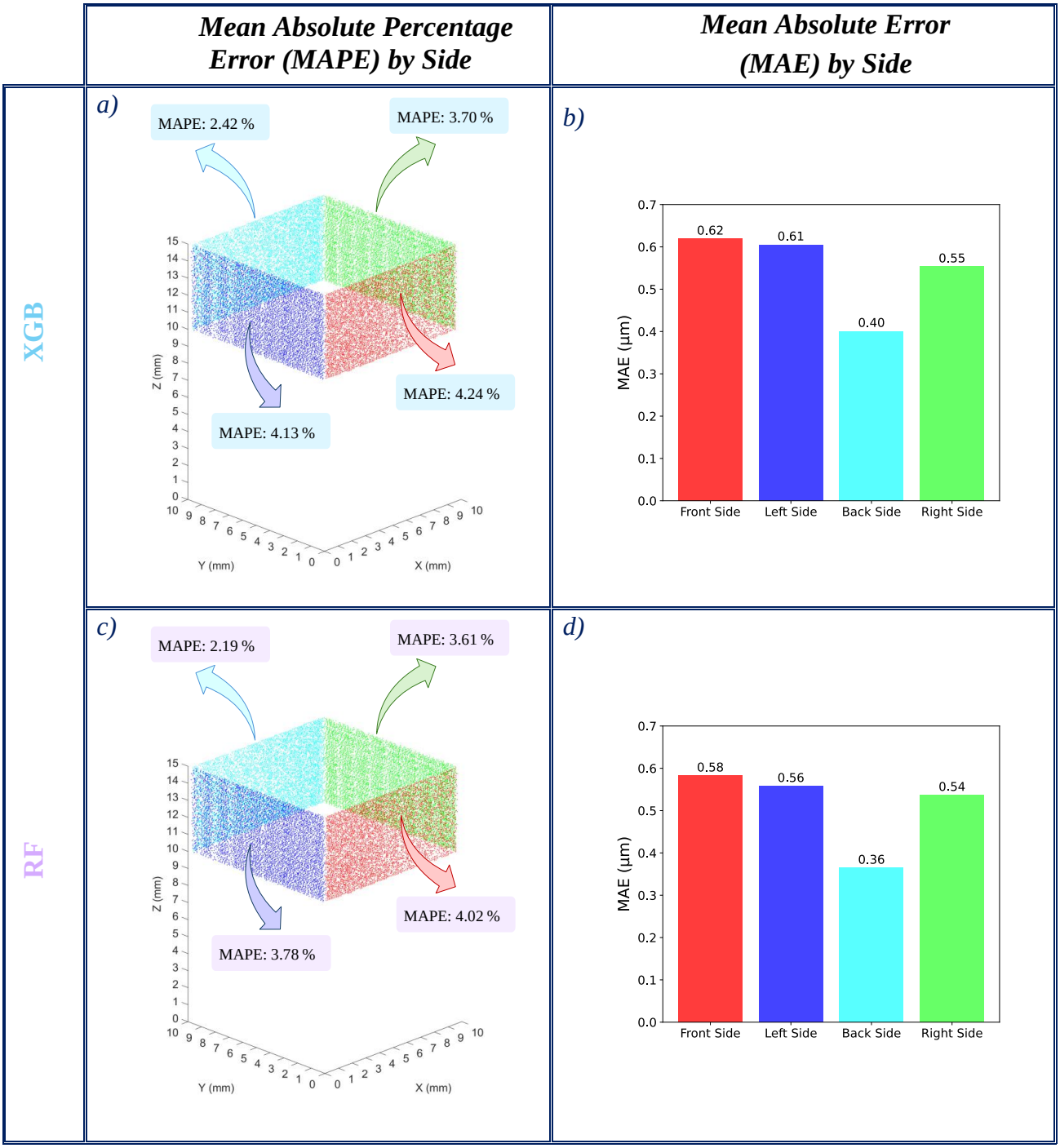


Figure 4-12. Side-wise evaluation of the best models (XGB and RF) using Mean Absolute Percentage Error (MAPE) and Mean Absolute Error (MAE) on the unseen test set. RF demonstrates better performance across all sides, with the Back Side and Right Side showing the lowest errors due to their distinct and uniform Sa distributions.

4.3.3.3. Feature Combination Analysis

As discussed earlier, the input features were divided into three groups, including process parameters (PP), time-domain features extracted from MPM signals, and frequency-domain features extracted from MPM signals. This section investigates the models' performance when different combinations of these input features are used, offering insights into the relative significance of each group and their contributions to the overall performance.

Figure 4-13 compares the performance of the models under four feature configurations: (1) using only process parameters, denoted as PP in the figure, serving as the baseline (ex-situ approach), (2) PP combined with frequency-domain features from MPM signals, (3) PP combined with time-domain features from MPM signals, and (4) all three feature groups combined. The evaluation metrics used are R^2, MAE, RMSE, and MAPE. Higher R^2 and lower error metrics indicate better model performance.

Figure 4-13(a) shows the R^2 values for all models across the four configurations. When using only process parameters (baseline), all models achieve very low R^2 values (below 0.4 for XGB, RF, SVR, and GPR, and below 0.5 for FNN), indicating that the relationship between process parameters and surface roughness is highly non-linear and cannot be captured effectively by conventional methods alone. Adding frequency-domain features significantly improves R^2 values, demonstrating the importance of the dominant frequency and amplitude features in enhancing model performance. A more notable increase in R^2 is observed when time-domain features, such as clustered light intensity, skewness, variance, and autocorrelation, are added to process parameters. This highlights the critical role of time-domain features in capturing complex patterns in the data. Finally, combining all three feature groups (PP, frequency-domain, and time-domain features) achieves the highest R^2 values across all models (e.g., 0.78 for RF), validating the effectiveness of the selected features in improving predictive accuracy.

Figure 4-13(b), Figure 4-13(c), and Figure 4-13(d) present MAE, RMSE, and MAPE values, respectively. Consistent with the R^2 results, using only process parameters results in the highest errors, reflecting the limitations of the baseline approach. Adding frequency-domain features reduces the error values, and incorporating time-domain features further improves model performance. The lowest errors are achieved when all three feature groups are combined, confirming that the integration of in-situ monitoring data with process parameters significantly enhances model accuracy.

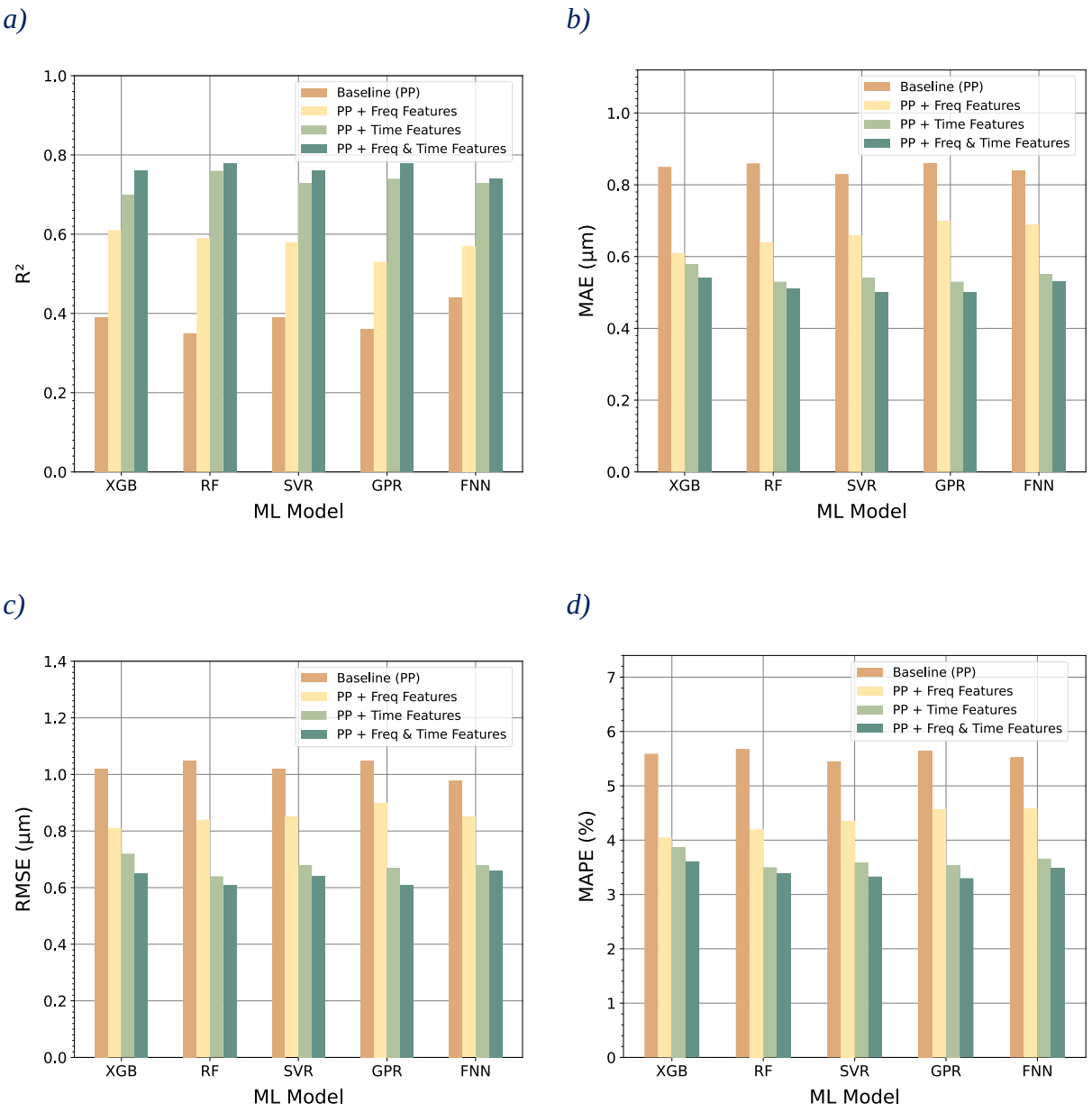


Figure 4-13. Performance comparison of models on the unseen test set with different combinations of input features (PP, frequency-domain, and time-domain) using R², MAE, RMSE, and MAPE. Combining all feature groups results in the highest R² and lowest error metrics, demonstrating the effectiveness of integrating in-situ features with process parameters.

4.3.3.4. Training Size Sensitivity Analysis

Figure 4-14 illustrates how training set size affects the performance of the models on the unseen test data. The performance is evaluated using R^2 (left) and RMSE (right) as the key metrics, with varying training set sizes ranging from 53 to 268 data points (20%–100% of the train set). This analysis provides insights into how the quantity of training data influences the models' ability to

generalize and make accurate predictions. As the training size increases, all models show improved predictive accuracy (higher R^2) and reduced prediction error (lower RMSE).

GPR and RF consistently outperform the other models, achieving the highest accuracy and lowest error rates, particularly at larger training sizes. GPR demonstrates strong robustness even with smaller datasets, maintaining reliable performance with limited data. XGB also performs well, steadily improving as training size grows, maintaining competitive accuracy but slightly behind GPR and RF. SVR and FNN exhibit greater sensitivity to training size, starting with lower performance but improving substantially with more data. By the largest training size, SVR matches XGB in accuracy, while FNN shows notable improvement but remains less consistent.

Overall, GPR and RF exhibit the best performance, achieving high accuracy and low error rates across all training sizes, while SVR and FNN highlight the importance of larger datasets for enhanced generalization. These results underscore the critical role of training size in determining model effectiveness for surface roughness prediction.

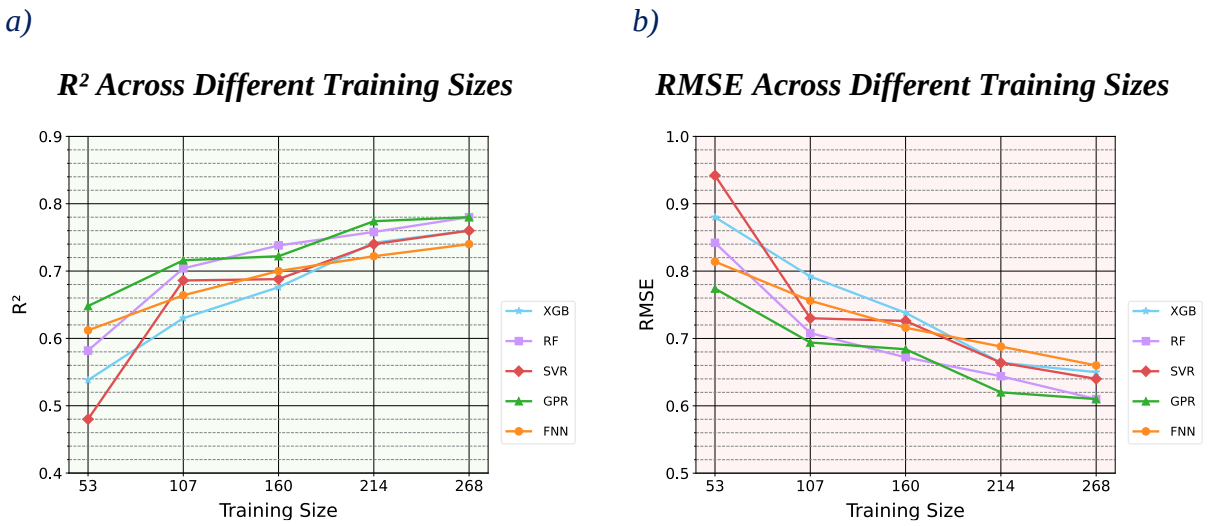


Figure 4-14. Sensitivity analysis of training set size on model performance on the unseen test set, showing improvements in R^2 and RMSE as the training size increases for all models. GPR and RF achieve the best accuracy and lowest errors.

4.3.4. Feature Importance Assessment

Figure 4-15 illustrates the feature importance for XGB and RF, the two best-performing models identified in the previous analyses. Feature importance is presented only for these models because they inherently provide interpretable metrics, unlike SVR, GPR, and FNN, which do not offer direct feature attribution mechanisms.

In the XGB model, process parameters dominate, contributing 67.6% to the overall performance, with VED and Laser Power identified as the most significant features. However, despite their dominance, relying solely on process parameters resulted in an R^2 of only 0.39 (Figure 4-13), highlighting the importance of incorporating additional features. By integrating time-domain features, which account for 28.5% of the importance (e.g., Autocorrelation and Skewness), and frequency-domain features, which contribute 3.9%, the model achieved a significantly improved R^2 of 0.76 (Figure 4-13). This demonstrates how the inclusion of in-situ monitoring data strengthens the model's predictive capabilities.

The RF model, in contrast, places greater emphasis on time-domain features, which account for 67.2% of the overall contribution. Key time-domain features include Clustered data, Skewness, and Autocorrelation. Process parameters contribute 23.7%, again dominated by VED, while frequency-domain features add 9.2%, showing slightly more impact compared to XGB.

The comparison reveals that while XGB heavily relies on process parameters, RF leverages time-domain features more effectively, explaining RF's slight performance advantage in certain scenarios. Both models, however, underscore the importance of combining process parameters with in-situ monitoring data. Time-domain features, in particular, play a critical role in capturing complex temporal patterns, while frequency-domain features, though less impactful, still contribute meaningful information for surface roughness prediction. These findings reinforce the value of integrating diverse feature types to enhance predictive accuracy.

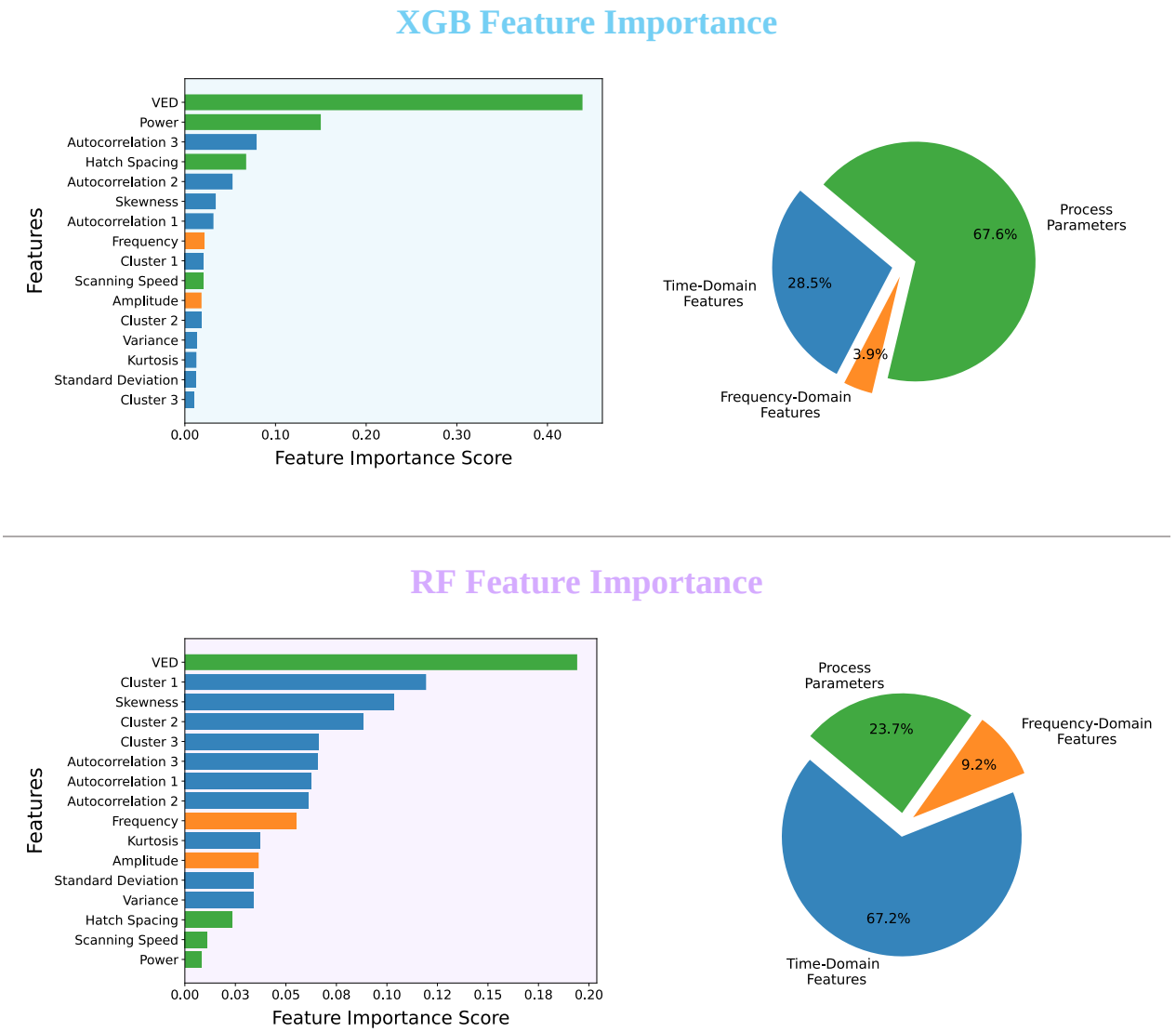


Figure 4-15. Feature importance analysis for XGB and RF models. XGB relies heavily on process parameters (67.6%), while RF emphasizes time-domain features (67.2%). Although XGB shows a strong reliance on process parameters, using only process parameters results in an R^2 of 0.35, highlighting the importance of integrating in-situ features to improve performance, increasing R^2 to 0.76. (Note: C1-C3 represent the centroids of three clusters of light intensity using SOM).

4.4. Summary

This study examined the correlation between vertical side surface roughness and the light intensity signal emitted from the melt pool, captured by an in-situ photodiode from regions adjacent to vertical surfaces during the printing process. The collected signal data were processed for each vertical side, with key features extracted from both the time and frequency domains. These

extracted features, along with relevant process parameters, were used as inputs for various ML models. The models were developed to predict surface roughness for all four vertical sides (Front, Left, Back, and Right). Their predictive accuracy and robustness were assessed using an unseen test dataset, ensuring the model's reliability and applicability to different LPBF conditions.

Chapter 5. Conclusion and Future Work

5.1. Conclusions of In-Situ Top Surface Roughness Prediction

The primary objective of this thesis was to develop a novel ML-based approach for in-situ surface roughness prediction in Ti-6AL-4V components manufactured via LPBF. The predictive approach relies on real-time monitoring of light intensity emitted from the melt pool during the manufacturing process using photodiode sensor, coupled with several process parameters and geometrical features as inputs. Six distinct ML algorithms were utilized for this study, namely RF, GB, XGB, SVM, NN, and LSTM. Surface roughness is classified into four classes based on *Sa* values (Class 1: $Sa < 8$ µm, Class 2: $8 \leq Sa < 14$ µm, Class 3: $14 \leq Sa < 22$ µm, and Class 4: 22 µm $\leq Sa$), showing severe imbalance in the dataset, particularly in Class 4. The main aim of this study was to predict *Sa* class for individual small cells (690 µm × 510 µm) across a part, enabling predictions for even the edges and corners rather than merely assigning a single class to the entire part. To achieve this, new input features were introduced, including clustered light intensity group, process parameters group, spatter region index group, and edge proximity index group, and their influence on prediction accuracy was investigated. Evaluation metrics are comprehensively discussed, including accuracy, precision, recall, F1-score, confusion matrix, and ROC curve analysis. The following conclusions can be drawn from this study:

- The distribution of light intensity in each part is influenced by the scanning direction and VED value, and it correlates with the height distribution of the part top surface.
- Incorporating additional input features enhances model efficiency, leading to improved evaluation metric scores.
- When dealing with imbalanced data, the SMOTE technique outperforms class weighting, resulting in a 10% increase in the F1-score.
- While models like NN and LSTM demonstrate proficiency in predicting Classes 1, 2, and 3, they face challenges with Class 4 predictions.
- RF exhibits superior performance, with a weighted F1-Score of 0.71, a micro-average AUC of 0.89, and the best confusion matrix among all models, showcasing resilience to data imbalances.

- XGB also yields promising results, closely following RF.
- Both RF and XGB are the fastest models evaluated.
- By reducing the size of the training set, RF and XGB outperform other models when the data points are still sufficient. However, for very limited data points, XGB may be the preferable option.
- Through analysis of feature importance generated by RF, it is evident that excluding any input feature group alters the importance score. However, the clustered light intensity feature consistently emerges as significant, highlighting its effectiveness in prediction.

5.2. Conclusions of In-Situ Vertical Side Surface Roughness Prediction

This study also introduced a novel framework for in-situ prediction of vertical surface roughness in LPBF using a photodiode sensor integrated with ML algorithms. Key features from time- and frequency-domain photodiode signals were combined with process parameters to predict surface roughness accurately. Five ML models (XGB, RF, SVR, GPR, and FNN) were evaluated, and the following conclusions can be drawn from this study:

- Cross-validation analysis identified optimal clustering numbers (N = 3) and edge margin zones (EMZ = 120 μm), achieving high accuracy and stability in surface roughness prediction.
- Based on the 5-fold cross-validation, violin plots of R^2 and RMSE showed that XGB achieved the highest median R^2 and lowest RMSE with the smallest variability, demonstrating superior consistency and accuracy across folds. RF closely followed, balancing high accuracy and reliability, while GPR, SVR, and FNN exhibited greater variability and reduced consistency.
- All models achieved R^2 values above 74% on unseen test data, with RF and GPR performing best (R^2 = 0.78), demonstrating superior accuracy and consistency.
- The Back Side, with its shifted distribution toward higher *Sa* values, was more distinguishable, aiding model predictions (RF: MAPE = 2.19%). The Right Side's narrow, high-peaked distribution reflected uniform roughness and lower variability, improving accuracy (RF: MAPE = 3.61%). In contrast, the broader and overlapping distributions of the Front and Left Sides made them more relatively challenging to predict with high accuracy (RF-Front: MAPE = 4.02%, RF-Left: MAPE = 3.78%).

- Using only process parameters resulted in poor performance ($R^2 < 0.4$). Adding frequency-domain features improved R^2, while time-domain features further enhanced predictions. Combining all feature groups resulted in the highest R^2 values (RF = 0.78, XGB = 0.76).
- GPR and RF exhibit the best performance, achieving high accuracy and low error rates across all training sizes. SVR and FNN were more sensitive to training size but showed significant improvement with more data.
- XGB relied heavily on process parameters (67.6%) but benefited from adding time-domain features (28.5%), improving R^2 from 0.39 to 0.76. RF emphasized time-domain features (67.2%), with Clustered data, Skewness, and Autocorrelation as key contributors, while frequency-domain features added value (9.2%).

5.3. Future work

The two primary objectives of this thesis were to explore the feasibility of ML for in-situ surface roughness prediction in LPBF and to develop a novel photodiode-based approach for monitoring both top and vertical surface roughness. This study laid the groundwork for applying ML in underexplored areas of LPBF, particularly in scenarios where conventional ML applications such as the reliance on large datasets, may not be directly applicable. By integrating photodiode signals, process parameters, and ML models, this research has demonstrated the potential for real-time monitoring and prediction of surface roughness. While this work represents a significant step forward, further advancements are needed to enhance the accuracy, robustness, and industrial applicability of the developed methods. The following future research directions are recommended to build upon this foundation:

- **Development of an In-Situ Control System for Surface Roughness Adjustment:** A closed-loop control system should be developed to predict and correct surface roughness in real-time by adjusting process parameters (e.g., laser power and scan speed) in subsequent layers. This would reduce part porosity and improve top and vertical surface quality.
- **Integration of Optical Tomography (OT) for Enhanced Roughness Prediction:** Combining OT image analysis with photodiode data could improve roughness prediction for additional surface features, including down-facing and up-facing surfaces. This requires image processing, signal processing, and advanced ML models for more precise roughness detection.

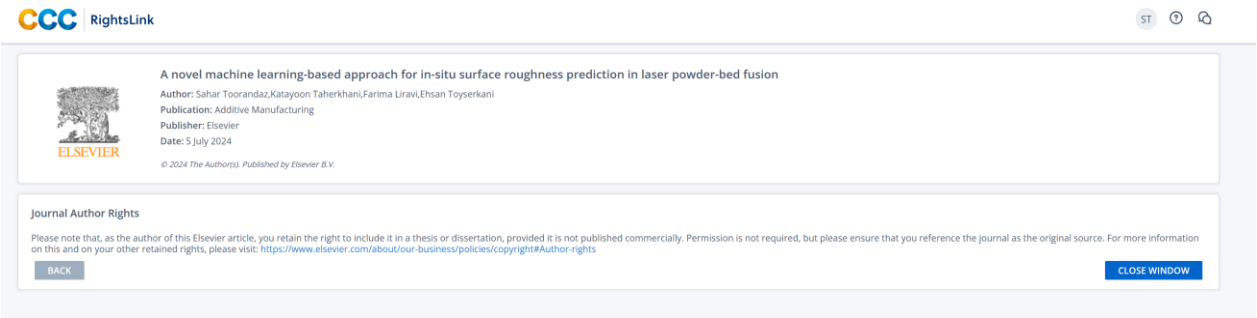
- **Expansion of the Monitoring Framework for Detecting Other Defects:** A multi-sensor fusion approach integrating photodiodes, OT, and other sensors could improve the detection of keyhole porosity and lack of fusion defects, expanding defect-monitoring capabilities beyond surface roughness.
- **Optimization of Process Parameters for Defect Healing:** Future studies should evaluate multiple process parameter sets to optimize laser power adjustments for better defect healing and surface quality enhancement.
- **Evaluation on New Materials:** The developed methodology should be experimentally tested on various alloys, such as Inconel, aluminum, and stainless steel, to assess its baseline adaptability and performance prior to implementing transfer learning techniques.
- **Transfer Learning for Cross-Material Generalization:** Transfer learning techniques should be explored to adapt the developed models for other materials with minimal additional training. This would enable broader applicability of the monitoring framework across various alloys without retraining from scratch.
- **Extension to Complex Geometries**: The current framework should be applied to parts with more complex geometries. While the overall methodology remains applicable, additional tuning and validation are needed to ensure reliable surface roughness prediction across varied part shapes.
- **Validation on Multiple LPBF Systems:** To enhance repeatability and scalability, the approach should be implemented on various LPBF machines to assess its robustness, ensuring it can be reliably applied across different manufacturing platforms for industrial application

Advancing these areas will further improve LPBF process monitoring, quality assurance, and real-time adaptive control for high-precision additive manufacturing.

Letter of Copyright Permission

Chapter 1:

Figure 1-1:



Chapter 2:

Figure 2-1:

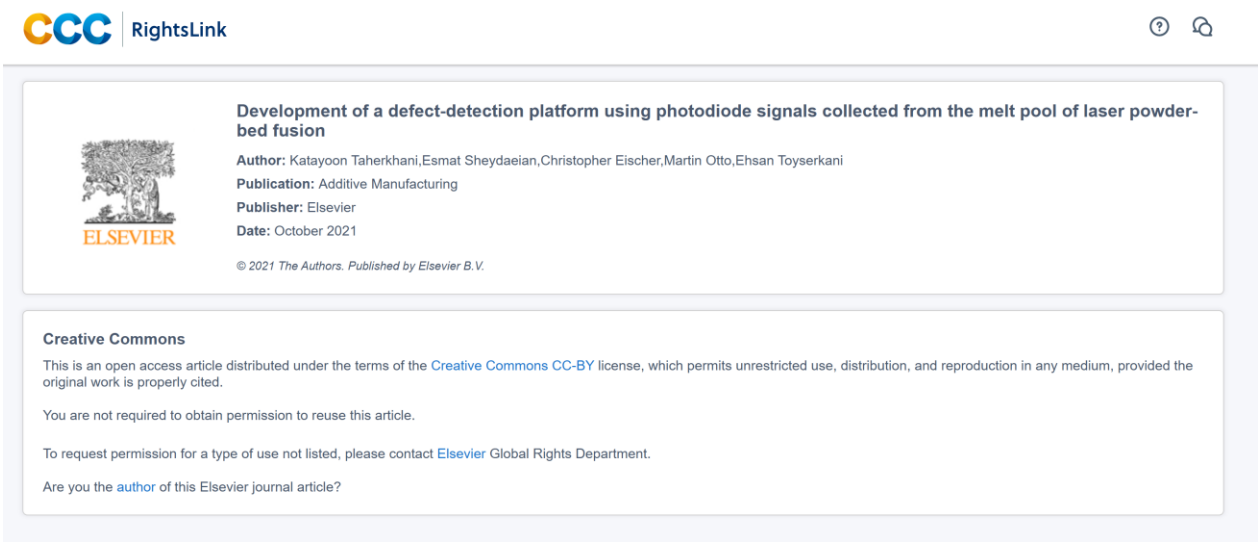
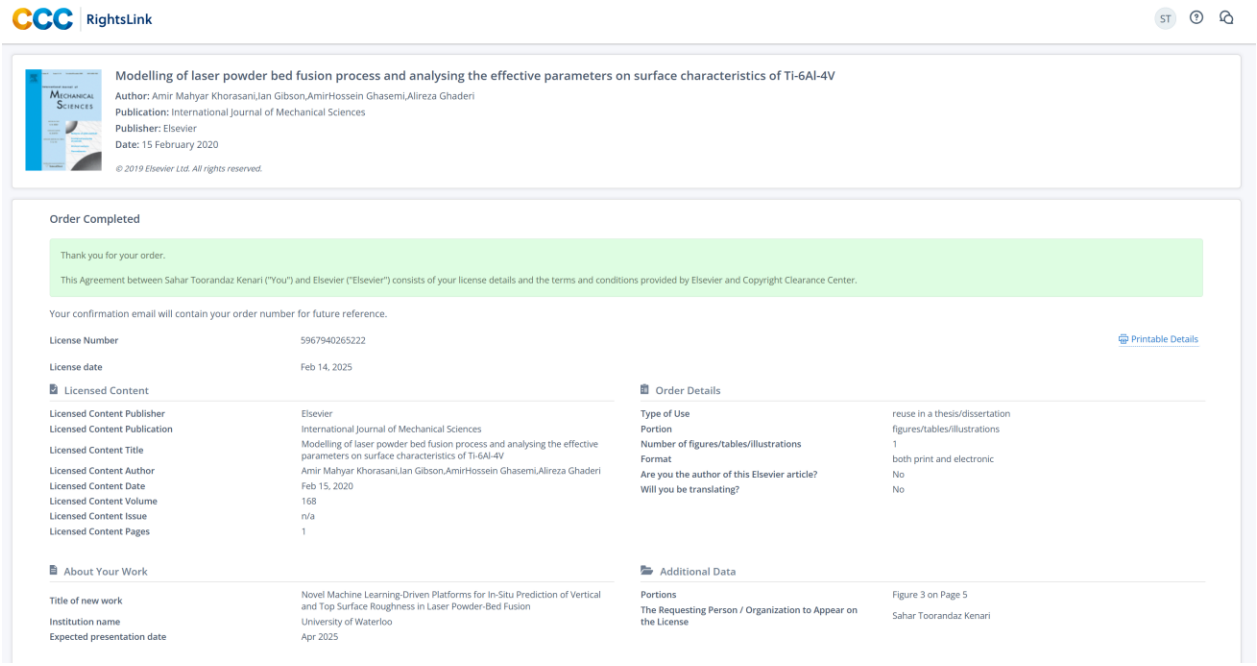


Figure 2-2:



CCC RightsLink

Modelling of laser powder bed fusion process and analysing the effective parameters on surface characteristics of Ti-6Al-4V

Author: Amir Mahyar Khorasani,Ian Gibson,AmirHossein Ghasemi,Alireza Ghaderi
Publication: International Journal of Mechanical Sciences
Publisher: Elsevier
Date: 15 February 2020

© 2019 Elsevier Ltd. All rights reserved.

Order Completed

Thank you for your order.

This Agreement between Sahar Toorandaz Kenari ("You") and Elsevier ("Elsevier") consists of your license details and the terms and conditions provided by Elsevier and Copyright Clearance Center.

Your confirmation email will contain your order number for future reference.

Printable Details

License Number	5967940265222
License date	Feb 14, 2025

Licensed Content

Licensed Content Publisher	Elsevier
Licensed Content Publication	International Journal of Mechanical Sciences
Licensed Content Title	Modelling of laser powder bed fusion process and analysing the effective parameters on surface characteristics of Ti-6Al-4V
Licensed Content Author	Amir Mahyar Khorasani,Ian Gibson,AmirHossein Ghasemi,Alireza Ghaderi
Licensed Content Date	Feb 15, 2020
Licensed Content Volume	168
Licensed Content Issue	n/a
Licensed Content Pages	1

Order Details

Type of Use	reuse in a thesis/dissertation
Portion	figures/tables/illustrations
Number of figures/tables/illustrations	1
Format	both print and electronic
Are you the author of this Elsevier article?	No
Will you be translating?	No

About Your Work

Title of new work	Novel Machine Learning-Driven Platforms for In-Situ Prediction of Vertical and Top Surface Roughness in Laser Powder-Bed Fusion
Institution name	University of Waterloo
Expected presentation date	Apr 2025

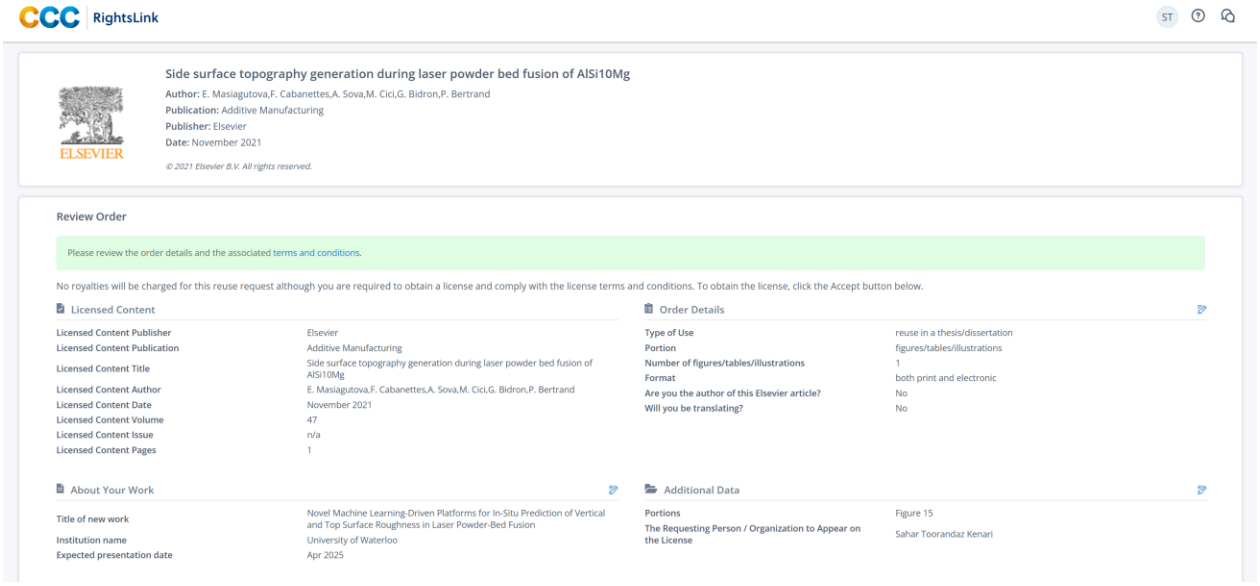
Additional Data

Portions	Figure 3 on Page 5
The Requesting Person / Organization to Appear on the License	Sahar Toorandaz Kenari

Figure 2-3:

© 2021 by the authors. Licensee MDPI, Basel, Switzerland. This article is an open access article distributed under the terms and conditions of the Creative Commons Attribution (CC BY) license (https://creativecommons.org/licenses/by/4.0/).

Figure 2-4:



CCC RightsLink

ST

Side surface topography generation during laser powder bed fusion of AlSi10Mg

Author: E. Masiagutova,F. Cabanettes,A. Sova,M. Cici,G. Bidron,P. Bertrand
Publication: Additive Manufacturing
Publisher: Elsevier
Date: November 2021

© 2021 Elsevier B.V. All rights reserved.

Review Order

Please review the order details and the associated terms and conditions.

No royalties will be charged for this reuse request although you are required to obtain a license and comply with the license terms and conditions. To obtain the license, click the Accept button below.

Licensed Content

Licensed Content Publisher	Elsevier
Licensed Content Publication	Additive Manufacturing
Licensed Content Title	Side surface topography generation during laser powder bed fusion of AlSi10Mg
Licensed Content Author	E. Masiagutova,F. Cabanettes,A. Sova,M. Cici,G. Bidron,P. Bertrand
Licensed Content Date	November 2021
Licensed Content Volume	47
Licensed Content Issue	n/a
Licensed Content Pages	1

Order Details

Type of Use	reuse in a thesis/dissertation
Portion	figures/tables/illustrations
Number of figures/tables/illustrations	1
Format	both print and electronic
Are you the author of this Elsevier article?	No
Will you be translating?	No

About Your Work

Title of new work	Novel Machine Learning-Driven Platforms for In-Situ Prediction of Vertical and Top Surface Roughness in Laser Powder-Bed Fusion
Institution name	University of Waterloo
Expected presentation date	Apr 2025

Additional Data

Portions	Figure 15
The Requesting Person / Organization to Appear on the License	Sahar Toorandaz Kenari

Figure 2-5:

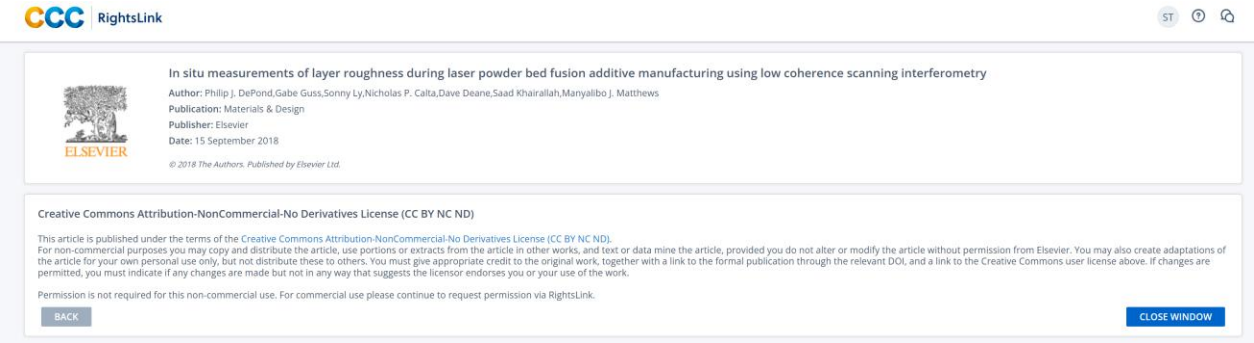
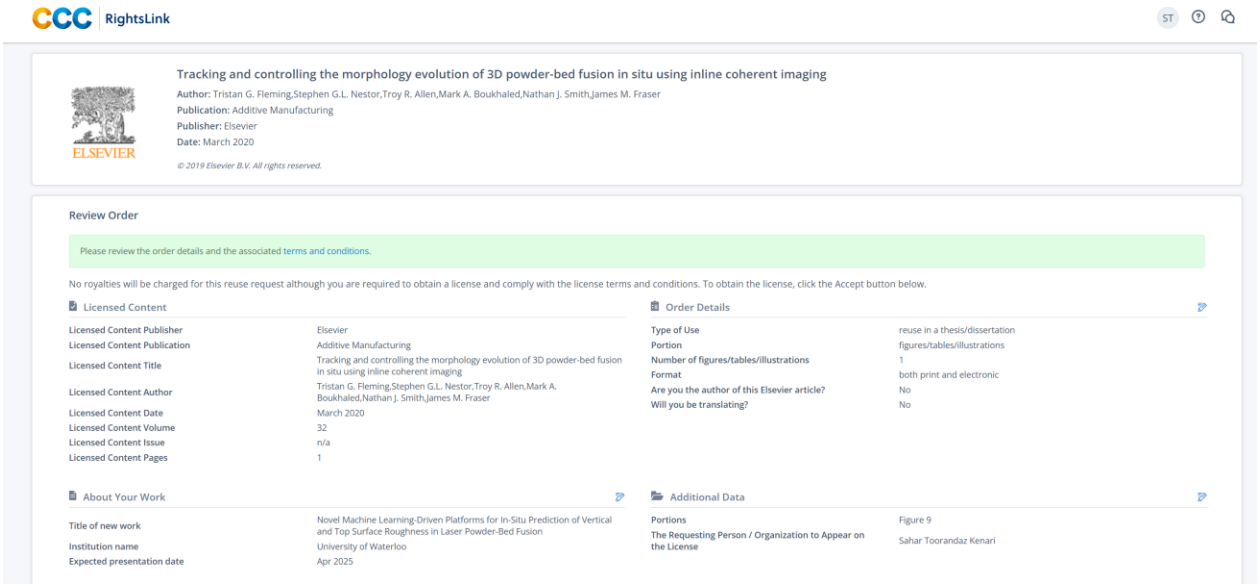

RightsLink
In situ measurements of layer roughness during laser powder bed fusion additive manufacturing using low coherence scanning interferometry
Author: Philip J. DePond,Gabe Guss,Sonny Ly,Nicholas P. Calta,Dave Deane,Saad Khairallah,Manyalibo J. Matthews
Publication: Materials & Design
Publisher: Elsevier
Date: 15 September 2018
© 2018 The Authors. Published by Elsevier Ltd.
Creative Commons Attribution-NonCommercial-No Derivatives License (CC BY NC ND)
This article is published under the terms of the Creative Commons Attribution-NonCommercial-No Derivatives License (CC BY NC ND).
For non-commercial purposes you may copy and distribute the article, use portions or extracts from the article in other works, and text or data mine the article, provided you do not alter or modify the article without permission from Elsevier. You may also create adaptations of the article for your own personal use only, but not distribute these to others. You must give appropriate credit to the original work, together with a link to the formal publication through the relevant DOI, and a link to the Creative Commons user license above. If changes are permitted, you must indicate if any changes are made but not in any way that suggests the licensor endorses you or your use of the work.
Permission is not required for this non-commercial use. For commercial use please continue to request permission via RightsLink.
BACK
CLOSE WINDOW

Figure 2-6:



CCC RightsLink

Tracking and controlling the morphology evolution of 3D powder-bed fusion in situ using inline coherent imaging

Author: Tristan G. Fleming,Stephen G.L. Nestor,Troy R. Allen,Mark A. Boukhaled,Nathan J. Smith,James M. Fraser
Publication: Additive Manufacturing
Publisher: Elsevier
Date: March 2020

© 2019 Elsevier B.V. All rights reserved.

Review Order

Please review the order details and the associated terms and conditions.

No royalties will be charged for this reuse request although you are required to obtain a license and comply with the license terms and conditions. To obtain the license, click the Accept button below.

Licensed Content

Licensed Content Publisher	Elsevier
Licensed Content Publication	Additive Manufacturing
Licensed Content Title	Tracking and controlling the morphology evolution of 3D powder-bed fusion in situ using inline coherent imaging
Licensed Content Author	Tristan G. Fleming,Stephen G.L. Nestor,Troy R. Allen,Mark A. Boukhaled,Nathan J. Smith,James M. Fraser
Licensed Content Date	March 2020
Licensed Content Volume	32
Licensed Content Issue	n/a
Licensed Content Pages	1

Order Details

Type of Use	reuse in a thesis/dissertation
Portion	figures/tables/illustrations
Number of figures/tables/illustrations	1
Format	both print and electronic
Are you the author of this Elsevier article?	No
Will you be translating?	No

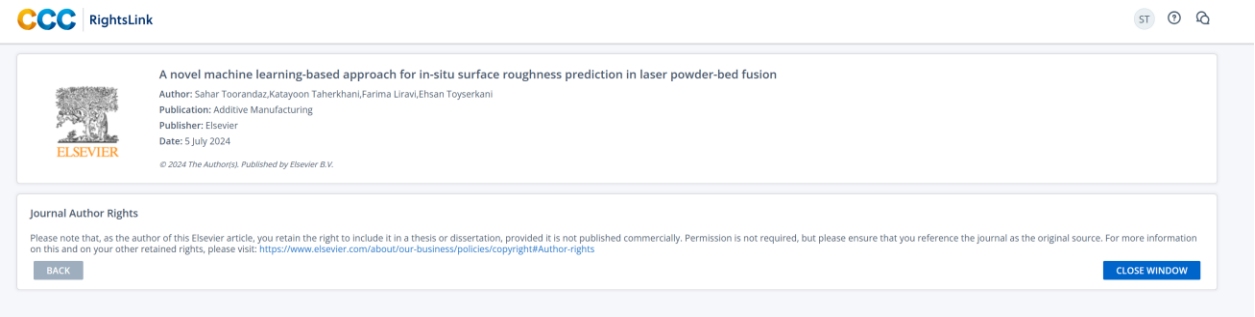
About Your Work

Title of new work	Novel Machine Learning-Driven Platforms for In-Situ Prediction of Vertical and Top Surface Roughness in Laser Powder-Bed Fusion
Institution name	University of Waterloo
Expected presentation date	Apr 2025

Additional Data

Portions	Figure 9
The Requesting Person / Organization to Appear on the License	Sahar Toorandaz Kenari

Chapter 3:


RightsLink
A novel machine learning-based approach for in-situ surface roughness prediction in laser powder-bed fusion
Author: Sahar Toorandaz,Katayoon Taherkhani,Farima Liravi,Ehsan Toyserkani
Publication: Additive Manufacturing
Publisher: Elsevier
Date: 5 July 2024
© 2024 The Author(s). Published by Elsevier B.V.
ELSEVIER
Journal Author Rights
Please note that, as the author of this Elsevier article, you retain the right to include it in a thesis or dissertation, provided it is not published commercially. Permission is not required, but please ensure that you reference the journal as the original source. For more information on this and on your other retained rights, please visit: https://www.elsevier.com/about/our-business/policies/copyright#Author-rights
BACK
CLOSE WINDOW

References

[1] C. G. Klingaa, T. Dahmen, S. Baier, S. Mohanty, and J. H. Hattel, "X-ray CT and image analysis methodology for local roughness characterization in cooling channels made by metal additive manufacturing," *Addit Manuf*, vol. 32, 2020, doi: 10.1016/j.addma.2019.101032.

[2] Y. Du, T. Mukherjee, N. Finch, A. De, and T. DebRoy, "High-throughput screening of surface roughness during additive manufacturing," *J Manuf Process*, vol. 81, 2022, doi: 10.1016/j.jmapro.2022.06.049.

[3] K. Taherkhani, G. Cantzler, C. Eischer, and E. Toyserkani, "Development of control systems for laser powder bed fusion," *International Journal of Advanced Manufacturing Technology*, vol. 129, no. 11–12, 2023, doi: 10.1007/s00170-023-12663-9.

[4] R. Wang, B. Standfield, C. Dou, A. C. Law, and Z. J. Kong, "Real-time process monitoring and closed-loop control on laser power via a customized laser powder bed fusion platform," *Addit Manuf*, vol. 66, 2023, doi: 10.1016/j.addma.2023.103449.

[5] S. Toorandaz, K. Taherkhani, F. Liravi, and E. Toyserkani, "A novel machine learning-based approach for in-situ surface roughness prediction in laser powder-bed fusion," *Addit Manuf*, vol. 91, p. 104354, 2024, doi: https://doi.org/10.1016/j.addma.2024.104354.

[6] B. Zhang, Y. Li, and Q. Bai, "Defect Formation Mechanisms in Selective Laser Melting: A Review," 2017. doi: 10.1007/s10033-017-0121-5.

[7] W. Shifeng, L. Shuai, W. Qingsong, C. Yan, Z. Sheng, and S. Yusheng, "Effect of molten pool boundaries on the mechanical properties of selective laser melting parts," *J Mater Process Technol*, vol. 214, no. 11, 2014, doi: 10.1016/j.jmatprotec.2014.06.002.

[8] M. J. Matthews, G. Guss, S. A. Khairallah, A. M. Rubenchik, P. J. Depond, and W. E. King, "Denudation of metal powder layers in laser powder bed fusion processes," *Acta Mater*, vol. 114, 2016, doi: 10.1016/j.actamat.2016.05.017.

[9] G. Li *et al.*, "Investigation into the effect of energy density on densification, surface roughness and loss of alloying elements of 7075 aluminium alloy processed by laser powder bed fusion," *Opt Laser Technol*, vol. 147, Mar. 2022, doi: 10.1016/j.optlastec.2021.107621.

[10] R. Cunningham, S. P. Narra, C. Montgomery, J. Beuth, and A. D. Rollett, "Synchrotron-Based X-ray Microtomography Characterization of the Effect of Processing Variables on Porosity Formation in Laser Power-Bed Additive Manufacturing of Ti-6Al-4V," *JOM*, vol. 69, no. 3, 2017, doi: 10.1007/s11837-016-2234-1.

[11] R. Rai, J. W. Elmer, T. A. Palmer, and T. Debroy, "Heat transfer and fluid flow during keyhole mode laser welding of tantalum, Ti-6Al-4V, 304L stainless steel and vanadium," *J Phys D Appl Phys*, vol. 40, no. 18, 2007, doi: 10.1088/0022-3727/40/18/037.

[12] W. E. King *et al.*, “Observation of keyhole-mode laser melting in laser powder-bed fusion additive manufacturing,” *J Mater Process Technol*, vol. 214, no. 12, 2014, doi: 10.1016/j.jmatprotec.2014.06.005.

[13] A. R. Nassar, M. A. Gundermann, E. W. Reutzel, P. Guerrier, M. H. Krane, and M. J. Weldon, “Formation processes for large ejecta and interactions with melt pool formation in powder bed fusion additive manufacturing,” *Sci Rep*, vol. 9, no. 1, Dec. 2019, doi: 10.1038/s41598-019-41415-7.

[14] S. Luisa, N. Contuzzi, A. Angelastro, and A. Domenico, “Capabilities and Performances of the Selective Laser Melting Process,” in *New Trends in Technologies: Devices, Computer, Communication and Industrial Systems*, 2010. doi: 10.5772/10432.

[15] S. Tammas-Williams, P. J. Withers, I. Todd, and P. B. Prangnell, “The Influence of Porosity on Fatigue Crack Initiation in Additively Manufactured Titanium Components,” *Sci Rep*, vol. 7, no. 1, 2017, doi: 10.1038/s41598-017-06504-5.

[16] E. Malekipour and H. El-Mounayri, “Common defects and contributing parameters in powder bed fusion AM process and their classification for online monitoring and control: a review,” *International Journal of Advanced Manufacturing Technology*, vol. 95, no. 1–4, pp. 527–550, Mar. 2018, doi: 10.1007/s00170-017-1172-6.

[17] B. Carl Hauser BEng, “Selective laser sintering of a stainless steel powder,” 2003.

[18] J. Platl *et al.*, “Potential Causes for Cracking of a Laser Powder Bed Fused Carbon-free FeCoMo Alloy,” *BHM Berg- und Hüttenmännische Monatshefte*, May 2022, doi: 10.1007/s00501-022-01238-y.

[19] R. Li, J. Liu, Y. Shi, L. Wang, and W. Jiang, “Balling behavior of stainless steel and nickel powder during selective laser melting process,” *International Journal of Advanced Manufacturing Technology*, vol. 59, no. 9–12, 2012, doi: 10.1007/s00170-011-3566-1.

[20] S. Das, “Physical Aspects of Process Control in Selective Laser Sintering of Metals,” 2003. doi: 10.1002/adem.200310099.

[21] C. Guo *et al.*, “Effect of processing parameters on surface roughness, porosity and cracking of as-built IN738LC parts fabricated by laser powder bed fusion,” *J Mater Process Technol*, vol. 285, Nov. 2020, doi: 10.1016/j.jmatprotec.2020.116788.

[22] J. C. Snyder and K. A. Thole, “Understanding laser powder bed fusion surface roughness,” *Journal of Manufacturing Science and Engineering, Transactions of the ASME*, vol. 142, no. 7, Jul. 2020, doi: 10.1115/1.4046504.

[23] J. C. Fox, S. P. Moylan, and B. M. Lane, “Effect of Process Parameters on the Surface Roughness of Overhanging Structures in Laser Powder Bed Fusion Additive Manufacturing,” in *Procedia CIRP*, 2016. doi: 10.1016/j.procir.2016.02.347.

[24] M. Taheri Andani, R. Dehghani, M. R. Karamooz-Ravari, R. Mirzaeifar, and J. Ni, “A study on the effect of energy input on spatter particles creation during selective laser melting process,” *Addit Manuf*, vol. 20, 2018, doi: 10.1016/j.addma.2017.12.009.

[25] E. Toyserkani, D. Sarker, F. Liravi, P. Russo, and K. Taherkhani, “metal additive manufacturing, A comprehensive review of additive manufacturing processes for metallic structures.” [Online]. Available: www.wiley.com

[26] C. Wang, X. P. Tan, S. B. Tor, and C. S. Lim, “Machine learning in additive manufacturing: State-of-the-art and perspectives,” Dec. 01, 2020, *Elsevier B.V.* doi: 10.1016/j.addma.2020.101538.

[27] W. Electronics Inc, “AN-LD17: Photodiode Basics: Selection & Operation,” 2020. [Online]. Available: www.teamWavelength.com

[28] Osi Optoelectronics, “Photodiode Characteristics,” *Osi Optoelectronics*, 2009.

[29] T. Craeghs, F. Bechmann, S. Berumen, and J. P. Kruth, “Feedback control of Layerwise Laser Melting using optical sensors,” in *Physics Procedia*, 2010. doi: 10.1016/j.phpro.2010.08.078.

[30] S. Clijsters, T. Craeghs, S. Buls, K. Kempen, and J. P. Kruth, “In situ quality control of the selective laser melting process using a high-speed, real-time melt pool monitoring system,” *International Journal of Advanced Manufacturing Technology*, vol. 75, no. 5–8, 2014, doi: 10.1007/s00170-014-6214-8.

[31] C. van GESTEL, “Study of physical phenomena of selective laser melting towards increased productivity,” *Nuclear Inst. and Methods in Physics Research, A*, vol. 6817, 2015.

[32] J. A. Kanko, A. P. Sibley, and J. M. Fraser, “In situ morphology-based defect detection of selective laser melting through inline coherent imaging,” *J Mater Process Technol*, vol. 231, 2016, doi: 10.1016/j.jmatprotec.2015.12.024.

[33] K. Taherkhani, E. Sheydaeian, C. Eischer, M. Otto, and E. Toyserkani, “Development of a defect-detection platform using photodiode signals collected from the melt pool of laser powder-bed fusion,” *Addit Manuf*, vol. 46, 2021, doi: 10.1016/j.addma.2021.102152.

[34] S. Tanwar, “Machine Learning,” in *Computational Science and Its Applications*, 2024. doi: 10.1201/9781003347484-2.

[35] L. Zhao *et al.*, “Review on the correlation between microstructure and mechanical performance for laser powder bed fusion AlSi10Mg,” *Addit Manuf*, vol. 56, p. 102914, 2022, doi: https://doi.org/10.1016/j.addma.2022.102914.

[36] N. Wawrzyniak, P. R. Provencher, M. Brochu, and M. Brochu, “Tensile properties of SS316L produced by LPBF: Influence of specimen dimensions and surface condition,” *Mater Charact*, vol. 203, p. 113117, 2023, doi: https://doi.org/10.1016/j.matchar.2023.113117.

[37] A. Hemmasian Ettefagh, S. Guo, and J. Raush, “Corrosion performance of additively manufactured stainless steel parts: A review,” *Addit Manuf*, vol. 37, p. 101689, 2021, doi: https://doi.org/10.1016/j.addma.2020.101689.

[38] A. Bhatt *et al.*, “In situ characterisation of surface roughness and its amplification during multilayer single-track laser powder bed fusion additive manufacturing,” *Addit Manuf*, vol. 77, p. 103809, 2023, doi: https://doi.org/10.1016/j.addma.2023.103809.

[39] P. J. DePond *et al.*, “In situ measurements of layer roughness during laser powder bed fusion additive manufacturing using low coherence scanning interferometry,” *Mater Des*, vol. 154, pp. 347–359, 2018, doi: https://doi.org/10.1016/j.matdes.2018.05.050.

[40] S. J. Foster *et al.*, “Process-Defect-Structure-Property Correlations During Laser Powder Bed Fusion of Alloy 718: Role of In Situ and Ex Situ Characterizations,” *Metallurgical and Materials Transactions A*, vol. 49, no. 11, pp. 5775–5798, 2018, doi: 10.1007/s11661-018-4870-2.

[41] L. Chen *et al.*, “In-situ process monitoring and adaptive quality enhancement in laser additive manufacturing: A critical review,” *J Manuf Syst*, vol. 74, pp. 527–574, 2024, doi: https://doi.org/10.1016/j.jmsy.2024.04.013.

[42] X. Shan, C. Gao, J. H. Rao, M. Wu, M. Yan, and Y. Bi, “Experimental Study and Random Forest Machine Learning of Surface Roughness for a Typical Laser Powder Bed Fusion Al Alloy,” *Metals (Basel)*, vol. 14, no. 10, 2024, doi: 10.3390/met14101148.

[43] M. Arunadevi *et al.*, “Enhancing surface quality of metal parts manufactured via LPBF: ANN classifier and bayesian learning approach,” *International Journal on Interactive Design and Manufacturing (IJIDeM)*, vol. 18, no. 6, pp. 4093–4101, 2024, doi: 10.1007/s12008-024-01942-8.

[44] I. La Fé-Perdomo, J. A. Ramos-Grez, I. Jeria, C. Guerra, and G. O. Barrionuevo, “Comparative analysis and experimental validation of statistical and machine learning-based regressors for modeling the surface roughness and mechanical properties of 316L stainless steel specimens produced by selective laser melting,” *J Manuf Process*, vol. 80, pp. 666–682, 2022, doi: https://doi.org/10.1016/j.jmapro.2022.06.021.

[45] V. Akhil, G. Raghav, N. Arunachalam, and D. S. Srinivas, “Image Data-Based Surface Texture Characterization and Prediction Using Machine Learning Approaches for Additive Manufacturing,” *J Comput Inf Sci Eng*, vol. 20, no. 2, Jan. 2020, doi: 10.1115/1.4045719.

[46] A. M. Khorasani, I. Gibson, A. H. Ghasemi, and A. Ghaderi, “Modelling of laser powder bed fusion process and analysing the effective parameters on surface characteristics of Ti-6Al-4V,” *Int J Mech Sci*, vol. 168, Feb. 2020, doi: 10.1016/j.ijmecsci.2019.105299.

[47] M. Khorasani *et al.*, “A study on surface morphology and tension in laser powder bed fusion of Ti-6Al-4V,” *The International Journal of Advanced Manufacturing Technology*, vol. 111, pp. 2891–2909, 2020, doi: 10.1007/s00170-020-06221-w/Published.

[48] R. Wang, C. F. Cheung, and C. Wang, “Heterogeneous hypergraph learning for analyzing surface defects in additive manufacturing process,” *J Manuf Syst*, vol. 76, pp. 1–10, 2024, doi: https://doi.org/10.1016/j.jmsy.2024.06.011.

[49] W. Wang, H. Garmestani, and S. Y. Liang, “Prediction of upper surface roughness in laser powder bed fusion,” *Metals (Basel)*, vol. 12, no. 1, Jan. 2022, doi: 10.3390/met12010011.

[50] S. Detwiler and B. Raeymaekers, “Deriving Data-Driven Models That Relate Deterministic Surface Topography Parameters of As-Built Inconel 718 Surfaces to Laser Powder Bed Fusion Process Parameters,” *J Tribol*, vol. 144, no. 12, Sep. 2022, doi: 10.1115/1.4055606.

[51] B. Whip, L. Sheridan, and J. Gockel, “The effect of primary processing parameters on surface roughness in laser powder bed additive manufacturing,” *The International Journal of Advanced Manufacturing Technology*, vol. 103, no. 9, pp. 4411–4422, 2019, doi: 10.1007/s00170-019-03716-z.

[52] B.-Q. Li, Z. Li, P. Bai, B. Liu, and Z. Kuai, “Research on Surface Roughness of AlSi10Mg Parts Fabricated by Laser Powder Bed Fusion,” *Metals (Basel)*, vol. 8, no. 7, 2018, doi: 10.3390/met8070524.

[53] T. Özel, A. Altay, B. Kaftanoğlu, R. Leach, N. Senin, and A. Donmez, “Focus Variation Measurement and Prediction of Surface Texture Parameters Using Machine Learning in Laser Powder Bed Fusion,” *J Manuf Sci Eng*, vol. 142, no. 1, Nov. 2019, doi: 10.1115/1.4045415.

[54] E. Masiagutova, F. Cabanettes, A. Sova, M. Cici, G. Bidron, and P. Bertrand, “Side surface topography generation during laser powder bed fusion of AlSi10Mg,” *Addit Manuf*, vol. 47, p. 102230, 2021, doi: https://doi.org/10.1016/j.addma.2021.102230.

[55] S. Rott, A. Ladewig, K. Friedberger, J. Casper, M. Full, and J. H. Schleifenbaum, “Surface roughness in laser powder bed fusion – Interdependency of surface orientation and laser incidence,” *Addit Manuf*, vol. 36, p. 101437, 2020, doi: https://doi.org/10.1016/j.addma.2020.101437.

[56] P. J. DePond *et al.*, “In situ measurements of layer roughness during laser powder bed fusion additive manufacturing using low coherence scanning interferometry,” *Mater Des*, vol. 154, pp. 347–359, Sep. 2018, doi: 10.1016/j.matdes.2018.05.050.

[57] T. G. Fleming, S. G. L. Nestor, T. R. Allen, M. A. Boukhaled, N. J. Smith, and J. M. Fraser, “Tracking and controlling the morphology evolution of 3D powder-bed fusion in situ using inline coherent imaging,” *Addit Manuf*, vol. 32, Mar. 2020, doi: 10.1016/j.addma.2019.100978.

[58] A. S. Raihan, H. Khosravi, T. H. Bhuiyan, and I. Ahmed, “An augmented surprise-guided sequential learning framework for predicting the melt pool geometry,” *J Manuf Syst*, vol. 75, pp. 56–77, 2024, doi: https://doi.org/10.1016/j.jmsy.2024.05.023.

[59] N. Gerdes, C. Hoff, J. Hermsdorf, S. Kaierle, and L. Overmeyer, “Hyperspectral imaging for prediction of surface roughness in laser powder bed fusion,” *International Journal of Advanced Manufacturing Technology*, vol. 115, no. 4, pp. 1249–1258, Jul. 2021, doi: 10.1007/s00170-021-07274-1.

[60] D. Yan, S. Pasebani, and Z. Fan, “Correlation study between the in-situ thermal signatures and surface roughness produced by laser powder bed fusion,” in *The ASME 2024 19th International Manufacturing Science and Engineering Conference*, 2024. [Online].

Available: http://asmedigitalcollection.asme.org/MSEC/proceedings-pdf/MSEC2024/88100/V001T01A031/7367376/v001t01a031-msec2024-124781.pdf

[61] C. Knaak, L. Masseling, E. Duong, P. Abels, and A. Gillner, "Improving Build Quality in Laser Powder Bed Fusion Using High Dynamic Range Imaging and Model-Based Reinforcement Learning," *IEEE Access*, vol. 9, pp. 55214–55231, 2021, doi: 10.1109/ACCESS.2021.3067302.

[62] M. Qu *et al.*, "Controlling melt flow by nanoparticles to eliminate surface wave induced surface fluctuation," *Addit Manuf*, vol. 59, p. 103081, 2022, doi: https://doi.org/10.1016/j.addma.2022.103081.

[63] H. Zhang, C. K. P. Vallabh, and X. Zhao, "Influence of spattering on in-process layer surface roughness during laser powder bed fusion," *J Manuf Process*, vol. 104, pp. 289–306, 2023, doi: https://doi.org/10.1016/j.jmapro.2023.08.058.

[64] H. Zhang, C. K. Prasad Vallabh, and X. Zhao, "Machine learning enhanced high dynamic range fringe projection profilometry for in-situ layer-wise surface topography measurement during LPBF additive manufacturing," *Precis Eng*, vol. 84, pp. 1–14, 2023, doi: https://doi.org/10.1016/j.precisioneng.2023.06.015.

[65] L. Fuchs and C. Eischer, "In-process monitoring systems for metal additive manufacturing," 2018. [Online]. Available: https://www.eos-apac.info/upload/2020-07/159522956575650000.pdf

[66] K. Taherkhani, C. Eischer, and E. Toyserkani, "An unsupervised machine learning algorithm for in-situ defect-detection in laser powder-bed fusion," *J Manuf Process*, vol. 81, 2022, doi: 10.1016/j.jmapro.2022.06.074.

[67] P. Vesely, "Handbook of Biological Confocal Microscopy, 3rd ed. By James B. Pawley, Editor. Springer Science + Business Media, LLC, New York (2006). ISBN 10: 0-387-25921-X; ISBN 13: 987-0387-25921-5; hardback; 28 + 985 pages," *Scanning*, vol. 29, no. 3, 2007, doi: 10.1002/sca.20059.

[68] C. Sheppard and D. Shotton, "Confocal Laser Scanning Microscopy: Principles," *Carl Zeiss*, 1998.

[69] G. Udupa, M. Singaperumal, R. S. Sirohi, and M. P. Kothiyal, "Characterization of surface topography by confocal microscopy: I. Principles and the measurement system," *Meas Sci Technol*, vol. 11, no. 3, 2000, doi: 10.1088/0957-0233/11/3/320.

[70] E. S. Gadelmawla, M. M. Koura, T. M. A. Maksoud, I. M. Elewa, and H. H. Soliman, "Roughness parameters."

[71] R. Leach, *Characterisation of areal surface texture*, vol. 9783642364587. 2013. doi: 10.1007/978-3-642-36458-7.

[72] K. Li *et al.*, "A comparative study on WE43 magnesium alloy fabricated by laser powder bed fusion coupled with deep cryogenic treatment: Evolution in microstructure and mechanical properties," *Addit Manuf*, vol. 77, 2023, doi: 10.1016/j.addma.2023.103814.

[73] Q. Chen, G. Guillemot, C. A. Gandin, and M. Bellet, “Three-dimensional finite element thermomechanical modeling of additive manufacturing by selective laser melting for ceramic materials,” *Addit Manuf*, vol. 16, 2017, doi: 10.1016/j.addma.2017.02.005.

[74] J. Hofmann, Z. Li, K. Taphorn, J. Herzen, and K. Wudy, “Porosity prediction in laser-based powder bed fusion of polyamide 12 using infrared thermography and machine learning,” *Addit Manuf*, vol. 85, Apr. 2024, doi: 10.1016/j.addma.2024.104176.

[75] R. Kamimura, *Information-theoretic approach to interpret internal representations of self-organizing maps. In: Self Organizing Maps - Applications and Novel Algorithm Design*. 2011. doi: 10.5772/566.

[76] S. Haykin, “Chapter 9: self-organizing maps. In: Neural networks: a comprehensive foundation second edition,” 1999.

[77] O. Kwon *et al.*, “A deep neural network for classification of melt-pool images in metal additive manufacturing,” *J Intell Manuf*, vol. 31, no. 2, 2020, doi: 10.1007/s10845-018-1451-6.

[78] H. Gong, K. Rafi, T. Starr, and B. Stucker, “Generation and detection of defects in metallic parts fabricated by selective laser melting and electron beam melting and their effects on mechanical properties.,” *Solid Freeform Fabrication*, 2013.

[79] G. M. Volpato, U. Tetzlaff, and M. C. Fredel, “A comprehensive literature review on laser powder bed fusion of Inconel superalloys,” 2022. doi: 10.1016/j.addma.2022.102871.

[80] Z. Snow, A. R. Nassar, and E. W. Reutzel, “Invited Review Article: Review of the formation and impact of flaws in powder bed fusion additive manufacturing,” Dec. 01, 2020, *Elsevier B.V.* doi: 10.1016/j.addma.2020.101457.

[81] A. Mirabal, I. Loza-Hernandez, C. Clark, D. E. Hooks, M. McBride, and J. A. Stull, “Roughness measurements across topographically varied additively manufactured metal surfaces,” *Addit Manuf*, vol. 69, 2023, doi: 10.1016/j.addma.2023.103540.

[82] R. Esmaeilizadeh, U. Ali, A. Keshavarzkermani, Y. Mahmoodkhani, E. Marzbanrad, and E. Toyserkani, “On the effect of spatter particles distribution on the quality of Hastelloy X parts made by laser powder-bed fusion additive manufacturing,” *J Manuf Process*, vol. 37, 2019, doi: 10.1016/j.jmapro.2018.11.012.

[83] D. Kozjek, F. M. Carter, C. Porter, J. E. Mogonye, K. Ehmann, and J. Cao, “Data-driven prediction of next-layer melt pool temperatures in laser powder bed fusion based on co-axial high-resolution Planck thermometry measurements,” *J Manuf Process*, vol. 79, pp. 81–90, Jul. 2022, doi: 10.1016/j.jmapro.2022.04.033.

[84] N. V. Chawla, K. W. Bowyer, L. O. Hall, and W. P. Kegelmeyer, “SMOTE: Synthetic minority over-sampling technique,” *Journal of Artificial Intelligence Research*, vol. 16, 2002, doi: 10.1613/jair.953.

[85] S. M. Estalaki, C. S. Lough, R. G. Landers, E. C. Kinzel, and T. Luo, “Predicting defects in laser powder bed fusion using in-situ thermal imaging data and machine learning,” *Addit Manuf*, vol. 58, Oct. 2022, doi: 10.1016/j.addma.2022.103008.

[86] V. S. Spelmen and R. Porkodi, “A Review on Handling Imbalanced Data,” in *Proceedings of the 2018 International Conference on Current Trends towards Converging Technologies, ICCTCT 2018*, 2018. doi: 10.1109/ICCTCT.2018.8551020.

[87] M. Belgiu and L. Drăgu, “Random forest in remote sensing: A review of applications and future directions,” 2016. doi: 10.1016/j.isprsjprs.2016.01.011.

[88] Q. Dong, X. Chen, and B. Huang, “Decision trees and ensemble learning,” in *Data Analysis in Pavement Engineering*, Elsevier, 2024, pp. 211–222. doi: 10.1016/b978-0-443-15928-2.00017-3.

[89] T. Chen and T. He, “xgboost: Extreme Gradient Boosting,” *R Lecture*, no. 2016, 2014.

[90] S. Shalev-Shwartz and S. Ben-David, *Understanding machine learning: From theory to algorithms*, vol. 9781107057135. 2013. doi: 10.1017/CBO9781107298019.

[91] D. E. Rumelhart, G. E. Hinton, and R. J. Williams, “Learning representations by back-propagating errors,” *Nature*, vol. 323, no. 6088, 1986, doi: 10.1038/323533a0.

[92] P. Pławiak and K. Rzecki, “Approximation of phenol concentration using computational intelligence methods based on signals from the metal-oxide sensor array,” *IEEE Sens J*, vol. 15, no. 3, 2015, doi: 10.1109/JSEN.2014.2366432.

[93] K. Taherkhani, O. Ero, F. Liravi, S. Toorandaz, and E. Toyserkani, “On the application of in-situ monitoring systems and machine learning algorithms for developing quality assurance platforms in laser powder bed fusion: A review,” 2023. doi: 10.1016/j.jmapro.2023.05.048.

[94] H. Jin, F. Chollet, Q. Song, and X. Hu, “AutoKeras: An AutoML Library for Deep Learning,” 2023.

[95] D. L. Olson and D. Delen, *Advanced data mining techniques*. 2008. doi: 10.1007/978-3-540-76917-0.

[96] H. He and Y. Ma, *Imbalanced learning: Foundations, algorithms, and applications*. 2013. doi: 10.1002/9781118646106.

[97] P. Promoppatum, R. Onler, and S. C. Yao, “Numerical and experimental investigations of micro and macro characteristics of direct metal laser sintered Ti-6Al-4V products,” *J Mater Process Technol*, vol. 240, 2017, doi: 10.1016/j.jmatprotec.2016.10.005.

[98] G. Kasperovich, J. Haubrich, J. Gussone, and G. Requena, “Correlation between porosity and processing parameters in TiAl6V4 produced by selective laser melting,” *Mater Des*, vol. 105, 2016, doi: 10.1016/j.matdes.2016.05.070.

[99] C. Yao, T. Zhang, Z. An, and M. Dang, “Process identification of laser powder bed fusion anomalies based on process-monitored melt pool radiation intensity data,” *J Phys Conf Ser*, vol. 2746, no. 1, p. 12047, May 2024, doi: 10.1088/1742-6596/2746/1/012047.

[100] H. Zhou, C. Song, Y. Yang, and V. Trofimov, “In Situ Monitoring of Melt Pool and Signal Modification in Laser Powder Bed Fusion,” *IEEE Sens J*, vol. 23, no. 20, 2023, doi: 10.1109/JSEN.2023.3311092.

[101] J. Ng and J. J. Goldberger, “Understanding and interpreting dominant frequency analysis of AF electrograms,” 2007. doi: 10.1111/j.1540-8167.2007.00832.x.

[102] T. Chen and C. Guestrin, “XGBoost: A scalable tree boosting system,” in *Proceedings of the ACM SIGKDD International Conference on Knowledge Discovery and Data Mining*, 2016. doi: 10.1145/2939672.2939785.

[103] L. Breiman, “Random Forests,” *Mach Learn*, vol. 45, no. 1, pp. 5–32, 2001, doi: 10.1023/A:1010933404324.

[104] A. J. Smola and B. Schölkopf, “A tutorial on support vector regression,” *Stat Comput*, vol. 14, no. 3, pp. 199–222, 2004, doi: 10.1023/B:STCO.0000035301.49549.88.

[105] E. Schulz, M. Speekenbrink, and A. Krause, “A tutorial on Gaussian process regression: Modelling, exploring, and exploiting functions,” *J Math Psychol*, vol. 85, 2018, doi: 10.1016/j.jmp.2018.03.001.

[106] N. Ketkar and J. Moolayil, “Feed-Forward Neural Networks,” in *Deep Learning with Python*, 2021. doi: 10.1007/978-1-4842-5364-9_3.

[107] S. Kumar *et al.*, “Machine learning techniques in additive manufacturing: a state of the art review on design, processes and production control,” 2023. doi: 10.1007/s10845-022-02029-5.

[108] W. Muhammad, J. Kang, O. Ibragimova, and K. Inal, “Experimental investigation and development of a deep learning framework to predict process-induced surface roughness in additively manufactured aluminum alloys,” *Welding in the World*, vol. 67, no. 4, 2023, doi: 10.1007/s40194-022-01445-8.

[109] T. Batu, H. G. Lemu, and H. Shimels, “Application of Artificial Intelligence for Surface Roughness Prediction of Additively Manufactured Components,” *Materials*, vol. 16, no. 18, 2023, doi: 10.3390/ma16186266.